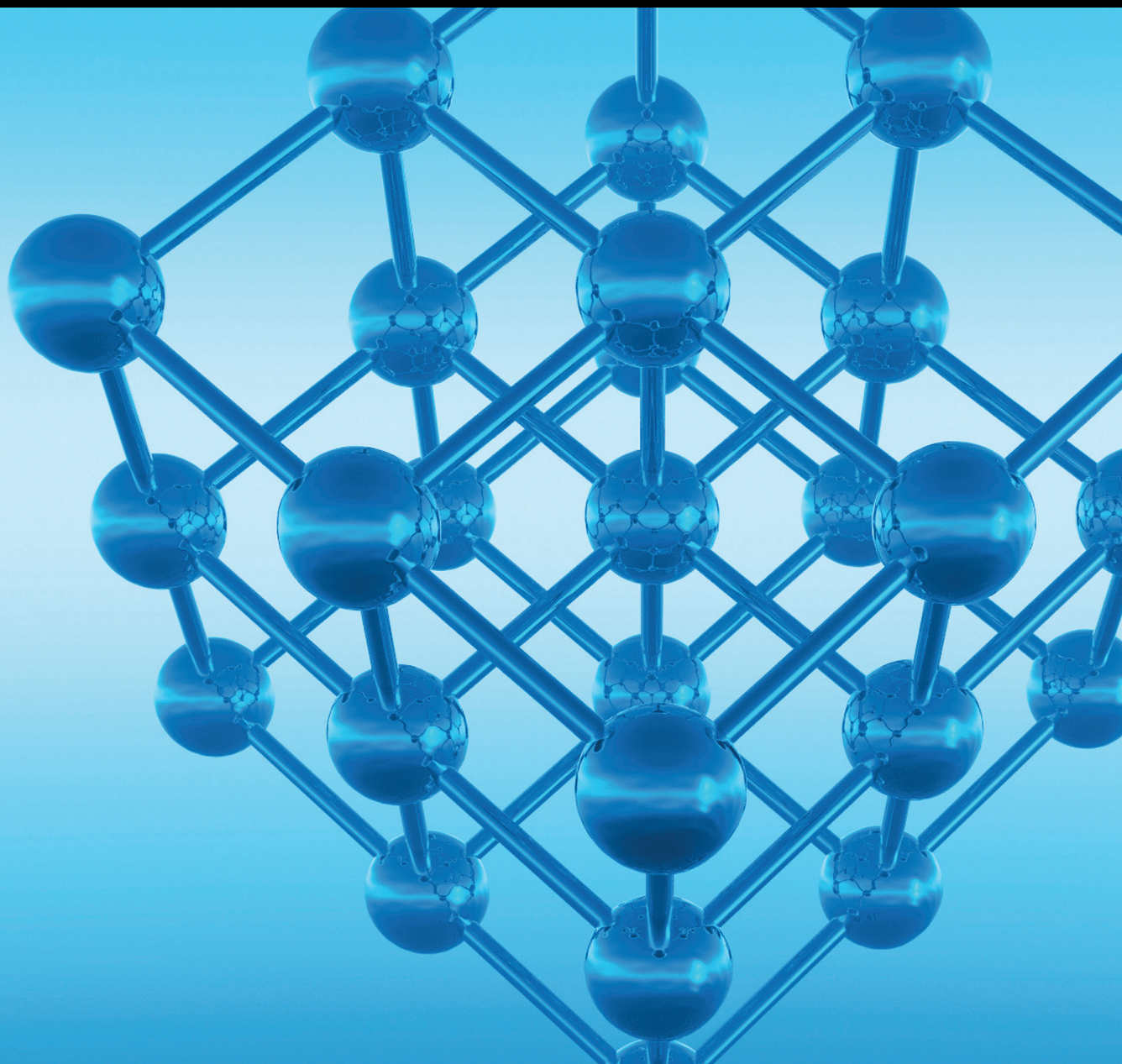


Low-Dimensional Semiconductor Structures for Optoelectronic Applications

Guest Editors: Wei Lu, Hong Chen, Weida Hu, Guofeng Song, Wen Lei,
and Ying Fu





Low-Dimensional Semiconductor Structures for Optoelectronic Applications

Advances in Condensed Matter Physics

Low-Dimensional Semiconductor Structures for Optoelectronic Applications

Guest Editors: Wei Lu, Hong Chen, Weida Hu, Guofeng Song,
Wen Lei, and Ying Fu



Copyright © 2015 Hindawi Publishing Corporation. All rights reserved.

This is a special issue published in "Advances in Condensed Matter Physics." All articles are open access articles distributed under the Creative Commons Attribution License, which permits unrestricted use, distribution, and reproduction in any medium, provided the original work is properly cited.

Editorial Board

Dario Alfe, UK	Yuri Galperin, Norway	Joseph S. Poon, USA
Bohdan Andraka, USA	Russell Giannetta, USA	Ruslan Prozorov, USA
Daniel Arovas, USA	James L. Gole, USA	Leonid Pryadko, USA
Veer P. S. Awana, India	Prasenjit Guptasarma, USA	Charles Rosenblatt, USA
Arun Bansil, USA	Da-Ren Hang, Taiwan	Omid Saremi, Canada
Ward Beyermann, USA	M. Zahid Hasan, USA	Mohindar S. Seehra, USA
Golam M. Bhuiyan, Bangladesh	Yurij Holovatch, Ukraine	Sergei Sergeenkov, Brazil
Rudro R. Biswas, USA	Chia-Ren Hu, USA	Ivan Smalyukh, USA
Luis L. Bonilla, Spain	David Huber, USA	Daniel L. Stein, USA
Mark Bowick, USA	Nigel E. Hussey, UK	Michael C. Tringides, USA
Gang Cao, USA	Philippe Jacquod, USA	Sergio E. Ulloa, USA
Ashok Chatterjee, India	Jan A. Jung, Canada	Attila Virosztek, Hungary
Ram N. P. Choudhary, India	Feo V. Kusmartsev, UK	Markus R. Wagner, Germany
Kim Chow, Canada	Rosa Lukaszew, USA	Gary Wysin, USA
Oleg Derzhko, Ukraine	Victor V. Moshchalkov, Belgium	Kiyokazu Yasuda, Japan
Hiromi Kitahara Eba, Japan	Charles Myles, USA	Fajun Zhang, Germany
Gayyanath Fernando, USA	Vladimir A. Osipov, Russia	
Jrg Fink, Germany	Rolfe Petschek, USA	

Contents

Low-Dimensional Semiconductor Structures for Optoelectronic Applications, Wei Lu, Hong Chen, Weida Hu, Guofeng Song, Wen Lei, and Ying Fu
Volume 2015, Article ID 156196, 2 pages

Synthesis, Characterization, and Photoluminescence on the Glass Doped with AgInS₂ Nanocrystals, Dewu Yin, Lang Pei, Zhen Liu, Xinyu Yang, Weidong Xiang, and Xiyan Zhang
Volume 2015, Article ID 141056, 5 pages

Analysis of Low Dimensional Nanoscaled Inversion-Mode InGaAs MOSFETs for Next-Generation Electrical and Photonic Applications, C. H. Yu, X. Y. Chen, X. D. Luo, W. W. Xu, and P. S. Liu
Volume 2015, Article ID 423791, 6 pages

Photoelectric Characteristics of Double Barrier Quantum Dots-Quantum Well Photodetector, M. J. Wang, F. Y. Yue, and F. M. Guo
Volume 2015, Article ID 920805, 6 pages

Modeling and Design of Graphene GaAs Junction Solar Cell, Yawei Kuang, Yushen Liu, Yulong Ma, Jing Xu, Xifeng Yang, Xuekun Hong, and Jinfu Feng
Volume 2015, Article ID 326384, 7 pages

Shell Thickness-Dependent Strain Distributions of Confined Au/Ag and Ag/Au Core-Shell Nanoparticles, Feng Liu, Honghua Huang, Ying Zhang, Ting Yu, Cailei Yuan, and Shuangli Ye
Volume 2015, Article ID 583863, 7 pages

Experimental Determination of Effective Minority Carrier Lifetime in HgCdTe Photovoltaic Detectors Using Optical and Electrical Methods, Haoyang Cui, Jialin Wang, Chaoqun Wang, Can Liu, Kaiyun Pi, Xiang Li, Yongpeng Xu, and Zhong Tang
Volume 2015, Article ID 482738, 5 pages

Modeling and Simulation of a Resonant-Cavity-Enhanced InGaAs/GaAs Quantum Dot Photodetector, W. W. Wang, F. M. Guo, and Y. Q. Li
Volume 2015, Article ID 847510, 6 pages

Determination of Temperature-Dependent Stress State in Thin AlGaN Layer of AlGaN/GaN HEMT Heterostructures by Near-Resonant Raman Scattering, Yanli Liu, Xifeng Yang, Dunjun Chen, Hai Lu, Rong Zhang, and Youdou Zheng
Volume 2015, Article ID 918428, 6 pages

Photoreponse of Long-Wavelength AlGaAs/GaAs Quantum Cascade Detectors, Liang Li and Dayuan Xiong
Volume 2015, Article ID 306912, 5 pages

Influence of Codoping on the Optical Properties of ZnO Thin Films Synthesized on Glass Substrate by Chemical Bath Deposition Method, G. Shanmuganathan and I. B. Shameem Banu
Volume 2014, Article ID 761960, 9 pages

Editorial

Low-Dimensional Semiconductor Structures for Optoelectronic Applications

Wei Lu,¹ Hong Chen,² Weida Hu,¹ Guofeng Song,³ Wen Lei,⁴ and Ying Fu⁵

¹*Shanghai Institute of Technical Physics, Chinese Academy of Sciences, Shanghai 200083, China*

²*The Institute of Physics, Chinese Academy of Sciences, Beijing 100190, China*

³*The Institute of Semiconductors, Chinese Academy of Sciences, Beijing 200083, China*

⁴*University of Western Australia, Crawley, WA 6009, Australia*

⁵*The Royal Institute of Technology (KTH), 136 40 Stockholm, Sweden*

Correspondence should be addressed to Wei Lu; luwei@mail.sitp.ac.cn

Received 15 February 2015; Accepted 15 February 2015

Copyright © 2015 Wei Lu et al. This is an open access article distributed under the Creative Commons Attribution License, which permits unrestricted use, distribution, and reproduction in any medium, provided the original work is properly cited.

A truly extraordinary research effort is pressed to develop a full understanding of the properties of matters at the nanoscale and its possible applications. The aim of the special issue is to include the recent advances in new and original theoretical, experimental, and/or simulation works in narrow-gap, nanoscaled, and low-dimensional structures for infrared detectors, solar cells, and transistors.

Among a large number of submissions, we have selected 10 papers for publication in the special issue. The work reported by H. Cui et al. is believed to be very useful in measuring the minority carrier lifetime of HgCdTe photodetector by using optical and electrical methods. The paper by Y. Liu et al. reports an experimental work for determining temperature-dependent stress state in thin AlGaN layer of AlGaN/GaN HEMT heterostructures by near-resonant Raman scattering. The theoretical modeling is in good agreement with the measurements. M. J. Wang et al. and W. W. Wang et al. published two papers on InGaAs/GaAs quantum dot/quantum well infrared photodetector. Both papers are highly important for the design, fabrication, and characterization of quantum dot/quantum well infrared photodetectors. A two-dimensional simulation for effects of structure parameters on shot channel effects of low-dimensional nanoscaled inversion-mode InGaAs MOSFETs has been investigated in detail by C. H. Yu et al. The paper by

L. Li and D. Xiong reports a mathematical model for investigating photoresponse of long-wavelength AlGaAs/GaAs quantum cascade detectors. The theoretical results for simulating photoresponse of AlGaAs/GaAs detectors could be of immense importance for the designing of AlGaAs/GaAs-based optoelectronic devices. An interesting work on modeling and design of graphene GaAs junction solar cell reported by Y. Kuang et al. has also been considered for publication. D. Yin et al. report on synthesis, characterization, and photoluminescence on the glass doped with AgInS₂ nanocrystals. The paper by F. Liu et al. presents a detailed investigation on shell thickness-dependent strain distributions of confined Au/Ag and Ag/Au core-shell nanoparticles, providing an effective method to manipulate the strain distributions of the Au/Ag and Ag/Au nanoparticles by tuning the thickness of the shell. The paper by G. Shanmuganathan and I. B. S. Banu reports influence of codoping on the optical properties of ZnO thin films synthesized on glass substrate by chemical bath deposition method, confirming that codoped ZnO thin films can be suitable candidates for antireflecting coating and optoelectronic devices. It is believed that the special issue will be of significant interest to the scientists and researchers working in the areas related to the narrow-gap semiconductors and low-dimensional structures for optoelectronic applications.

Acknowledgments

We would like to thank all the authors and coauthors who submitted their papers to the special issue.

*Wei Lu
Hong Chen
Weida Hu
Guofeng Song
Wen Lei
Ying Fu*

Research Article

Synthesis, Characterization, and Photoluminescence on the Glass Doped with AgInS₂ Nanocrystals

Dewu Yin,^{1,2} Lang Pei,² Zhen Liu,² Xinyu Yang,^{1,2} Weidong Xiang,^{1,2} and Xiyan Zhang¹

¹College of Materials Science and Engineering, Changchun University of Science and Technology, Changchun 130022, China

²Faculty of Chemistry & Material Engineering, Wenzhou University, Wenzhou 325027, China

Correspondence should be addressed to Xinyu Yang; yangxinyu13@126.com and Xiyan Zhang; xiyanzhang@126.com

Received 17 August 2014; Accepted 17 September 2014

Academic Editor: Wen Lei

Copyright © 2015 Dewu Yin et al. This is an open access article distributed under the Creative Commons Attribution License, which permits unrestricted use, distribution, and reproduction in any medium, provided the original work is properly cited.

We demonstrated a synthetic process on the glass doped with AgInS₂ nanocrystals through sol-gel method under a controlled atmosphere. X-ray powder diffraction and X-ray photoelectron spectra revealed that the AgInS₂ crystalline phase had formed in the glass matrix. Transmittance electron microscopy showed that these AgInS₂ crystals had spherical shape and good dispersed form in the glass matrix, and their diameter distribution was mainly focused on three size regions. Furthermore, the glass doped with AgInS₂ nanocrystals exhibited three photoluminescence peaks located at 1.83 eV, 2.02 eV, and 2.21 eV, which were ascribed to the introduction of AgInS₂ nanocrystals in the glass.

1. Introduction

In the last two decades, semiconductor nanocrystals have attracted tremendous attention due to their unique electronic and optical properties [1, 2]. Such nanocrystals have potential applications for future photonic devices and electronic devices such as light emitting diodes, solar cell materials, nonlinear optical devices, and biooptical imaging devices [2–4]. Typically of semiconductor materials, II-VI-type semiconductor nanocrystals have drawn more attention due to their considerable fluorescent properties [5]. But, unfortunately, the constituents of these II-VI semiconductors often include some toxic elements such as Cd, As, Pb, Hg, and Se [6, 7], which are not an environmental friendly model. Thus, developing a semiconductor with nontoxic constituents is very important for more wide applications in the future. One thing worth mentioning is the ternary I-III-VI₂-type semiconductors like AgInS₂, which has been recognized as an ideal replacement [8–10]. AgInS₂ crystals with the band-gap energy of 1.9 eV, specially, exhibit a chalcopyrite structure [11]. Such AgInS₂-based materials are often used to develop high-efficiency Cu(In,Ga)Se₂ solar cells because the lattice parameter of AgInS₂ crystals is almost the same as that of Cu(In,Ga)Se₂ crystals [12]. In particular, some studies

showed that some AgInS₂ crystals with nanolevel size distribution and well-defined spherical morphology exhibited considerable photoluminescence and high quantum yield (~41%) [13], indicating that the morphology and size distribution of AgInS₂ nanocrystals should be controlled effectively in practical applications. Thus, how to achieve a suitable morphology and size distribution of AgInS₂ nanocrystals will be very crucial in the synthetic process.

Nanocrystals glasses, namely, by adding nanolevel crystalline particles into the glass matrices, are one of the most interesting issues in materials science. The reason is that glasses seem to be preferable for optical devices because of their ease of fabrication in desirable shapes and sizes, high transparency, good chemical and thermal durability, threshold to optical damage, and so forth [14], which make them promising matrices for loading different nanocrystals, thereby giving glasses some good performances. Consequently, a variety of nanocrystals glasses have been developed for many applications, such as solid state laser [15], nonlinear media [16], and photonic applications [17]. Under this background, researchers have been trying to employ different methods for realizing the development of nanocrystals glasses. In this paper, we demonstrated an effective path to achieve the synthesis of the glass doped with AgInS₂

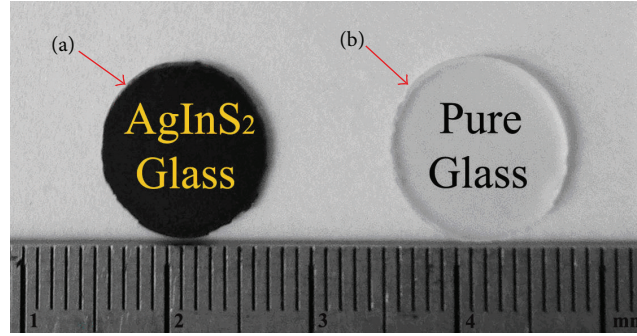


FIGURE 1: Photograph of as-obtained glass: (a) AgInS_2 nanocrystals glass and (b) pure glass.

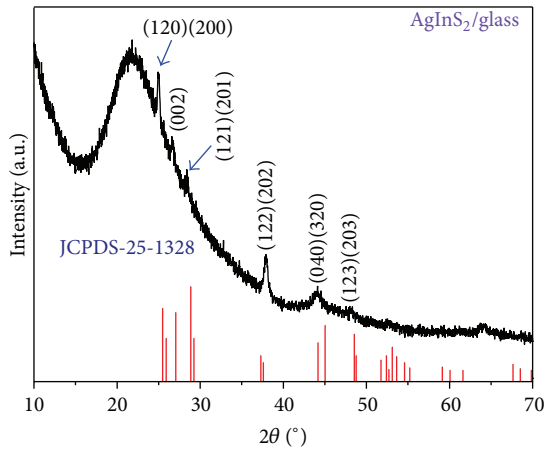


FIGURE 2: XRD pattern of the as-obtained glass. The JCPDS pattern of AgInS_2 crystals is also shown.

nanocrystals through sol-gel method under a controlled atmosphere. By adjusting these parameters including temperature, time, and atmosphere, AgInS_2 nanocrystals with well-defined spherical morphology and suitable size distribution were successfully doped in the glass matrix. It meant that nanocrystals-glass material, which has both the properties of semiconductor and optical glass, could be realized in the same material system. In addition, microstructure and photoluminescence of the glass doped with AgInS_2 nanocrystals were also studied in this paper. We believe that the path will provide a reference to realize the synthesis of different semiconductor nanocrystals in the glass matrices, which is very necessary and significant to study the photonics and optoelectronics in materials science.

2. Experimental Section

In a typical synthetic process, bulk glass doped with AgInS_2 nanocrystals was synthesized through sol-gel method under a controlled atmosphere. The stoichiometric composition of the glass was designed for the following: Na_2O (7 mol%), B_2O_3 (23 mol%), and SiO_2 (70 mol%) • AgInS_2 (1.5 mol%). The synthetic process of the stiff gel agreed with our previous work [18]. Silver and indium nitrate salts were chosen to form AgInS_2 nanocrystals. Specific synthetic process of the

glass doped with AgInS_2 nanocrystals showed the following. Firstly, the yellow-brown stiff gel containing silver and indium ions was heated in oxygen atmosphere at 450°C and kept for 10 h at this temperature. Secondly, the aerogel was exposed to hydrogen atmosphere at 450°C for 10 h to form Ag-In alloy nanocrystals and then the aerogel was further heated in hydrogen sulfide atmosphere up to 600°C . Finally, an indehiscent, well-densified brown glass doped with AgInS_2 nanocrystals was obtained, as shown in Figure 1(a). Meanwhile, transparent pure post glass was shown in Figure 1(b).

The crystalline phase was performed on a Germany Bruker X-ray diffractometer from 10° to 70° . The formation of AgInS_2 was measured by AXIS ULTRA DLD X-ray photoelectron spectrometer. Transmission electron microscopy was recorded on a FEI Tecnai F20 transmission electron microscope for the morphology, size distribution, and crystalline phase of AgInS_2 nanocrystals. The photoluminescence spectra of the as-obtained glass were measured by Horiba Jobin Yvon 6400 Raman scattering spectrometer with a 325 nm laser as the excitation source at room temperature.

3. Results and Discussion

Figure 2 represented an X-ray powder diffraction (XRD) result of the as-obtained glass, in which several characteristic

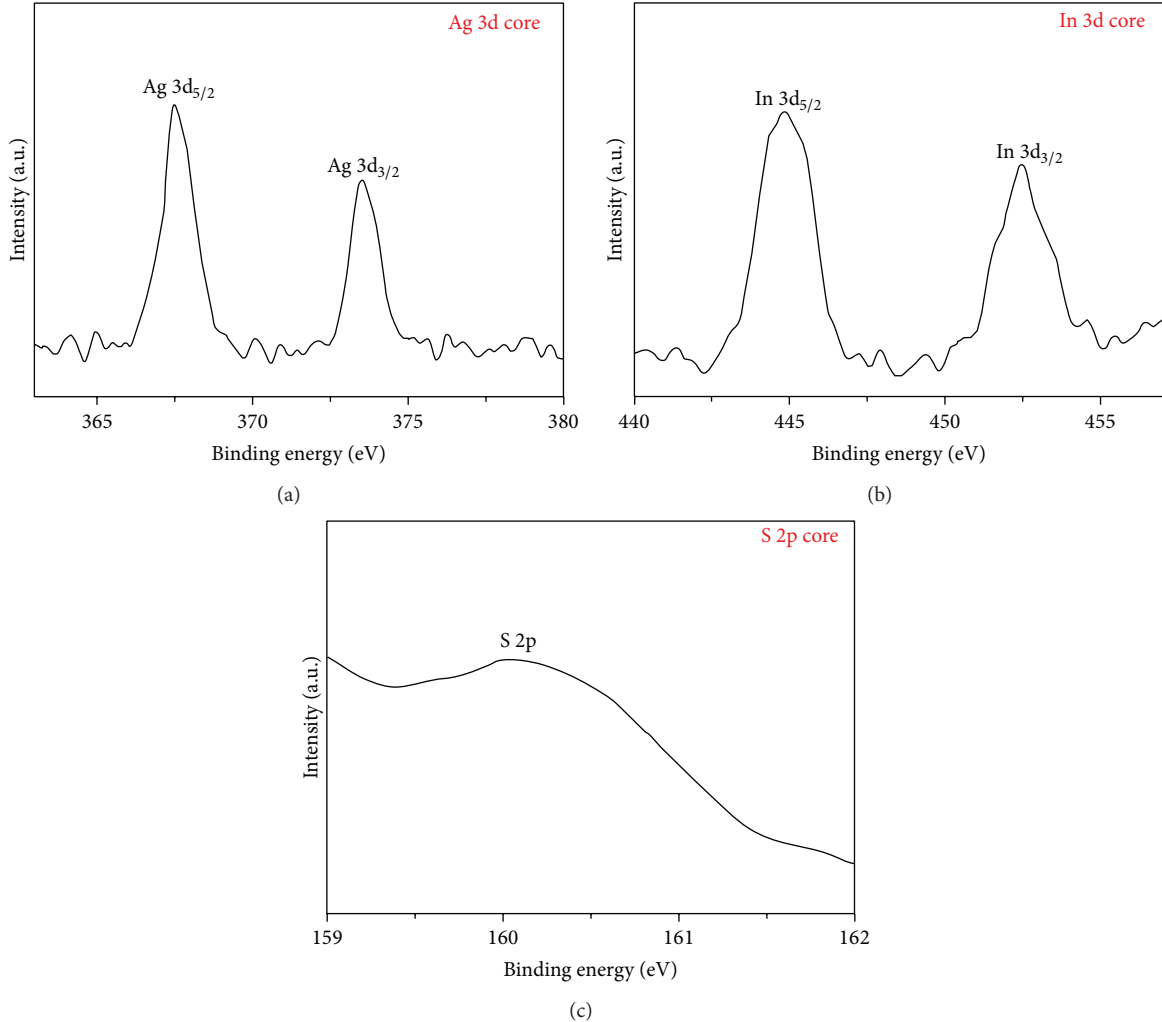


FIGURE 3: XPS pattern of AgInS_2 nanocrystal: (a) Ag 3d core level spectrum; (b) In 3d core level spectrum; (c) S 2p core level spectrum.

diffraction peaks corresponding to (120), (002), (121), (122), and (040) of orthorhombic AgInS_2 crystals (JCPDS-25-1328) are observed. No other diffraction peaks are observed in the diffraction curve, indicating that the desired product for AgInS_2 crystals has formed in the glass matrix. Moreover, the characteristic diffraction peak shapes are broad, suggesting that the as-obtained AgInS_2 crystals should be small in size.

Figure 3 represented the high-resolution XPS result of the as-obtained glass, from which the Ag 3d, In 3d, and S 2p XPS spectra are evident. Figure 3(a) shows that the binding energies of Ag 3d_{3/2} and Ag 3d_{5/2} located at 373.6 eV and 367.5 eV with a peak spacing of 6.1 eV, which agreed with the standard reference XPS spectrum of Ag (I). Similarly, the peak spacing of In 3d_{3/2} and In 3d_{5/2} located at 452.4 eV and 444.8 eV is 7.6 eV, matching well with In (III), as shown in Figure 3(b). Figure 3(c) shows that the S 2p is an asymmetric peak, maybe resulting from the recombination of S 2p_{1/2} and S 2p_{3/2}. Meanwhile, the Ag 3d and In 3d XPS spectra also reveal that the actual molar ratio of Ag and In is about 0.96 : 1, which is almost approximate to 1:1. The XPS result agreed

well with the XRD result, indicating that AgInS_2 crystals have formed in the glass matrix.

To clarify the morphology, distribution, and crystalline phase of AgInS_2 crystals in the glass matrix, transmission electron microscopy (TEM) measurement was performed. Figure 4(a) shows that the precipitated AgInS_2 particles appear in a spherical shape and good dispersed form, and the diameter size of these AgInS_2 particles mainly focuses on three different regions, as shown in Figure 4(b), including 8~12 nm accounting for 20%, 12~16 nm accounting for 50%, and 16~20 nm accounting for 30%, after counting all particles in Figure 4(a). Figure 4(c) shows the high-resolution TEM result (HRTEM), in which the atomic planes with lattice fringe are observed, indicating a typical crystalline structure. The insets shown in the red square and circle frames are an enlarged image for the lattice fringe, as shown in the main panel of Figure 4(c). The lattice fringe spacing is equal to 0.357 nm corresponding to the (120) plane of AgInS_2 crystals in an orthorhombic crystal system (JCPDS-25-1328). Figure 4(d) shows the selected area electron diffraction

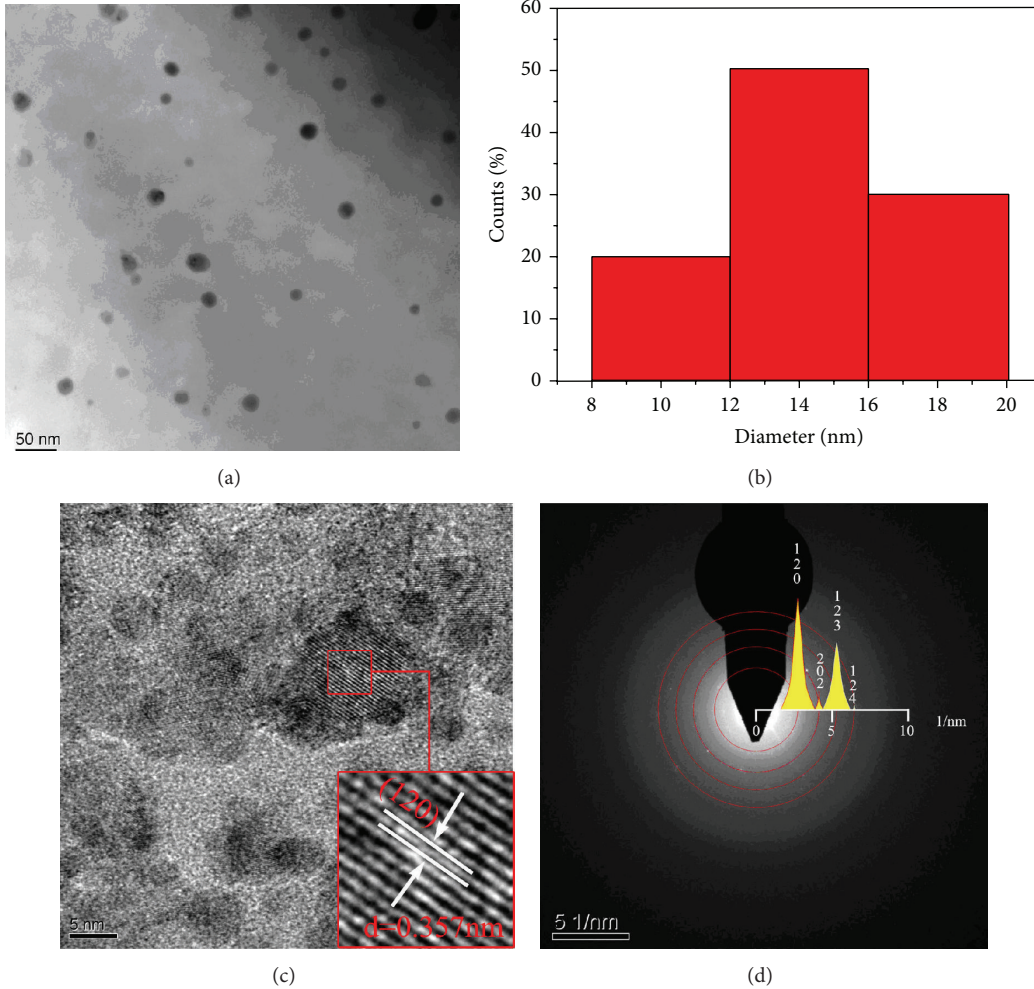


FIGURE 4: TEM analysis of the as-obtained glass: (a) morphology image; (b) size distribution; (c) HRTEM image; (d) SAED image.

(SAED) pattern taken in a zone filled with nanoparticles. The estimated diffraction radii rings correspond well to AgInS₂ lattice planes (120), (202), (123), and (124), respectively. TEM results further confirm the analytical results of XRD and XPS measurements.

Figure 5 represented the photoluminescence result of the pure and as-obtained glasses, which are excited at 325 nm. In a prescribed wavelength scope, it is noticed that no photoluminescence emission peak appears in the pure glass (Curve (a)). However, three photoluminescence emission peaks located at 1.83 eV, 2.02 eV, and 2.21 eV are evident in the as-obtained glass (Curve (b)). Obviously, the different photoluminescence of the two glasses should derive from the AgInS₂ nanocrystals in the glass. Interestingly, the photoluminescence emission peaks appear on three different photon energy positions, which could be attributed to the size distribution of AgInS₂ nanocrystals in the glass. Figures 4(a) and 4(b) show that the diameter sizes of these AgInS₂ nanocrystals are mainly focused on three different regions, indicating that the different photoluminescence emission positions are correlative with the size distribution. Hamanaka et al. and Ogawa et al. had also come to a similar conclusion

[10, 19]. They discovered that the photoluminescence peaks of the AgInS₂ nanocrystals shifted towards a lower energy with increasing nanocrystals size. Such a size-dependent shift of the emission peak should be attributed to a quantum confinement effect of carriers in AgInS₂ nanocrystals. Thus, the photoluminescence should derive from the transition between the lowest quantized levels of the valence and conduction bands in the as-obtained glass. The results also suggest that the as-obtained glass will have better tunability from orange-green to deep red region by adjusting the size distribution of the AgInS₂ nanocrystals in the glass. The relevant work is still in progress.

4. Conclusion

We design a path successfully to realize the synthesis of the glass doped with AgInS₂ nanocrystals by sol-gel method under a controlled atmosphere. XRD and XPS analysis show that the AgInS₂ nanocrystals have formed in the glass, and these AgInS₂ nanocrystals have spherical shape, good dispersed form, and three main size distribution regions observed in TEM analysis, which will cause three significant

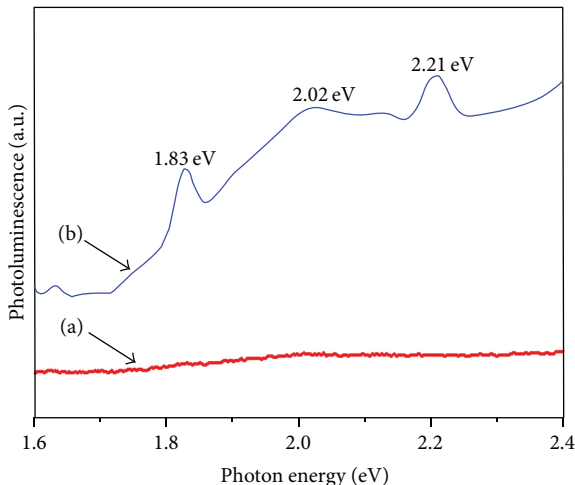


FIGURE 5: Photoluminescence spectra of the as-obtained glasses: (a) pure glass and (b) AgInS_2 nanocrystals glass.

photoluminescence emission peaks located at 1.83 eV, 2.02 eV, and 2.21 eV, respectively. The reason is attributed to a quantum confinement effect of carriers in AgInS_2 nanocrystals. We believe that the synthetic path will become a promising technique in the optical glass materials. In particular, the tunability of emission color in the nanocrystals glass will have a potential application in solid laser, LED, nonlinear optics, and so forth.

Conflict of Interests

The authors declare that there is no conflict of interests regarding the publication of this paper.

Acknowledgments

The work was financially supported by the National Natural Science Foundation of China (Grant no. 51202166), the Zhejiang Province Natural Science Foundation of China (Grant no. Y4100233), and the Wenzhou University Innovation and Career Project of China (Grant no. DC2012006).

References

- [1] H. Weller, "Colloidal semiconductor Q-particles: chemistry in the transition region between solid state and molecules," *Angewandte Chemie International Edition*, vol. 32, pp. 41–53, 1993.
- [2] Y. Masumoto and T. Takagahara, *Semiconductor Quantum Dots: Physics, Spectroscopy and Applications*, Springer, Berlin, Germany, 2002, Springer.
- [3] H. S. Nalwa, *Handbook of Thin Film Materials*, Academic Press, San Diego, Calif, USA, 2002.
- [4] L. W. Liu, R. Hu, W. C. Law et al., "Optimizing the synthesis of red- and near-infrared CuInS_2 and AgInS_2 semiconductor nanocrystals for bioimaging," *Analyst*, vol. 138, no. 20, pp. 6144–6153, 2013.
- [5] J. S. Steckel, S. Coe-Sullivan, V. Bulović, and M. G. Bawendi, "1.3 μm to 1.55 μm tunable electroluminescence from PbSe quantum dots embedded within an organic device," *Advanced Materials*, vol. 15, no. 21, pp. 1862–1866, 2003.
- [6] Z. Lingley, K. Mahalingam, S. Lu, G. J. Brown, and A. Madhukar, "Nanocrystal-semiconductor interface: atomic-resolution cross-sectional transmission electron microscope study of lead sulfide nanocrystal quantum dots on crystalline silicon," *Nano Research*, vol. 7, no. 2, pp. 219–227, 2014.
- [7] S. V. Kahane, V. Sudarsan, and S. Mahamuni, "A study of charge transfer mechanism and optical properties of Au-CdS core-shell nanocrystals," *Journal of Luminescence*, vol. 147, pp. 353–357, 2014.
- [8] J. Y. Chang, G. Q. Wang, C. Y. Cheng, W. X. Lin, and J. C. Hsu, "Strategies for photoluminescence enhancement of AgInS_2 quantum dots and their application as bioimaging probes," *Journal of Materials Chemistry*, vol. 22, pp. 10609–10618, 2012.
- [9] M.-A. Langevin, A. M. Ritcey, and C. N. Allen, "Air-stable near-infrared AgInSe_2 nanocrystals," *ACS Nano*, vol. 8, no. 4, pp. 3476–3482, 2014.
- [10] Y. Hamanaka, T. Ogawa, M. Tsuzuki, K. Ozawa, and T. Kuzuya, "Luminescence properties of chalcopyrite AgInS_2 nanocrystals: Their origin and related electronic states," *Journal of Luminescence*, vol. 133, pp. 121–124, 2013.
- [11] J. L. Shay and B. Tell, "Energy band structure of I-III-VI₂ semiconductors," *Surface Science*, vol. 37, pp. 748–751, 1973.
- [12] Y. Akaki, K. Yamashita, and T. Yoshitake, "Characterization of AgInS_2 thin films prepared by vacuum evaporation," *Physica B*, vol. 407, pp. 2858–2860, 2012.
- [13] X. S. Tang, W. B. A. Ho, and J. M. Xue, "Synthesis of Zn-Doped AgInS_2 nanocrystals and their fluorescence properties," *The Journal of Physical Chemistry C*, vol. 116, no. 17, pp. 9769–9773, 2012.
- [14] F. E. P. Dos Santos, C. B. De Araujo, A. S. L. Gomes et al., "Nonresonant third-order nonlinear properties of glasses in the near infrared," *Journal of Applied Physics*, vol. 106, Article ID 063507, 2009.
- [15] P. T. Guerreiro, S. Ten, N. F. Borrelli, J. Butty, G. E. Jabbour, and N. Peyghambarian, "PbS quantum-dot doped glasses as saturable absorbers for mode locking of a Cr: forsterite laser," *Applied Physics Letters*, vol. 71, no. 12, pp. 1595–1597, 1997.
- [16] L. A. Padiha, A. A. R. Neves, E. Rodriguez, C. L. Cesar, L. C. Barbosa, and C. H. Brito Cruz, "Ultrafast optical switching with CdTe nanocrystals in a glass matrix," *Applied Physics Letters*, vol. 86, Article ID 161111, 2005.
- [17] Q. Luo, X. Fan, X. Qiao, H. Yang, M. Wang, and X. Zhang, " Eu^{2+} -Doped glass ceramics containing BaF_2 nanocrystals as a potential blue phosphor for UV-LED," *Journal of the American Ceramic Society*, vol. 92, no. 4, pp. 942–944, 2009.
- [18] X. Yang, W. Xiang, H. Zhao, H. Liu, X. Zhang, and X. Liang, "Nonlinear saturable absorption of the sodium borosilicate glass containing Bi_2S_3 nanocrystals using Z-scan technique," *Journal of Alloys and Compounds*, vol. 509, no. 26, pp. 7283–7289, 2011.
- [19] T. Ogawa, T. Kuzuya, Y. Hamanaka, and K. Sumiyama, "Synthesis of Ag-In binary sulfide nanoparticles—structural tuning and their photoluminescence properties," *Journal of Materials Chemistry*, vol. 20, no. 11, pp. 2226–2231, 2010.

Research Article

Analysis of Low Dimensional Nanoscaled Inversion-Mode InGaAs MOSFETs for Next-Generation Electrical and Photonic Applications

C. H. Yu,¹ X. Y. Chen,^{1,2} X. D. Luo,¹ W. W. Xu,¹ and P. S. Liu¹

¹Jiangsu Key Laboratory of ASIC Design, Nantong University, Nantong 226019, China

²Laboratory of Advanced Material, Fudan University, Shanghai 200438, China

Correspondence should be addressed to X. Y. Chen; chenxiaoyao@fudan.edu.cn

Received 21 October 2014; Accepted 17 December 2014

Academic Editor: Wen Lei

Copyright © 2015 C. H. Yu et al. This is an open access article distributed under the Creative Commons Attribution License, which permits unrestricted use, distribution, and reproduction in any medium, provided the original work is properly cited.

The electrical characteristics of $\text{In}_{0.53}\text{Ga}_{0.47}\text{As}$ MOSFET grown with Si interface passivation layer (IPL) and high k gate oxide HfO_2 layer have been investigated in detail. The influences of Si IPL thickness, gate oxide HfO_2 thickness, the doping depth, and concentration of source and drain layer on output and transfer characteristics of the MOSFET at fixed gate or drain voltages have been individually simulated and analyzed. The determination of the above parameters is suggested based on their effect on maximum drain current, leakage current, saturated voltage, and so forth. It is found that the channel length decreases with the increase of the maximum drain current and leakage current simultaneously. Short channel effects start to appear when the channel length is less than $0.9\ \mu\text{m}$ and experience sudden sharp increases which make device performance degrade and reach their operating limits when the channel length is further lessened down to $0.5\ \mu\text{m}$. The results demonstrate the usefulness of short channel simulations for designs and optimization of next-generation electrical and photonic devices.

1. Introduction

$\text{In}_{0.53}\text{Ga}_{0.47}\text{As}$ alloys with higher electron mobility are ideal channel materials to implement metal-oxide-semiconductor field effect transistors (MOSFETs) [1, 2]. $\text{In}_{0.53}\text{Ga}_{0.47}\text{As}$ is believed to be easier to obtain unpinned surface Fermi level and thus can potentially provide better transistor performances compared to other III-V materials. At present, low dimensional nanoscaled III-V semiconductor MOSFETs have received particular attention for their potential applications in photodetectors and solar cells [3–10]. As MOSFET scaling approaches physical and technical limits, various specific gate oxides and passivation techniques have been developed to further increase the device performance of $\text{In}_{0.53}\text{Ga}_{0.47}\text{As}$ MOSFETs. Among them, silicon interface passivation layer (IPL) technique has been successfully employed where silicon IPL acts as a barrier layer to prevent reactions between oxygen

and $\text{In}_{0.53}\text{Ga}_{0.47}\text{As}$ layer [11]. The bonds between oxygen and Ga atoms which are closely associated with interface states are replaced by Ga-Si and As-Si bonds during the growth of silicon interface layer [12]. Another functional layer, Ga_2O_3 , Al_2O_3 , or HfO_2 , is also usually deposited as gate oxide in MOSFET structures to improve drain currents [13]. High performance $\text{In}_{0.53}\text{Ga}_{0.47}\text{As}$ MOSFET with silicon IPL and HfO_2 gate oxide has been demonstrated experimentally. However, quantitative analysis of device behavior of this kind of MOSFET is still further needed.

In this paper, the electrical characteristics of nanoscaled $\text{In}_{0.53}\text{Ga}_{0.47}\text{As}$ MOSFET grown with Si IPL and high k gate oxide HfO_2 layer are investigated. The effects of various parameters, such as thickness of Si IPL and HfO_2 layers and thickness and doping concentration of drain and source areas, on drain current and I_{off} are systematically analyzed. Changes of threshold voltage, subthreshold characteristics

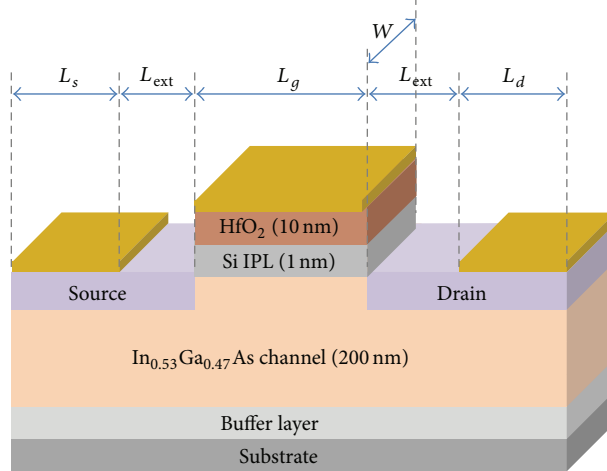


FIGURE 1: Schematic device structure of $\text{In}_{0.53}\text{Ga}_{0.47}\text{As}$ MOSFET.

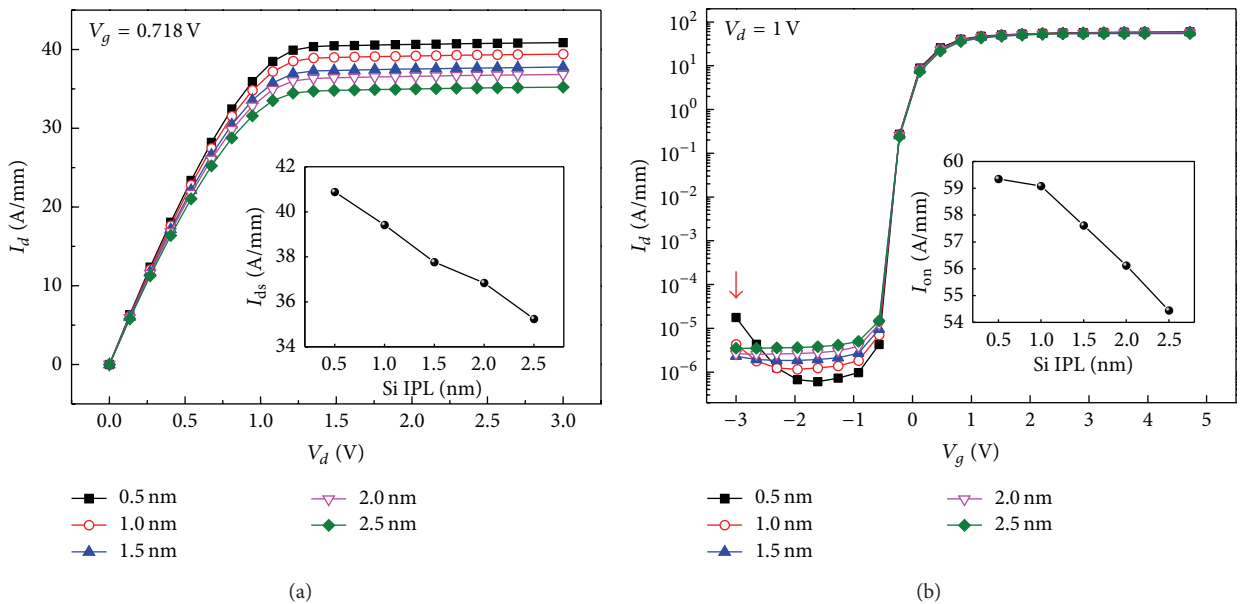


FIGURE 2: Si IPL thickness dependence on output (a) and transfer (b) characteristics.

translation, and saturation region due to short-channel effect caused by decrease of $\text{In}_{0.53}\text{Ga}_{0.47}\text{As}$ channel length are also investigated.

2. Method and Device Structure

Schematic device structure of the $\text{In}_{0.53}\text{Ga}_{0.47}\text{As}$ MOSFET is shown in Figure 1. The thickness of unintentionally doped $\text{In}_{0.53}\text{Ga}_{0.47}\text{As}$ channel layer, silicon IPL, and HfO_2 gate oxide layer is 200 nm, 1 nm, and 10 nm, respectively. All the lengths of gate L_g , source L_s , and drain L_d are equal to 5 μm . The extended length L_{ext} between source and drain contacts is 10 μm . The doping concentration in source and drain areas is $5 \times 10^{18}/\text{cm}^3$. The transverse width of this MOSFET W is 600 μm . Physical models applied in our simulation include drift-diffusion equation, band gap narrowing (OldSlotboom),

doping-dependent degradation and high field saturation for mobility, Fowler-Nordheim tunneling model for gate leakage current, and Shockley-Read-Hall (SRH) recombination models [14].

3. Results and Discussion

Figure 2 shows output and transfer characteristics with a thickness of Si IPL varying from 0.5 nm to 2.5 nm at a fixed gate or drain voltage. Maximum drain current, I_{ds} , increases linearly with the decrease of thickness of Si IPL as shown in the first inset. This increase can be accounted for by the increase of electric field strength under gate electrode with decrease of thickness of Si IPL, which subsequently raises the electron concentration induced in $\text{In}_{0.53}\text{Ga}_{0.47}\text{As}$ channels. The interpretation can also explain the increase of power-up

current I_{on} and leakage current I_{off} with decrease of thickness of Si IPL in the transfer characteristics curves in the second inset. Simultaneously, the effect of Si IPL as a barrier layer between oxygen and $In_{0.53}Ga_{0.47}As$ layers may be diminished by the decrease of its thickness. The significant increases of I_{off} when the gate voltages V_g approach larger negative voltages, as the arrow indicates, are attributed to the depletion in the drain area close to gate electrode in $In_{0.53}Ga_{0.47}As$ channels, which increases tunneling probability of carriers between drain and gate electrode [15]. Therefore, the determination of thickness of Si IPL should be a result of compromise between drain currents and role of a barrier layer. A value between 1.0 nm and 1.5 nm is suggested to be set for the thickness of Si IPL based on above simulation results.

Figure 3 shows output and transfer characteristics with a thickness of gate oxide HfO_2 layer varying from 5 nm to 25 nm at a fixed gate or drain voltage. Due to the variation of electric field strength under gate electrode, maximum drain current I_{ds} and power-up current I_{on} increase with decrease of thickness of HfO_2 layer. Stronger I_{ds} and I_{on} are beneficial to improving device performance of $In_{0.53}Ga_{0.47}As$ MOSFETs. Leakage current I_{off} also exhibits sharp increase with decrease of thickness of HfO_2 layer as explained in Figure 2, especially when the thickness is reduced to 5 nm. This occurrence is not desired to improve device performance. Based on these results, an ideal value of thickness of HfO_2 layer should be kept larger than 10 nm.

Figure 4 shows influences of doping depth of source and drain layer on output and transfer characteristics at a fixed gate or drain voltage. The decrease of doping depth of source and drain layers leads to a decrease of maximum drain current I_{ds} and an increase of turn-on voltage V_{on} . The former decrease is negative for device development, whereas the latter increase is desired for it is helpful to enlarge the linear operation zone of $In_{0.53}Ga_{0.47}As$ MOSFETs. Different from the aforementioned effects of Si IPL thickness and HfO_2 thickness, the doping depth of source/drain layer has obvious influence on I_{on} instead of I_{off} . I_{on} increases quickly with increase of doping depth. Therefore, a larger doping depth in source and drain layers is preferred for improving device performance. However, increase of doping depth is restricted by the geometrical sizes of $In_{0.53}Ga_{0.47}As$ MOSFETs themselves.

Figure 5 shows influences of doping concentration of source and drain layer on output and transfer characteristics at a fixed gate or drain voltage. The increase of doping concentration produces a desired increase of maximum drain current I_{ds} and an undesired decrease of turn-on voltage V_{on} . As a result for balance between I_{ds} and V_{on} , a middle-value doping concentration is preferred in practice. When the doping concentration increases ten times from $5 \times 10^{18}/cm^3$ to $5 \times 10^{19}/cm^3$, I_{ds} only increases about 40%, indicating that impurity scattering which inhibits electrical current increasing begins to dominate [16]. Here, the doping concentration of source/drain layer also has obvious influence on I_{on} instead of I_{off} as previous doping depth.

Figure 6 shows influences of channel length on output and transfer characteristics at a fixed gate or drain voltage.

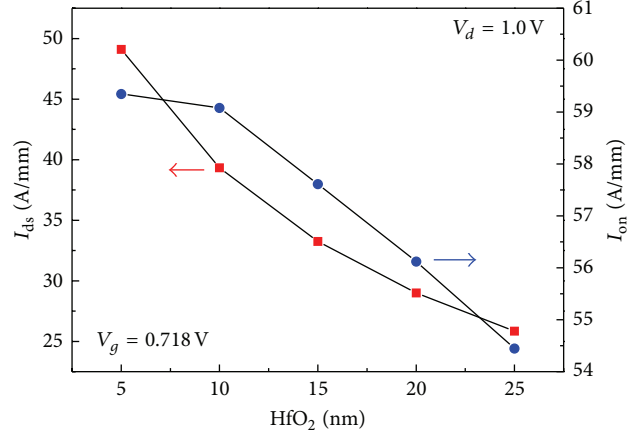


FIGURE 3: Gate oxide HfO_2 thickness dependence on output and transfer characteristics.

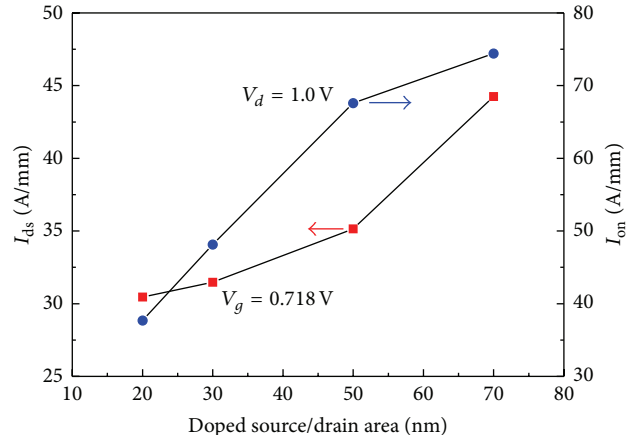


FIGURE 4: Source/drain layer doping depth dependence on output and transfer characteristics.

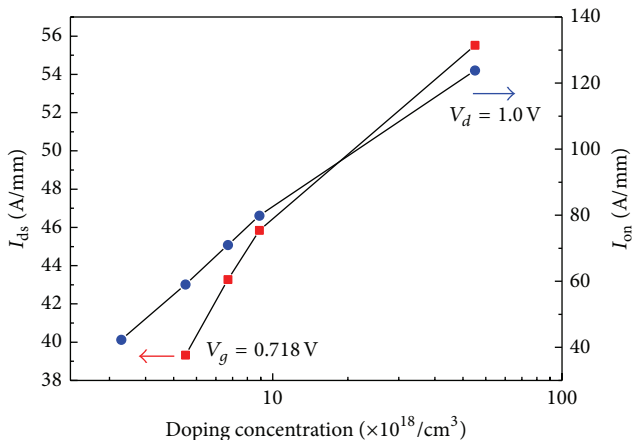


FIGURE 5: Source/drain layer doping concentration dependence on output and transfer characteristics.

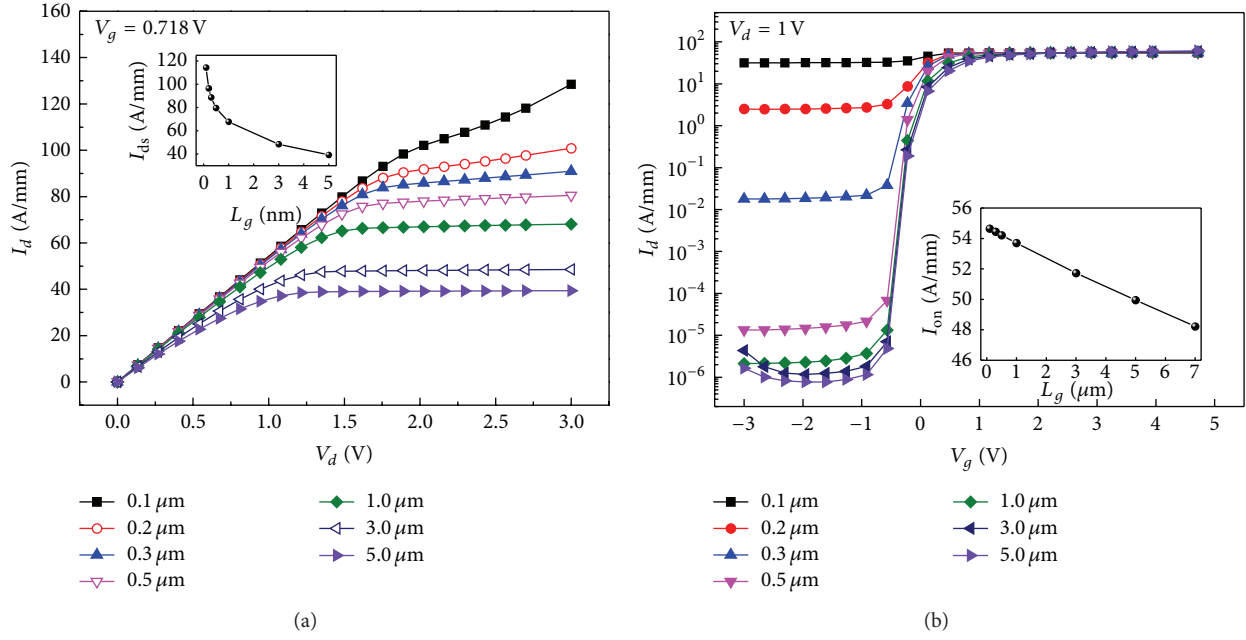


FIGURE 6: Channel length dependence on output (a) and transfer (b) characteristics.

Saturated drain current I_{ds} and saturated voltage V_s both increase with the decrease of channel length. The appearance of saturated drain current is a result of unvaried pinch-off voltage at the point where the potential drop across the oxide at the drain terminal is equal to threshold voltage V_T . When the channel length is further lessened down from $0.5 \mu\text{m}$ to $0.1 \mu\text{m}$, the depletion region at the drain terminal extends laterally into the channel, reducing the effective channel length and causing the drain current to be no more saturated. This is the so-called channel length modulation that drain currents begin to move upward with increase of drain voltage when the channel length is substantially shortened as Figure 6(a) illustrates. Meanwhile, the reduction of channel length causes the drain terminations to be closer to source terminations, producing an obvious increase of leakage current I_{off} and weaker effect of gate electrode on drain currents, as Figure 6(b) shows. Power-up current I_{on} shows a linear relationship with channel length. This is consistent with previous reports [14].

Figure 7 shows influences of channel length on threshold voltage V_T and subthreshold characteristics ∇V_T at a fixed drain voltage. A transverse shift of subthreshold characteristics ∇V_T is observed for different channel lengths, an important feature of drain induced barrier lowering (DIBL) effect. The DIBL effect is a result of increase of injected electrons from source area to channel induced by lowering of potential barrier height between drain and source electrodes when the channel length is lessened [17]. The shift of subthreshold characteristics ∇V_T starts to become most obvious and the device performance degrades quickly when the channel length is lessened down to a critical value of $0.5 \mu\text{m}$, much bigger than that of Si-based npn MOSFETs [18, 19]. In the InGaAs-based MOSFETs, the channel layer InGaAs is unintentionally doped whereas the channel layer in Si-based devices is p -type doped,

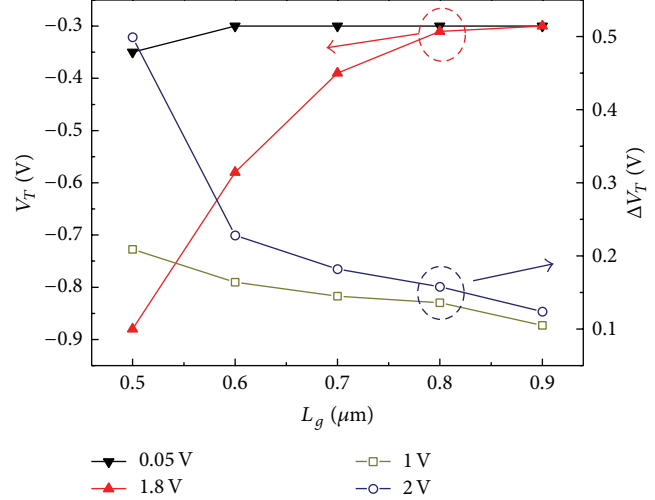


FIGURE 7: Channel length dependence on threshold voltage and shift of subthreshold characteristics.

which will induce less Fermi energy difference between drain and source electrodes. Then the corresponding potential barrier height in the InGaAs MOSFETs is comparatively smaller than that of Si-based MOSFETs [20–22]. This is the physical mechanism where DIBL effect is much obvious in the InGaAs MOSFETs. Threshold voltage V_T experiences a similar sudden decrease when the channel length is lessened down to the same value of $0.5 \mu\text{m}$. These results mean that the InGaAs MOSFETs start to show short channel effect at a value of $0.9 \mu\text{m}$ of channel length and reach their operating limits when the channel length is further lessened down to $0.5 \mu\text{m}$.

4. Conclusion

In conclusion, the electrical characteristics of $\text{In}_{0.53}\text{Ga}_{0.47}\text{As}$ MOSFET grown with Si IPL and high k gate oxide HfO_2 layer have been investigated in detail. The decrease of Si IPL thickness and gate oxide HfO_2 thickness is beneficial to improving device performance by increasing the maximum drain current. However, rather small Si IPL thickness and gate oxide HfO_2 thickness result in sharp increase of leakage current and device performance degradation. The increase of source and drain layer doping depth brings about larger maximum drain current and almost has little negative influence on saturated voltage and leakage current. Unfortunately, increase of doping depth is limited by the geometrical size of MOSFETs themselves. The increase of source and drain layer doping concentration also has dual influences. On the one hand, it helps to improve the maximum drain current. On the other hand, it produces a lowered saturated voltage and smaller device linear operating limits. The decrease of channel length increases the maximum drain current and leakage current simultaneously. Short channel effects start to appear when the channel length is lessened down to about $0.9\ \mu\text{m}$ and experience sudden sharp increases which make device performance degrade and reach their operating limits when the channel length is further lessened down to $0.5\ \mu\text{m}$.

Conflict of Interests

The authors declare that there is no conflict of interests regarding the publication of this paper.

Acknowledgments

This work was supported in part by the National Natural Science Foundation of China (Grant nos. 11104150, 11274330, and 61474067), the Key Natural Science Foundation of the Jiangsu Higher Education Institutions of China (Grant no. 14-KJA510005), and the National Basic Research Program of China (Grant no. 2011CBA00700).

References

- [1] F. Zhu, H. Zhao, I. Ok et al., "A high performance $\text{In}_{0.53}\text{Ga}_{0.47}\text{As}$ metal-oxide-semiconductor field effect transistor with silicon interface passivation layer," *Applied Physics Letters*, vol. 94, no. 1, Article ID 013511, 2009.
- [2] Y. Xuan, P. D. Ye, and T. Shen, "Substrate engineering for high-performance surface-channel III-V metal-oxide-semiconductor field-effect transistors," *Applied Physics Letters*, vol. 91, no. 23, Article ID 232107, 2007.
- [3] H. Xia, Z.-Y. Lu, T.-X. Li et al., "Distinct photocurrent response of individual GaAs nanowires induced by n-type doping," *ACS Nano*, vol. 6, no. 7, pp. 6005–6013, 2012.
- [4] J. Miao, W. Hu, N. Guo et al., "Single InAs nanowire room-temperature near-infrared photodetectors," *ACS Nano*, vol. 8, no. 4, pp. 3628–3635, 2014.
- [5] J. Miao, W. Hu, and N. Guo, "High-responsivity graphene/InAs nanowire heterojunction near-infrared photodetectors with distinct photocurrent on/off ratios," *Small*, 2014.
- [6] Z. Liu, T. Luo, B. Liang et al., "High-detectivity InAs nanowire photodetectors with spectral response from ultraviolet to near-infrared," *Nano Research*, vol. 6, no. 11, pp. 775–783, 2013.
- [7] N. Guo, W. Hu, L. Liao et al., "Anomalous and highly efficient InAs nanowire phototransistors based on majority carrier transport at room temperature," *Advanced Materials*, vol. 26, no. 48, pp. 8203–8209, 2014.
- [8] H. Zeng, G. Duan, Y. Li, S. Yang, X. Xu, and W. Cai, "Blue luminescence of ZnO nanoparticles based on non-equilibrium processes: defect origins and emission controls," *Advanced Functional Materials*, vol. 20, no. 4, pp. 561–572, 2010.
- [9] H. Zeng, C. Zhi, Z. Zhang et al., "White graphenes: boron nitride nanoribbons via boron nitride nanotube unwrapping," *Nano Letters*, vol. 10, no. 12, pp. 5049–5055, 2010.
- [10] Z. Liu, J. Xu, D. Chen, and G. Shen, "Flexible electronics based on inorganic nanowires," *Chemical Society Reviews*, vol. 44, no. 1, pp. 161–192, 2015.
- [11] N. Taoka, M. Harada, Y. Yamashita, T. Yamamoto, N. Sugiyama, and S.-I. Takagi, "Effects of Si passivation on Ge metal-insulator-semiconductor interface properties and inversion-layer hole mobility," *Applied Physics Letters*, vol. 92, no. 11, Article ID 113511, 2008.
- [12] J. Ivanco, T. Kubota, and H. Kobayashi, "Deoxidation of gallium arsenide surface via silicon overlayer: a study on the evolution of the interface state density," *Journal of Applied Physics*, vol. 97, no. 7, Article ID 073712, 2005.
- [13] Y. Xuan, Y. Q. Wu, H. C. Lin, T. Shen, and P. D. Ye, "Submicrometer inversion-type enhancement-mode InGaAs MOSFET with atomic-layer-deposited Al_2O_3 as gate dielectric," *IEEE Electron Device Letters*, vol. 28, no. 11, pp. 935–938, 2007.
- [14] C.-H. Yu, Q.-Z. Luo, X.-D. Luo, and P.-S. Liu, "Donor-like surface traps on two-dimensional electron gas and current collapse of AlGaN/GaN HEMTs," *The Scientific World Journal*, vol. 2013, Article ID 931980, 6 pages, 2013.
- [15] Y.-K. Choi, D. Ha, T.-J. King, and J. Bokor, "Investigation of gate-induced drain leakage (GIDL) current in thin body devices: single-gate ultra-thin body, symmetrical double-gate, and asymmetrical double-gate MOSFETs," *Japanese Journal of Applied Physics*, vol. 42, no. 4, pp. 2073–2076, 2003.
- [16] W. Hu, X. Chen, X. Zhou, Z. Quan, and L. Wei, "Quantum-mechanical effects and gate leakage current of nanoscale n-type FinFETs: a 2d simulation study," *Microelectronics Journal*, vol. 37, no. 7, pp. 613–619, 2006.
- [17] M. Si, J. J. Gu, X. Wang et al., "Effects of forming gas anneal on ultrathin InGaAs nanowire metal-oxide-semiconductor field-effect transistors," *Applied Physics Letters*, vol. 102, no. 9, Article ID 093505, 2013.
- [18] A. D. Franklin, M. Luisier, S.-J. Han et al., "Sub-10 nm carbon nanotube transistor," *Nano Letters*, vol. 12, no. 2, pp. 758–762, 2012.
- [19] S. H. Park, Y. Liu, N. Kharche et al., "Performance comparisons of III-V and strained-Si in planar FETs and nonplanar FinFETs at ultrashort gate length (12 nm)," *IEEE Transactions on Electron Devices*, vol. 59, no. 8, pp. 2107–2114, 2012.
- [20] T. Yamada, Y. Nakajima, T. Hanajiri, and T. Sugano, "Suppression of drain-induced barrier lowering in silicon-on-insulator MOSFETs through source/drain engineering for low-operating-power system-on-chip applications," *IEEE Transactions on Electron Devices*, vol. 60, no. 1, pp. 260–267, 2013.

- [21] F. Xue, A. Jiang, H. Zhao et al., "Sub-50-nm MOSFETs with various barrier layer materials," *IEEE Electron Device Letters*, vol. 33, no. 1, pp. 32–34, 2012.
- [22] S. Tewari, A. Biswas, and A. Mallik, "Impact of different barrier layers and indium content of the channel on the analog performance of InGaAs MOSFETs," *IEEE Transactions on Electron Devices*, vol. 60, no. 5, pp. 1584–1589, 2013.

Research Article

Photoelectric Characteristics of Double Barrier Quantum Dots-Quantum Well Photodetector

M. J. Wang, F. Y. Yue, and F. M. Guo

Shanghai Key Laboratory of Multidimensional Information Processing, Key Laboratory of Polar Materials & Devices, School of Information Science Technology, East China Normal University, No. 500, Dong Chuan Road, Shanghai 200241, China

Correspondence should be addressed to F. M. Guo; fmguo@ee.ecnu.edu.cn

Received 26 November 2014; Accepted 6 January 2015

Academic Editor: Wen Lei

Copyright © 2015 M. J. Wang et al. This is an open access article distributed under the Creative Commons Attribution License, which permits unrestricted use, distribution, and reproduction in any medium, provided the original work is properly cited.

The photodetector based on double barrier AlAs/GaAs/AlAs heterostructures and a layer self-assembled InAs quantum dots and $In_{0.15}Ga_{0.85}As$ quantum well (QW) hybrid structure is demonstrated. The detection sensitivity and detection ability under weak illuminations have been proved. The dark current of the device can remain at 0.1 pA at 100 K , even lower to $3.05 \times 10^{-15}\text{ A}$, at bias of -1.35 V . Its current responsivity can reach about $6.8 \times 10^5\text{ A/W}$ when 1 pw 633 nm light power and -4 V bias are added. Meanwhile a peculiar amplitude quantum oscillation characteristic is observed in testing. A simple model is used to qualitatively describe. The results demonstrate that the InAs monolayer can effectively absorb photons and the double barrier hybrid structure with quantum dots in well can be used for low-light-level detection.

1. Introduction

Low dimensional nano-scaled III-V semiconductor is a promising candidate material for future high-performance electronics and optoelectronics, including high-mobility field-effect transistors (FETs), long-wavelength infrared photodetectors, and phototransistors [1–5]. Currently, there is great interest in exploring highly sensitive photodetector for potential applications in remote sensing, spectroscopy, and even air quality monitoring in industrial or medical and pro-environment detection. In order to approach the photon counting mode, the very high photoexcited carrier multiplication factor is a basic requirement [6, 7]. Recently, it has been demonstrated that resonant tunneling structure containing a layer of self-assembled quantum dots (QDs) may be used as a very high photoexcited carrier multiplication for low-light-level detection [8–12].

In the present work we discuss peculiar photoelectric conversion characteristics in the double AlAs barrier, self-assembled InAs QDs, and $In_{0.15}Ga_{0.85}As$ QW hybrid structure. When the detector is illuminated with an energy which exceeds GaAs band gap, the photoexcited electrons and holes are generated in the undoped GaAs layers on each side of two AlAs barriers. The photoexcited electrons drift or tunnel

by bias toward the lower potential energy and eventually would be captured by the $In_{0.15}Ga_{0.85}As$ QW. The similar process also occurs to holes, except that holes drift on the opposite direction and are trapped in the InAs QDs. Due to the spatial separation of electrons and holes, as well as the additional in-plane localization provided by the QDs, the excess electrons and holes could be stored for enough long time. These photovoltaic effects in the wide GaAs quantum well should have each imprint on the photoelectric response. The electrons and holes trapped separately within the $In_{0.15}Ga_{0.85}As$ QW and InAs QDs induce a potential which affects the tunneling characteristics [9, 10]. We can see that the trapped charge strongly affects the tunnel current of the detector which allows for the weak light detection.

The larger current oscillations appear when the detector is illuminated with a 633 nm He-Ne laser under certain conditions. It originates from quantized ballistic motion of photoexcited carriers and is qualitatively different from RTD [3–10]. More than dozens of resonant peaks reveal regions of negative differential conductance in the photocurrent as bias changed from -2 V to 2.5 V and about 100 K temperature. The quantum oscillation appears with typical peak-to-peak voltage interval $\Delta V_{pp} \approx 100\text{ mV}$. The electron (and hole) energy levels confined with high quantum numbers successively

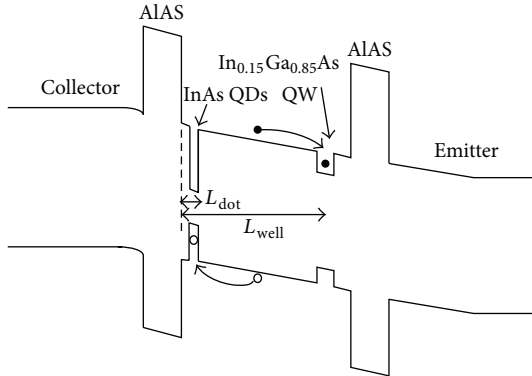


FIGURE 1: Schematic diagram of the capturing of an electron and hole photoexcited in a QW and QD under bias.

reach the top of the triangular potential as electric field increased. It causes the tails of the Airy-type wave functions near the classical turning point of the potential to overlap strongly with the high density of free majority carriers in the nearby n doped electrodes. The enhancement of the recombination rate leads to a modulation of the photocurrent measured as a function of applied bias. A model is constructed based on methods of mathematical physics to explain the photocurrent oscillations [10–12].

2. Device Test

The photodetector was grown by MBE on an n^+ -type (1 0 0) GaAs substrate; a typical layer structure consists of a 1 μm thick Si-doped (10^{18} cm^{-3}) GaAs buffer layer at the bottom, an undoped 30 nm GaAs spacer, a 25 nm AlAs barrier, a 3 nm GaAs interlayer, a 6 nm $\text{In}_{0.15}\text{Ga}_{0.85}\text{As}$ QW, a 45 nm GaAs wide well, 1.8 ML self-assembled InAs QD layer, a 5 nm GaAs overlayer, and the second 25 nm AlAs barrier. On the top, 30 nm undoped GaAs and 30 nm Si-doped (10^{18} cm^{-3}) GaAs were deposited as the capping layer. Ohmic contacts were made both on the top and at the bottom of the detector meanwhile. A rectangular aperture ($50 \times 500 \mu\text{m}^2$) was left on the top surface for optical access [10, 13]. The band diagram profile of the detector along its epitaxial growth direction is shown in Figure 1.

The 633 nm He-Ne laser beam with 50 μm diameter was focused on the photosensitive window of the detector. When the bias is at ± 1.7 V, the electric field reaches $1 \times 10^7 \text{ V/m}$ and the photoexcited electrons and holes are generated in the undoped GaAs layers on each side of the AlAs barriers. The photocurrent-voltage curves of the detector can be recorded by Keithley 4200-SCS. Figure 2 shows the I - V characteristics at incidence light power changing from 0.1 picowatt (pW) to 100 nanowatt (nW). When the bias voltages range from below +1 V to -1.5 V reverse biases, the dark current remains 0.1 pA although the active area is very large ($50 \times 500 \mu\text{m}^2$). When the detector is biased at -1.35 V, the minimum dark current is only $3.05 \times 10^{-15} \text{ A}$. We can still see when the light power exceeds 40 pW, the oscillatory photocurrent occurs at bias voltages ranging from -2 V to 2.5 V. The oscillatory amplitude

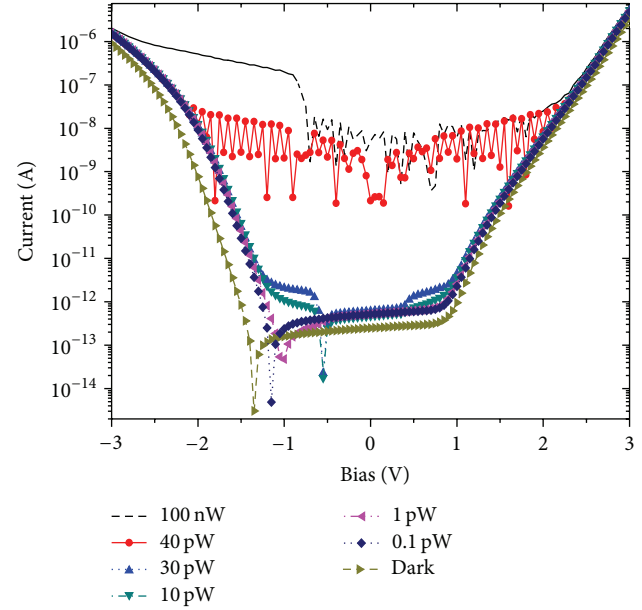


FIGURE 2: The I - V curves at different illumination power.

also decreases substantially when the bias exceeds 2.5 V or is lower than -2 V. The oscillatory characteristic disappears when light power decreases lower than 40 pW and exceeds 100 nW at bias voltage of -0.6 V.

We can see a reverse bias current valley shifted which changed with illumination power as shown in Figure 2. And the valley shifted more evident as stronger illumination. It represents that the photoexcited holes trapped in the QDs lead to the energy bands downward shift localized, such that a lower bias is required for the detector to reach the large tunneling current [1–7].

Figure 3 shows the higher responsivity of the detector at low-light-level illumination. The current responsivity is larger than $6.8 \times 10^5 \text{ A/W}$ when 633 nm light power with 1 pw at -3 V bias is employed. Because an idea quantum efficiency $\eta = 1$, the spectral response $R_{\lambda=633 \text{ nm}}$ is expected to be 0.51 A/W according to [14]

$$\eta = \frac{I_p/e}{P/h\nu} = \frac{Ihc}{gPe\lambda} = \frac{R}{g} \frac{hc}{e\lambda} = \frac{R}{g} \frac{1.24}{\lambda (\mu\text{m})}. \quad (1)$$

The gain of the detector can be estimated at least 1.3×10^6 . Further, the ratio of the photocurrent versus the dark current can be calculated as shown in Figure 3. When the detector is biased at -1.35 V, the minimum dark current can be gained and then the magnitude of the photocurrent versus the dark current is the largest at this moment.

Figure 4 plots the photocurrent spectra of the detector at 77 K using Bruker FITR Vertex 80 V. The detector shows a good response in the spectral range from 550 nm up to over 930 nm. The photocurrent peak at 818 nm is from the GaAs bulk layer, while the peaks at 873 nm and 925 nm should be attributed to the $\text{In}_{0.15}\text{Ga}_{0.85}\text{As}$ QW and InAs QDs. By the photocurrent spectra, we estimated that the current responsivity at ~925 nm is dozen times more than 633 nm and

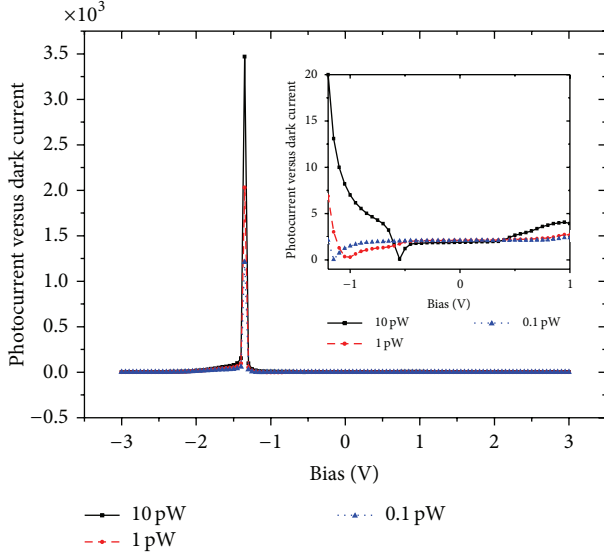


FIGURE 3: Ratio of the photocurrent versus dark current at illumination 55 pW and bias changed from -3 V to 3 V. The inset shows the enlargement of section bias range from -1.2 V to 1 V.

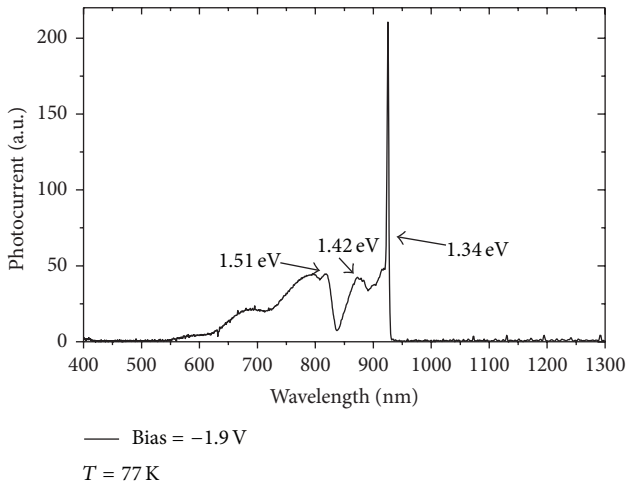


FIGURE 4: Representative photocurrent spectrum of the detector at $T = 77$ K.

thus potentially provides even higher sensitivity. The result indicates that it is a promising detector for sensitive visible to near-infrared imaging applications.

3. Analysis

3.1. Sensitivity. According to Figure 1, a simple model is presented for the detector with one layer of InAs QDs and thin $\text{In}_{0.15}\text{Ga}_{0.85}\text{As}$ QW embedded at distances L_{dot} and L_{well} from one side of AlAs barrier. The QDs layer width is neglectful for simplicity, such that QDs spatial distribution and narrow QW can be modeled by means of a delta function.

Poisson's equation with the boundary conditions is as follows [15, 16]:

$$\frac{d^2\varphi}{dx^2} = -\frac{eN_d}{\epsilon\epsilon_0} - \frac{ep_{\text{dot}}}{\epsilon\epsilon_0}\delta(x - L_{\text{dot}}) + \frac{en_{\text{well}}}{\epsilon\epsilon_0}\delta(x - L_{\text{well}}), \quad (2)$$

$$\varphi(w) = 0, \quad (3)$$

$$\left.\frac{d\varphi}{dx}\right|_{x=w} = 0. \quad (4)$$

The charge density in the right-hand side of Poisson's equation consists of three components: N_d is the constant charge density of ionized impurity; p_{dot} and n_{well} are the charge density accumulating in QDs and $\text{In}_{0.15}\text{Ga}_{0.85}\text{As}$ QW, respectively. The solution of (2) can be obtained by boundary conditions shown in (3) and (4):

$$\begin{aligned} \varphi(x) \approx & -\frac{eN_d}{\epsilon\epsilon_0}(x - w)^2 \\ & + \begin{cases} 0, & x > L_{\text{well}}, \\ -\frac{en_{\text{dot}}}{\epsilon\epsilon_0}(L_{\text{dot}} - x), & x < L_{\text{dot}}, \\ \frac{en_{\text{dot}}}{\epsilon\epsilon_0}(L_{\text{well}} - x), & L_{\text{dot}} < x < L_{\text{well}}. \end{cases} \end{aligned} \quad (5)$$

At a larger negative bias, the photoexcited electrons will drift or tunnel toward the side of the lower potential energy and eventually would be captured by the $\text{In}_{0.15}\text{Ga}_{0.85}\text{As}$ QW. The photoexcited holes will drift on opposite direction and be trapped in the InAs QDs. At weak illumination, the QDs and QW layer make little effect on the potential profile because of the very low p_{dot} and n_{well} . As the laser intensity increases, the photoexcited electron-hole pair increases, which means p_{dot} and n_{well} become larger, and induces ΔV photovoltaic effect near the dots, as $x = 0$:

$$\Delta V \approx -\frac{ep_{\text{dot}}}{\epsilon\epsilon_0}L_{\text{dot}}. \quad (6)$$

As the negative bias decreases, the InAs dots capture more holes and the potential near the dots is pulled down gradually. The $\text{In}_{0.15}\text{Ga}_{0.85}\text{As}$ QW captures more electrons and the potential near the QW is pulled up. Such a large ΔV is enough to increase voltage drop of AlAs barrier. That will influence the tunneling process through the AlAs barrier. The higher photosensitivity of the detector indicates a long dwell time of a photoexcited hole following capture at one of the dots. Under appropriate bias voltage, the average electric field in the active region (120 nm wide) of the detector is 10^7 V/cm. Assuming that the mobility of electron and hole is $8000 \text{ cm}^2/\text{V}\cdot\text{s}$ and $400 \text{ cm}^2/\text{V}\cdot\text{s}$, respectively, their transit times are correspondingly about 1×10^{-14} s and 1×10^{-13} s, which is on a much shorter time than the electron-hole recombination time of about 1×10^{-9} s [10, 15, 16]. Since the transition time is about four orders of magnitude shorter than the electron-hole recombination time, it allows a very high multiplication in detector. At a larger positive bias, the photoexcited electrons will be captured by the InAs QDs and

the photoexcited holes will drift on the opposite direction and be trapped in the $\text{In}_{0.15}\text{Ga}_{0.85}\text{As}$ QW.

For stronger confined ability of QDs compared to QW, the InAs dots capture more holes at negative bias than $\text{In}_{0.15}\text{Ga}_{0.85}\text{As}$ QW at positive bias, and it can get higher detector responsivity in reverse bias.

3.2. Current Oscillations. Under lower level photoexcitation, the space charge density induced by the photoexcited carriers is relatively small. We assume a constant electric field F_z in the intrinsic regions on each side of the barrier layer. We can model for carrier quantization in the formed potential wells by using analytical solutions of the Schrödinger equation at an infinite triangular quantum well. The quantization energies E_j and eigenfunctions $\psi_j(z)$ due to the z component of the carrier motions are given by [12]

$$-\left[\frac{\hbar^2}{2m_e^*} \frac{\partial^2}{\partial z^2} + V(z) \right] \psi(z) = E\psi(z). \quad (7)$$

The photoexcited electrons occupy the quantized energy subbands j of the triangular potential well. They are influenced by low dimensional quantum effects. The energy of carriers in each subband is given by [12]

$$E_j = \left(\frac{\hbar^2}{2m^*} \right)^{1/3} \left[\frac{3}{2} \pi q F_s \left(j + \frac{3}{4} \right) \right]^{2/3}, \quad j = 0, 1, 2, \dots \quad (8)$$

The eigenfunctions $\psi_j(z)$ are given by Airy functions:

$$\psi_j(z) = Ai \left[\frac{2m^* q F_z}{\hbar^2} \left(z - \frac{E_j}{q F_z} \right) \right]. \quad (9)$$

Energy level spacing of carriers in each subband is given by

$$\Delta E_j \approx \left(\frac{\hbar^2}{2m^*} \right)^{1/3} \left[\frac{3}{2} \pi q F_s \left(j + \frac{3}{4} \right) \right]^{-1/3} \pi q F_z. \quad (10)$$

At appropriate bias voltage, an excited state subband with quantum number j_m and energy E_{jm} reaches the top of the triangular quantum well and joins the continuum state of extended electrons above (and below) the conduction (and valence) band edge in the doped electrodes. The voltage interval $V_j - V_{j+1}$, over successive $(j+1)$ th and j th levels, reaches the ionization energy, and it can then be estimated and compared with the measured voltage interval ΔV_{pp} between the peaks of the photocurrent.

As electric field F_z increasing, the Airy function state j of a particular hole approaches the top of its triangular potential well and its wave function increasingly overlaps with the high density of majority electrons in the doped n -GaAs electrode. The overlap increases the recombination rate of the photoexcited holes in the j_m th subband, thus reducing their contribution to the photocurrent by tunneling through the AlAs barrier. As the voltage varies, successive Airy function energy levels approach the top of the triangular potential well and join a continuum state of extending the unbounded

states in the GaAs conduction band. Hence the competition between tunneling and the bias-dependent modulation of the recombination rate repeats itself, which gives rise to the observed oscillatory photocurrent [12, 17–20].

In addition, the detector may be analogous to N-I-N structure. The photoexcited electrons overlap between the tails of their wave functions and the minority holes in the n -doped layers are very small. The electrons recombination rate with minority holes in the n -GaAs layer is too low to modulate the photocurrent.

As the light power decreases lower than 40 pW as shown in Figure 2, the space charge density induced by the carrier density photoexcited is very small. The recombination current is too low to modulate the photocurrent. This leads to no observation of photocurrent oscillations.

As photoexcitation range changed from 40 pW to 100 nW, the oscillatory amplitude decreases evidently when bias voltage exceeds 2.5 V or becomes lower than -2 V. At higher bias the highest energy states in the triangular potential well are no longer confined by the AlAs barrier so the photocurrent increases rapidly. We note that carriers scattering at the heterointerface between the QD and the surrounding AlAs matrix strongly affects the radiative recombination of photoexcited carriers. A possible explanation for the oscillatory effect is that the QD layer gives rise to a scattering potential which enhances the elastic scattering-assisted tunneling [12].

It is also interesting to note that photocurrent oscillates at bias voltages that range from -0.6 V to 2.5 V and disappears at -0.6 V negative bias whose higher photoexcitation state is ~100 nW. The photoexcited electron-hole pairs induce larger ΔV photovoltaic changed, so the tunneling current increases rapidly and the recombination current is too low to modulate the photocurrent.

4. 64-Pixel Line Readout

To read out the weak light response, a 1×64 array readout circuit and an on-chip integrated system for data processing with low noise and high precision are designed. Figure 5 is the readout response voltage of the 64-pixel line with laser beam power at ~1 nw, the integration time 29 μ s, and indoor temperature. Due to the working point of inconsistencies for some pixels, their readout voltage is saturated and premature. The inset shows the response voltage of the most normal pixel. The response voltage is changed in approximate linear when the light power changed from 10 pw to 100 pw. The response voltage is 27 mV at 10 pw illumination beam power and 35 μ s integration time. The voltage responsivity reaches about 2.7×10^9 V/W.

5. Conclusion

We have measured and analyzed the photoelectric characteristics of the AlAs/GaAs/AlAs double barrier structure photodetector, which contains a layer of self-assembled InAs QD and thin $\text{In}_{0.15}\text{Ga}_{0.85}\text{As}$ QW in AlAs double barriers. The higher sensitivity is caused by the charge effect of the photoexcited holes and electrons captured by surrounding

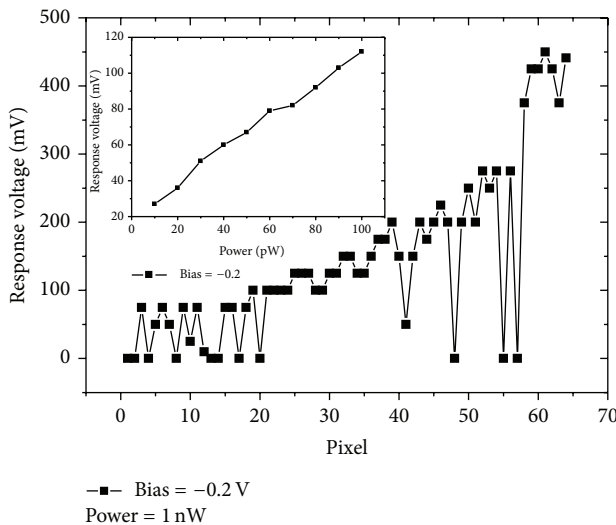


FIGURE 5: Readout voltage of the 64-pixel linear array at 1 nW illuminated beam (633 nm) power. The inset shows the 61th pixel response voltage at indoor temperature and laser (633 nm) power changed from 10 pw to 100 pw.

QDs and $\text{In}_{0.15}\text{Ga}_{0.85}\text{As}$ QW, respectively. The oscillations appear when the detector is illuminated with 633 nm He-Ne laser beam at certain bias and incidence. The competition between tunneling and the bias-dependent modulation of the recombination rate repeats itself giving rise to the oscillatory photocurrent observed. Further, we find the photocurrent tails up to 930 nm wavelength with high sensitivity. The readout results demonstrate that the photodetector shows good sensitivity when light power (633 nm) is as low as 10 pW at indoor temperature.

Conflict of Interests

The authors declare that there is no conflict of interests regarding the publication of this paper.

Acknowledgments

This work was supported by the National Scientific Research Plan (2011CB932903), the Scientific and Technological Commission of Shanghai (no. 118014546), the Natural Science Foundation of China (61376103), the State Key Laboratory of Functional Materials for Informatics, and Laboratory for Terahertz Solid State Technology Chinese Academy of Science.

References

- [1] E. E. Vdovin, A. Levin, A. Patane et al., "Imaging the electron wave function in self-assembled quantum dots," *Science*, vol. 290, no. 5489, pp. 122–124, 2000.
- [2] J. C. Blakesley, P. See, A. J. Shields et al., "Efficient single photon detection by quantum dot resonant tunneling diodes," *Physical Review Letters*, vol. 94, no. 6, Article ID 067401, 2005.
- [3] S. S. Hees, B. E. Kardynal, P. See, A. J. Shields, I. Farrer, and D. A. Ritchie, "Effect of InAs dots on noise of quantum dot resonant tunneling single-photon detectors," *Applied Physics Letters*, vol. 89, no. 15, Article ID 153510, 3 pages, 2006.
- [4] N. Guo, W. Hu, L. Liao et al., "Anomalous and highly efficient InAs nanowire phototransistors based on majority carrier transport at room temperature," *Advanced Materials*, vol. 26, no. 48, pp. 8203–8209, 2014.
- [5] J. Miao, W. Hu, N. Guo et al., "Single InAs nanowire room-temperature near-infrared photodetectors," *ACS Nano*, vol. 8, no. 4, pp. 3628–3635, 2014.
- [6] W. Lu, Y. M. Mu, X. Q. Liu et al., "Direct observation of above-quantum-step quasibound states in GaAs/Al_xGa_{1-x}As/vacuum heterostructures," *Physical Review B—Condensed Matter and Materials Physics*, vol. 57, no. 16, pp. 9787–9791, 1998.
- [7] W. Wang, Y. Hou, D. Xiong et al., "High photoexcited carrier multiplication by charged InAs dots in AlAs/GaAs/AlAs resonant tunneling diode," *Applied Physics Letters*, vol. 92, no. 2, Article ID 023508, 2008.
- [8] Q. C. Weng, Z. H. An, D. Y. Xiong et al., "Photocurrent spectrum study of a quantum dot single-photon detector based on resonant tunneling effect with near-infrared response," *Applied Physics Letters*, vol. 105, no. 3, Article ID 031114, 3 pages, 2014.
- [9] T. M. Fromhold, L. Eaves, F. W. Sheard, M. L. Leadbeater, T. J. Foster, and P. C. Main, "Magnetotunneling spectroscopy of a quantum well in the regime of classical chaos," *Physical Review Letters*, vol. 72, no. 16, pp. 2608–2611, 1994.
- [10] B. Hu, X. Zhou, Y. Tang et al., "Photocurrent response in a double barrier structure with quantum dots-quantum well inserted in central well," *Physica E: Low-Dimensional Systems and Nanostructures*, vol. 33, no. 2, pp. 355–358, 2006.
- [11] J. Wen, L. Li, Q. C. Weng, and D. Y. Xiong, "Simulation of resonant tunneling devices: origin of the $I - V$ multi-peak behavior," *Optical and Quantum Electronics*, vol. 45, no. 7, pp. 783–790, 2013.
- [12] E. E. Vdovin, M. Ashdown, A. Patanè et al., "Quantum oscillations in the photocurrent of GaAs/AlAs p-i-n diodes," *Physical Review B—Condensed Matter and Materials Physics*, vol. 89, no. 20, Article ID 205305, 2014.
- [13] H.-Z. Zheng, H.-F. Li, Y.-M. Zhang et al., "Experimental study of tunneling escape through double-barrier resonant-tunneling structures," *Physical Review B*, vol. 51, no. 16, pp. 11128–11131, 1995.
- [14] F. Hartmann, F. Langer, D. Bisping et al., "GaAs/AlGaAs resonant tunneling diodes with a GaInNAs absorption layer for telecommunication light sensing," *Applied Physics Letters*, vol. 100, no. 17, Article ID 172113, 3 pages, 2012.
- [15] A. J. Chiquito, Y. A. Pusep, S. Mergulhão, J. C. Galzerani, and N. T. Moshegov, "Effect of photogenerated holes on capacitance-voltage measurements in InAs/GaAs self-assembled quantum dots," *Physical Review B: Condensed Matter and Materials Physics*, vol. 61, no. 7, pp. 4481–4484, 2000.
- [16] S. D. Lin, V. V. Ilchenko, V. V. Marin et al., "Observation of the negative differential capacitance in Schottky diodes with InAs quantum dots near room temperature," *Applied Physics Letters*, vol. 90, no. 26, Article ID 263114, 3 pages, 2007.
- [17] M. Narihiro, G. Yusa, Y. Nakamura, T. Noda, and H. Sakaki, "Resonant tunneling of electrons via 20 nm scale InAs quantum dot and magnetotunneling spectroscopy of its electronic states," *Applied Physics Letters*, vol. 70, no. 1, pp. 105–107, 1997.

- [18] O. Makarovskiy, E. E. Vdovin, A. Patané et al., "Laser location and manipulation of a single quantum tunneling channel in an InAs quantum dot," *Physical Review Letters*, vol. 108, no. 11, Article ID 117402, 2012.
- [19] G. R. Li, X. Zhou, F. H. Yang, P. H. Tan, H. Z. Zheng, and Y. P. Zeng, "Photo-capacitance response of internal tunnelling coupling in quantum-dot-imbedded heterostructures under selective photo-excitation," *Journal of Physics Condensed Matter*, vol. 16, no. 36, pp. 6519–6525, 2004.
- [20] Y. Tang, H. Zheng, F. Yang, P. Tan, C. Li, and Y. Li, "Electrical manifestation of the quantum-confined Stark effect by quantum capacitance response in an optically excited quantum well," *Physical Review B*, vol. 63, no. 11, Article ID 113305, 4 pages, 2001.

Research Article

Modeling and Design of Graphene GaAs Junction Solar Cell

**Yawei Kuang, Yushen Liu, Yulong Ma, Jing Xu, Xifeng Yang,
Xuekun Hong, and Jinfu Feng**

School of Physics and Electronic Engineering, Changshu Institute of Technology, Changshu 215500, China

Correspondence should be addressed to Jinfu Feng; fengjinfu@cslg.cn

Received 28 November 2014; Accepted 31 December 2014

Academic Editor: Wen Lei

Copyright © 2015 Yawei Kuang et al. This is an open access article distributed under the Creative Commons Attribution License, which permits unrestricted use, distribution, and reproduction in any medium, provided the original work is properly cited.

Graphene based GaAs junction solar cell is modeled and investigated by Silvaco TCAD tools. The photovoltaic behaviors have been investigated considering structure and process parameters such as substrate thickness, dependence between graphene work function and transmittance, and n-type doping concentration in GaAs. The results show that the most effective region for photo photogenerated carriers locates very close to the interface under light illumination. Comprehensive technological design for junction yields a significant improvement of power conversion efficiency from 0.772% to 2.218%. These results are in good agreement with the reported experimental work.

1. Introduction

Graphene, a single atom layer of carbon hexagons, has attracted much attention owing to its unique structure and fascination, such as low resistivity, ultra-high mobility, and near-zero band gap [1]. Graphene has been produced in the form of ultrathin sheets consisting of one or a few atomic layers by chemical vapor deposition or mechanical exfoliation and can be transferred to various substrates, which open a wide field of potential applications such as high performance electronic devices, photosensors, and smart composite [2, 3]. In particular the graphene film has a unique combination of high electrical conductivity and optical transparency in visible and near-infrared regions, which gives it the ability to serve as an active layer for metal-semiconductor (M/S) junction solar cells [4]. Recently, graphene based solar cells had been fabricated on various substrates such as Si [5], CdS [6], and GaAs [7]; much process has been achieved in the past several years. Moreover graphene/semiconductor nanowires heterojunction photoelectric devices have also been achieved [8], which is combined with the unique one-dimensional (1D) structural characteristics and versatile physical properties of 1D nanowires [9–12].

Graphene based junction solar cell could be fabricated at room temperature which shows great potential in light

harvesting and conversion application with the advantage of low cost, facile processibility, and environmental amity. Li et al. reported the first graphene based silicon solar cell with the average power conversion efficiency of about 1.65% [13]. After this work, many effects have been exerted to improve the performance of solar cell by using silicon nanowire array [14], modifying the work function of graphene [15], chemical doping to graphene [16], and so forth. In comparison with currently widely used silicon substrate, GaAs has direct band gap and is highly resistant to radiation which makes it suitable for high efficiency solar cell design and space application. The present technique can also provide the possibility to combine large area graphene with GaAs [17, 18]. Jie group transferred single and bilayer graphene sheets onto n-type GaAs substrates and got a power conversion efficiency of 1.95% [19]. Behura et al. calculated the photovoltaic response of graphene junction using the fundamental models for voltage and current; they pointed out that graphene GaAs heterojunction has a superior photovoltaic behavior to graphene silicon junctions [20].

However, the device based graphene GaAs junction is still far lower in efficiency. The application of graphene in solar cell requires much more investigation on devices especially in structure and technical parameter optimizing. In this work, simulation of graphene GaAs solar cells is carried out with

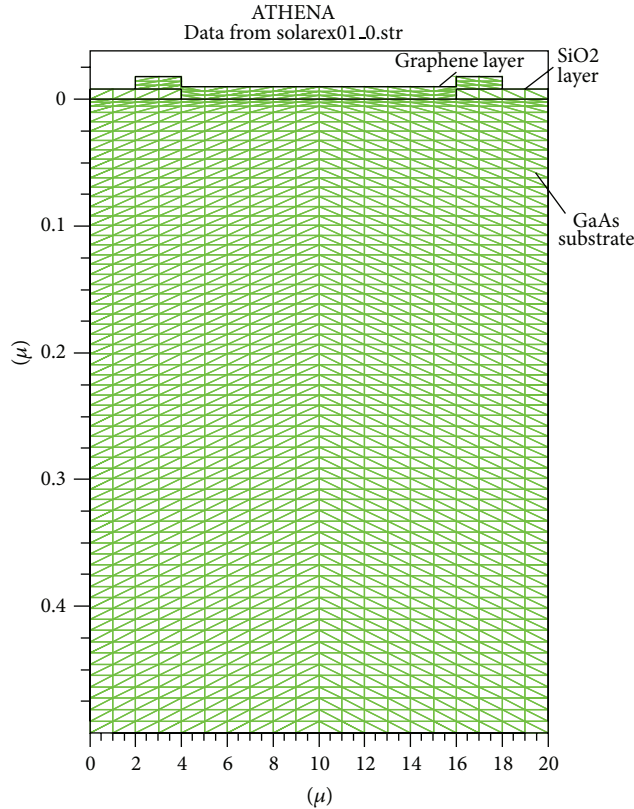


FIGURE 1: Cross section of the graphene GaAs solar cell.

the effect of substrate thickness, graphene transmittance and resistance, and n-type doping concentration. The graphene GaAs solar cell was modeled using Silvaco TCAD tools while the performance of solar cell was improved by parameter optimization.

2. Structure and Modeling

As mentioned above, Figure 1 shows the cross section of the graphene GaAs solar cell simulated using TCAD tools. The device consists of three regions which are Gallium arsenide (GaAs) substrate, SiO_2 window layer, and graphene layer from bottom to the top area, respectively. Here the graphene layer with a thickness of 10 nm was coated onto the silicon substrate with $1\text{ }\mu\text{m} \times 12\text{ }\mu\text{m}$ oxide window which could decrease the surface recombination.

Basically, any semiconductor can form a Schottky junction with a certain metal if their work function difference is big enough and the carrier density of the semiconductor is moderate [21]. GaAs, with a direct band gap of 1.42 ev, is a promising material for optoelectronic device application. Calculations' results indicate that graphene films form a Schottky junction with GaAs, which is favorable for producing a relatively large built-in field [22].

The nonlinear I - V characteristic of the Schottky junction can be expressed by the thermionic emission model:

$$I_s = AA^*T^2e^{-\phi_B/KT}, \quad (1)$$

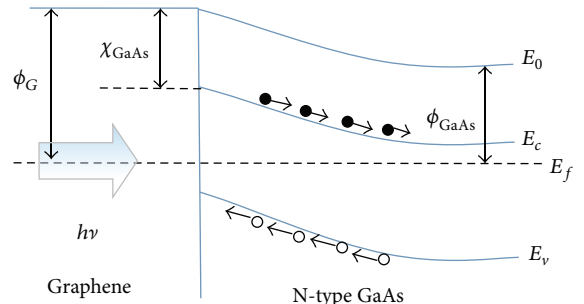


FIGURE 2: Energy diagrams of graphene n-GaAs solar sell.

where A is the contact area, A^* is the effective Richardson constant, T is the absolute temperature, K is Boltzmann constant, and ϕ_B is the barrier height

$$\phi_B = \phi_G - \chi \quad (2)$$

for n-type semiconductor where ϕ_G is the work function of graphene and χ is the electron affinity of semiconductor.

Under illumination, the photoexcited electrons and holes are generated in the GaAs substrate and then separated by the built-in electric field at the Schottky junction. Electrons and holes are collected by bottom electrodes and graphene film which form a photovoltaic action for n-type GaAs as shown in Figure 2.

TABLE 1: Simulation parameters for graphene GaAs solar cell.

Parameter	Description	Value
E_g	GaAs band gap	1.42 ev
N_c	Effective density of states in CB	$4.35e \times 10^{17} \text{ cm}^{-3}$
N_v	Effective density of states in VB	$8.16e \times 10^{18} \text{ cm}^{-3}$
χ	GaAs electron affinity	4.07 ev
μ_e	GaAs electron mobility, 300 K [23]	No doping: $8000 \text{ cm}^2/\text{Vs}$ N-type doping $1 \times 10^{14} \text{ cm}^{-3}$: $7300 \text{ cm}^2/\text{Vs}$ N-type doping $1 \times 10^{15} \text{ cm}^{-3}$: $5900 \text{ cm}^2/\text{Vs}$ N-type doping $1 \times 10^{16} \text{ cm}^{-3}$: $4600 \text{ cm}^2/\text{Vs}$
μ_h	GaAs hole mobility, 300 K	No doping: $400 \text{ cm}^2/\text{Vs}$ N-type doping $1 \times 10^{14} \text{ cm}^{-3}$: $340 \text{ cm}^2/\text{Vs}$ N-type doping $1 \times 10^{15} \text{ cm}^{-3}$: $302 \text{ cm}^2/\text{Vs}$ N-type doping $1 \times 10^{16} \text{ cm}^{-3}$: $240 \text{ cm}^2/\text{Vs}$

TABLE 2: Efficiency versus GaAs thickness, graphene work function and transmittance, and n-type doping concentration under AM1.5 illumination.

GaAs thickness (μm)	Graphene work function (ev)	Graphene transmittance (%)	N-type doping (cm^{-3})	J_{sc} (mA/cm^2)	V_{oc} (V)	FF	η (%)
1	4.55	93.1	No doping	7.082	0.255	0.344	0.772
2	4.55	93.1	No doping	8.483	0.268	0.406	1.174
5	4.55	93.1	No doping	8.261	0.281	0.473	1.392
10	4.55	93.1	No doping	7.519	0.289	0.433	1.196
5	4.4	95.4	No doping	8.613	0.263	0.451	1.298
5	4.8	85.3	No doping	7.951	0.296	0.496	1.481
5	4.8	85.3	$1e14$	7.966	0.301	0.499	1.518
5	4.8	85.3	$1e15$	8.054	0.332	0.518	1.755
5	4.8	85.3	$1e16$	8.191	0.389	0.548	2.218

To investigate the performance of graphene based solar cell, simulations were carried out using TCAD, which divides into two steps since there is no graphene default involved in the material declaration. Firstly, we deposit 10 nm aluminum film as anode electrode instead of graphene film using ATHENA tool to generate the device structure. Secondly, we redefine the anode electrode material as graphene layer using ATLAS tool.

Graphene is modeled as a semimetal, a carrier mobility of $15,000 \text{ cm}^2/\text{Vs}$. The carrier densities were calculated by Fermi distribution and by adjusting the values of effective masses, a thickness of 10 nm, and band gap such that the carrier densities agree with experimental results. It is important to point out that, for multilayer graphene film, the E - K dispersion relationship is weakly parabolic rather than linear as in the case of monolayer graphene. Simulation parameters used in Atlas tool for this device are listed in Table 1.

3. Result and Discussion

3.1. GaAs Substrate Thickness Effect. GaAs crystal is chosen as absorption area. Graphene layer acts as a transparent electrode, that is, for the intensity of photogenerated carriers. A Schottky junction is built in for the difference between their

work functions. Figures 3(a)–3(d) show the photogeneration rates of GaAs solar cell under AM1.5 illumination with depth for absorption layer were maintained at $1 \mu\text{m}$, $2 \mu\text{m}$, $5 \mu\text{m}$, and $10 \mu\text{m}$, respectively. The light could be absorbed in barrier layer and inside the semiconductor. Both results show the most effective absorption area located in the surface attachment about $0.1 \mu\text{m}$. Meanwhile, Figure 3(d) shows that $10 \mu\text{m}$ thickness is enough for full spectrum absorption since the intensity of the photogenerated carriers dramatically reduces in the deep area of GaAs substrate.

To investigate the effect of GaAs thickness on the performance of solar cell, we calculate the current-voltage curves and internal quantum efficiency (IQE) shown in Figures 4 and 5, respectively. Most carriers are generated around the surface for GaAs under light illumination. At the condition of the thickness below $5 \mu\text{m}$, the absorption of long wavelength photo is strengthened with the increase of thickness. In comparison the absorption of long wavelength photo decreases when the thickness at $5 \mu\text{m}$ and $10 \mu\text{m}$ expects the absorption peak at 870 nm which is according to the band energy level of GaAs. As a result, the light current gets a peak value versus different substrate thickness which leads to the biggest power conversion efficiency at 1.392% (listed in Table 2).

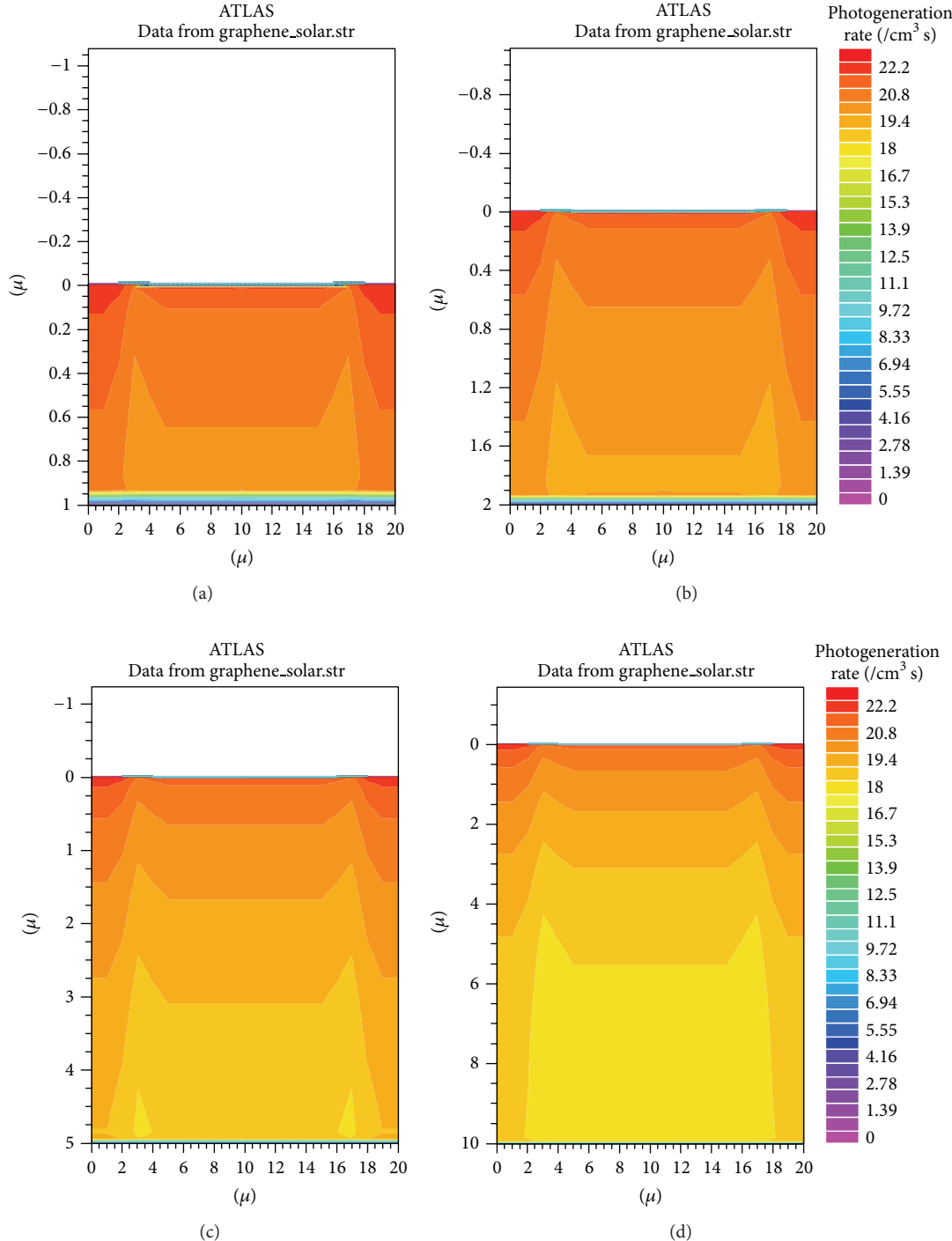


FIGURE 3: Photogeneration rate of graphene GaAs solar cell under AM1.5 illumination versus substrate thickness: (a) $1\text{ }\mu\text{m}$, (b) $2\text{ }\mu\text{m}$, (c) $5\text{ }\mu\text{m}$, and (d) $10\text{ }\mu\text{m}$.

3.2. Graphene Work Function and Transmittance Effect. According to the theory model described in Figure 2, the battier height ϕ_B is related to the difference between graphene work function ϕ_G and electron affinity χ of GaAs. Consequently, higher work function increases ϕ_B and further enhances the built-in potential V_{bi} via the equation $V_{bi} = \phi_B - V_n$, where V_n means the distance between E_c and E_f in GaAs.

Therefore, the increase of graphene work function implies the increase of V_{bi} corresponding to the upper limitation of V_{oc} .

Lancellotti et al. reported the dependence of graphene work function and transmittance on the number of layers [21]. We calculated the current-voltage curves and IQE of graphene GaAs solar cells versus different graphene work function considering the dependence of transmittance.

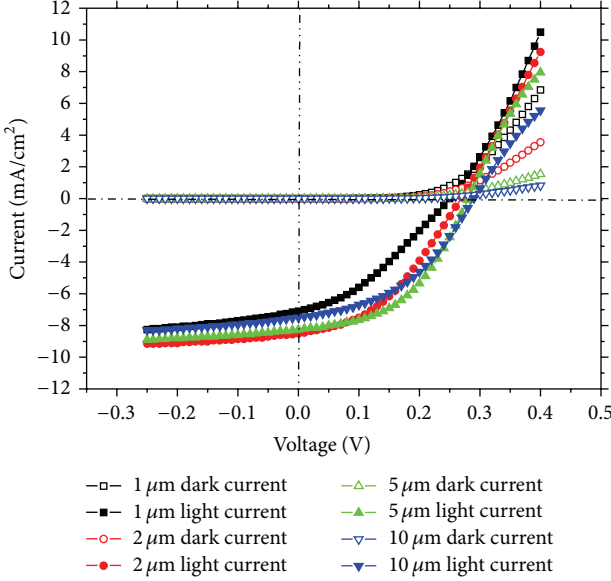


FIGURE 4: Current-voltage curves of graphene solar cells versus different GaAs thickness.

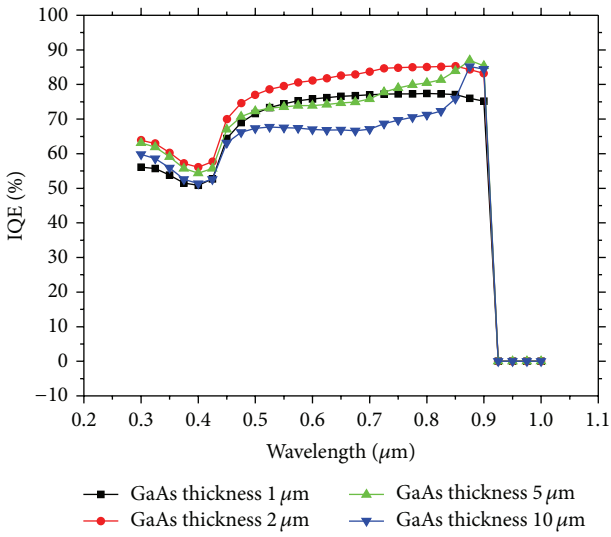


FIGURE 5: IQE of graphene solar cells versus different GaAs thickness.

We noticed that the IQE of three kinds of graphene layer have almost the same absorption spectrum zone as shown in Figure 7. However, the higher transmittance means the lower work function which leads to the balance between short circuit current and open-circuit voltage as shown in Figure 6. Accordingly, higher barrier also leads to a bigger fill factor. As a result, we got the biggest power conversion efficiency at 1.481% (listed in Table 2).

3.3. N-Type Doping Effect. It is well known that the n-type doping in GaAs can increase the Fermi energy level and intensity of photogeneration carriers. For doping concentration at $1 \times 10^{14} \text{ cm}^{-3}$, $1 \times 10^{15} \text{ cm}^{-3}$, and $1 \times 10^{16} \text{ cm}^{-3}$,

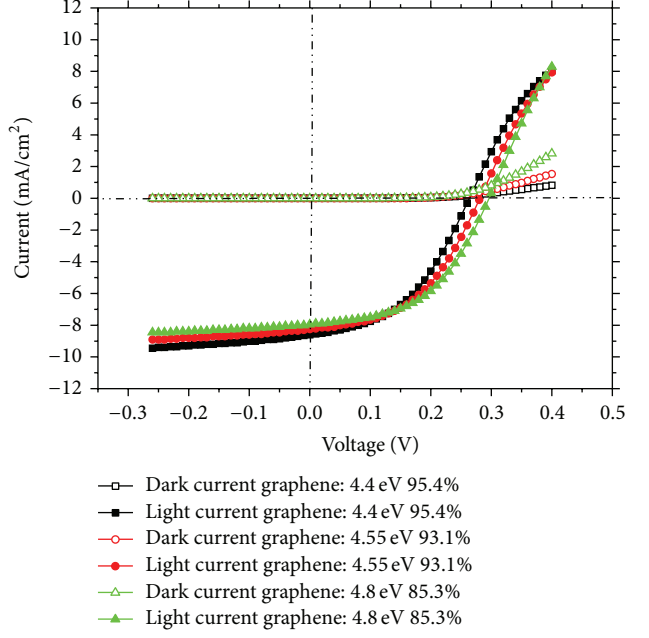


FIGURE 6: Current-voltage curves of graphene solar cells versus different graphene work function.

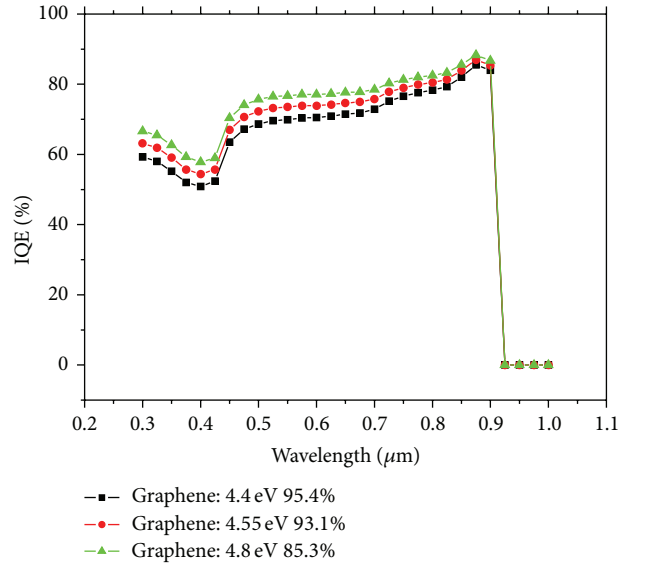


FIGURE 7: IQE of graphene solar cells versus different graphene work function.

the short-circuit current and open-circuit voltage are both increased due to higher barrier height as shown in Figure 8. The variation of V_{oc} is much more significant than that of I_{sc} which has great consistency with the IQE results shown in Figure 9. In other words, n-type doping for GaAs mainly affects the height of barrier which leads to the enhancement of open-circuit voltage while the current generated by photos does not show great shifts. It may be due to the movement of depletion boundary in the region close to the interface of graphene and GaAs with increasing doping density.

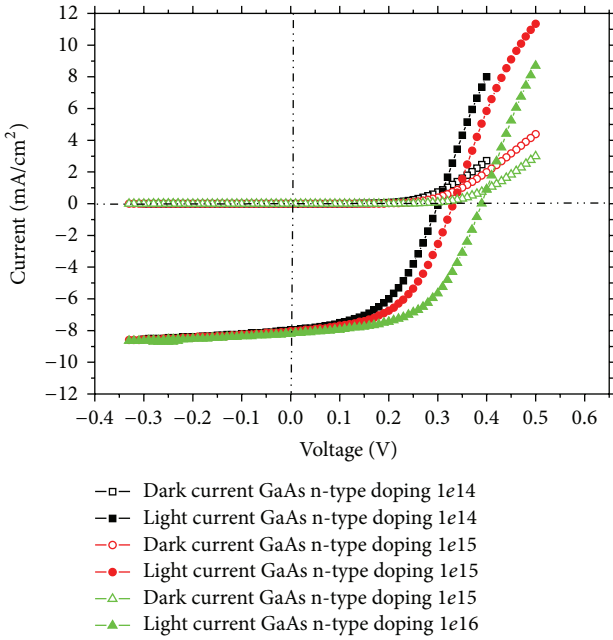


FIGURE 8: Current-voltage curves of graphene GaAs solar cells versus n-type doping concentration.

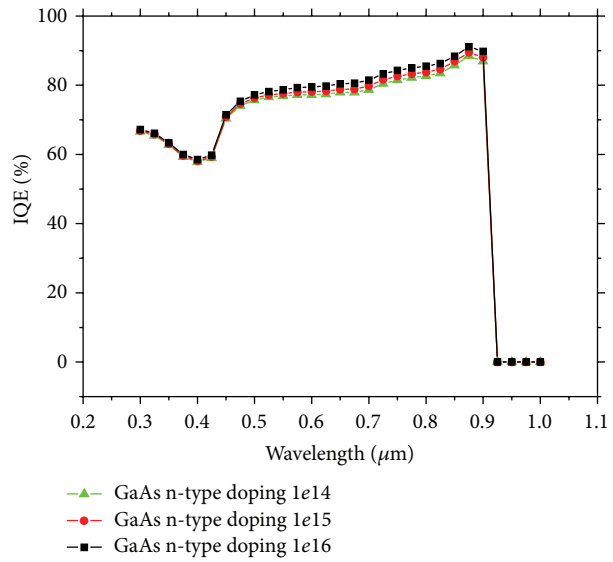


FIGURE 9: IQE of graphene GaAs solar cells versus n-type doping concentration.

4. Conclusion

Graphene based GaAs solar cell is modeled and then two-dimensional simulation of this device is carried out using Silvaco TCAD tools. The process of structure generation and material definition is described in the front section. We further compared the performance at different conditions including GaAs thickness, graphene work function and transmittance, and n-type doping concentration in GaAs crystal in detail. The results show that most carriers generated in the region locate very close to the interface under light

illumination. The comparison between higher work function and lower transmittance of graphene shows that the work function is more efficient for better performance. Moderate n-type doping in GaAs leads to great increase of power conversion efficiency while open-circuit voltage is much more sensitive than short-circuit current of this kind of device.

Conflict of Interests

The authors declare that there is no conflict of interests regarding the publication of this paper.

Acknowledgment

This work was supported by the National Natural Science Foundation of China (11247028).

References

- [1] P. Avouris and M. Freitag, "Graphene photonics, plasmonics, and optoelectronics," *IEEE Journal on Selected Topics in Quantum Electronics*, vol. 20, no. 1, Article ID 6000112, 2014.
- [2] D. Chen, H. Zhang, Y. Liu, and J. Li, "Graphene and its derivatives for the development of solar cells, photoelectrochemical, and photocatalytic applications," *Energy and Environmental Science*, vol. 6, no. 5, pp. 1362–1387, 2013.
- [3] P. Gao, K. Ding, Y. Wang et al., "Crystalline Si/graphene quantum dots heterojunction solar cells," *The Journal of Physical Chemistry C*, vol. 118, no. 10, pp. 5164–5171, 2014.
- [4] Z. Zhang, T. Cui, R. Lv et al., "Improved efficiency of Graphene/Si heterojunction solar cells by optimizing hydrocarbon feed rate," *Journal of Nanomaterials*, vol. 2014, Article ID 359305, 7 pages, 2014.
- [5] X. Miao, S. Tongay, M. K. Petterson et al., "High efficiency graphene solar cells by chemical doping," *Nano Letters*, vol. 12, no. 6, pp. 2745–2750, 2012.
- [6] Y. Lei, R. Li, F. Chen, and J. Xu, "Hydrothermal synthesis of graphene-CdS composites with improved photoelectric characteristics," *Journal of Materials Science: Materials in Electronics*, vol. 25, no. 7, pp. 3057–3061, 2014.
- [7] L.-B. Luo, J.-J. Chen, M.-Z. Wang et al., "Near-infrared light photovoltaic detector based on GaAs nanocone array/monolayer graphene schottky junction," *Advanced Functional Materials*, vol. 24, no. 19, pp. 2794–2800, 2014.
- [8] J. Miao, W. Hu, N. Guo et al., "High responsivity graphene/InAs nanowire heterojunction near-infrared photodetectors with distinct photocurrent on/off ratio," *Small*, 2014.
- [9] Z. Liu, T. Luo, B. Liang et al., "High-detectivity InAs nanowire photodetectors with spectral response from ultraviolet to near-infrared," *Nano Research*, vol. 6, no. 11, pp. 775–783, 2013.
- [10] Z. Liu, J. Xu, D. Chen, and G. Shen, "Flexible electronics based on inorganic nanowires," *Chemical Society Reviews*, vol. 44, no. 1, pp. 161–192, 2015.
- [11] N. Guo, W. Hu, L. Liao et al., "Anomalous and highly efficient InAs nanowire phototransistors based on majority carrier transport at room temperature," *Advanced Materials*, vol. 26, no. 48, pp. 8203–8209, 2014.
- [12] J. Miao, W. Hu, N. Guo et al., "Single InAs nanowire room-temperature near-infrared photodetectors," *ACS Nano*, vol. 8, no. 4, pp. 3628–3635, 2014.

- [13] X. Li, H. Zhu, K. Wang et al., "Graphene-on-silicon schottky junction solar cells," *Advanced Materials*, vol. 22, no. 25, pp. 2743–2748, 2010.
- [14] X. Zhang, C. Xie, J. Jie, X. Zhang, Y. Wu, and W. Zhang, "High-efficiency graphene/Si nanoarray Schottky junction solar cells via surface modification and graphene doping," *Journal of Materials Chemistry A*, vol. 1, no. 22, pp. 6593–6601, 2013.
- [15] T. Feng, D. Xie, Y. Lin et al., "Graphene based Schottky junction solar cells on patterned silicon-pillar-array substrate," *Applied Physics Letters*, vol. 99, no. 23, Article ID 233505, 2011.
- [16] C. Xie, J. Jie, B. Nie et al., "Schottky solar cells based on graphene nanoribbon/multiple silicon nanowires junctions," *Applied Physics Letters*, vol. 100, no. 19, Article ID 193103, 2012.
- [17] A. V. Babichev, V. E. Gasumyants, A. Y. Egorov, S. Vitusevich, and M. Tchernycheva, "Contact properties to CVD-graphene on GaAs substrates for optoelectronic applications," *Nanotechnology*, vol. 25, no. 33, Article ID 335707, 2014.
- [18] K. Takehana, Y. Imanaka, T. Takamasu, Y. Kim, and K.-S. An, "Substrate dependence of cyclotron resonance on large-area CVD graphene," *Current Applied Physics*, vol. 14, no. 1, pp. S119–S122, 2014.
- [19] W. Jie, F. Zheng, and J. Hao, "Graphene gallium arsenide-based Schottky junction solar cells," *Applied Physics Letters*, vol. 103, no. 23, Article ID 233111, 2013.
- [20] S. K. Behura, P. Mahala, A. Ray, I. Mukhopadhyay, and O. Jani, "Theoretical simulation of photovoltaic response of graphene-on-semiconductors," *Applied Physics A*, vol. 111, no. 4, pp. 1159–1163, 2013.
- [21] L. Lancellotti, T. Polichetti, F. Ricciardella et al., "Graphene applications in Schottky barrier solar cells," *Thin Solid Films*, vol. 522, pp. 390–394, 2012.
- [22] Z. Arefinia and A. Asgari, "A new modeling approach for graphene based silicon nanowire Schottky junction solar cells," *Journal of Renewable and Sustainable Energy*, vol. 6, no. 4, Article ID 043132, 2014.
- [23] *Silvaco-Atlas User's Manual*, 2014.

Research Article

Shell Thickness-Dependent Strain Distributions of Confined Au/Ag and Ag/Au Core-Shell Nanoparticles

Feng Liu,¹ Honghua Huang,² Ying Zhang,² Ting Yu,² Cailei Yuan,² and Shuangli Ye^{1,3}

¹*Institute of Microelectronics and Information Technology, Wuhan University, Wuhan, Hubei 430072, China*

²*Laboratory of Nanomaterials and Sensors, School of Physics, Electronics and Communication, Jiangxi Normal University, Nanchang, Jiangxi 330022, China*

³*School of Printing and Packaging, Wuhan University, Wuhan, Hubei 430072, China*

Correspondence should be addressed to Shuangli Ye; slye@whu.edu.cn

Received 27 November 2014; Accepted 31 December 2014

Academic Editor: Wen Lei

Copyright © 2015 Feng Liu et al. This is an open access article distributed under the Creative Commons Attribution License, which permits unrestricted use, distribution, and reproduction in any medium, provided the original work is properly cited.

The shell thickness-dependent strain distributions of the Au/Ag and Ag/Au core-shell nanoparticles embedded in Al_2O_3 matrix have been investigated by finite element method (FEM) calculations, respectively. The simulation results clearly indicate that there is a substantial strain applied on both the Au/Ag and Ag/Au core-shell nanoparticles by the Al_2O_3 matrix. For the Au/Ag nanoparticles, it can be found that the compressive strain existing in the shell is stronger than that on the center of core and reaches the maximum at the interface between the shell and core. In contrast, for the Ag/Au nanoparticles, the compressive strain applied on the core is much stronger than that at the interface and that in the shell. With the shell thickness increasing, both of the strains in the Au/Ag and Ag/Au nanoparticles increase as well. However, the strain gradient in the shell decreases gradually with the increasing of the shell thickness for both of Ag/Au ad Au/Ag nanoparticles. These results provide an effective method to manipulate the strain distributions of the Au/Ag and Ag/Au nanoparticles by tuning the thickness of the shell, which can further have significant influences on the microstructures and physical properties of Au/Ag and Ag/Au nanoparticles.

1. Introduction

Nanoparticles with core-shell structure have attracted intensive scientific and technical interests due to their potential applications in catalysis, drug delivery, microelectronics, sensor, and many other emerging nanotechnologies [1–5]. Particularly, the bimetallic nanoparticles with core-shell structure have constantly been the subject of these studies because of their improved electronic, optical, and catalytic performances compared with those of monometallic nanoparticles [6, 7]. Moreover, it has been demonstrated that the composition, size, shape, and surface modification of these bimetallic nanoparticles can be tailored for the targeted applications [8, 9]. Among them, Au/Ag and Ag/Au core-shell nanoparticles have currently captured exponential attention due to their unique optical and photonic properties. It has been illustrated that Au and Ag present a broad absorption band in the visible

region of the electromagnetic spectrum [10–12], which can be due to the collective oscillation of the free conduction electrons induced by an interacting electromagnetic field [13]. Moreover, Au is a suitable candidate for biomedical applications because of its excellent performances on biocompatibility, chemical stability and easy surface modification, and so forth. Therefore, the Au/Ag and Ag/Au core-shell nanoparticles with surface plasmon enhancement and high levels of sensitivity have tremendous applications for optical, chemical, and bimolecular devices. For example, the generation of detectable Fano-resonance has been demonstrated in Au/Ag core-shell structure [14], which has a great potential in the subwavelength waveguides, and low-loss metamaterials sensors [15–18].

On the other hand, strain engineering provides a general strategy to control the morphology and microstructure of the nanostructures, leading to an enhancement of their device

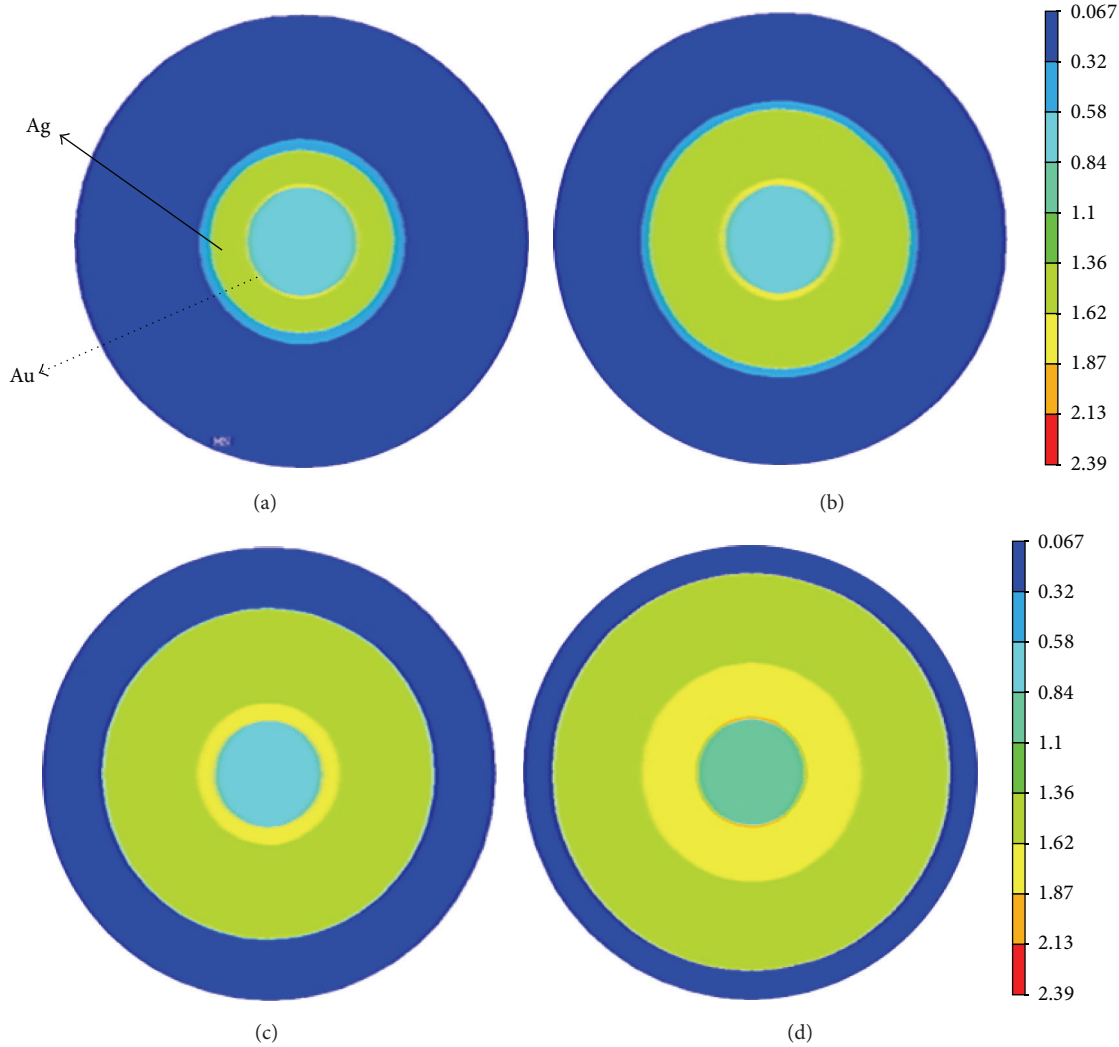


FIGURE 1: Morphological cross-sectional strain distribution of embedded core-shell Au/Ag nanoparticles with the shell thickness of (a) 2.5 nm, (b) 5 nm, (c) 7.5 nm, and (d) 10 nm, respectively.

performance. For example, quantum dots, a kind of nanostructures for making high performance nanodevices, can be realized by using self-assembled growth technique, which is based on a process of strain accumulation and relaxation in the system [19, 20]. For the core-shell nanoparticles confined in a host matrix, a substantial strain is induced [21–25], which can be used to tune the interplay between the core and shell layers, the morphology [26, 27], and optical properties [28]. Therefore, for the Au/Ag and Ag/Au core-shell nanoparticles, along with the enhanced light absorption, spectral tuning of the surface plasmon resonance by strain can provide another dimension besides the usual size and composition manipulation. Here, the shell thickness-dependent strain distributions of the Au/Ag and Ag/Au core-shell nanoparticles embedded in Al_2O_3 matrix have been investigated, respectively. The simulation results offer an effective method to manipulate the strain distributions of the Au/Ag and Ag/Au nanoparticles by tuning the thickness of the shell, which can further have significant influences on the surface states and surface plasmon resonance of Au/Ag and Ag/Au nanoparticles.

2. Methods

In this paper, a FE calculation is performed to simulate the strain distribution of embedded Au/Ag and Ag/Au core/shell nanoparticles with different shell thickness. The interplay between the strain and the structure of confined Au/Ag and Ag/Au nanoparticles has been investigated. FE calculation has been applied successfully to continuum modeling of deformation [29] of materials. Recently, simulation on the strain distribution of nanoparticles by FE method has been widely studied [30, 31]. For materials at nanoscale, the simulations by the continuum elastic FE method and the atomistic strain calculations have reached a general qualitative agreement [32, 33]. Many physical properties of nanomaterials, including elastic anisotropy, thermal expansion, and three-dimensional morphology, can be understood well by the FE simulation results. In our simulation, the FE model for the strain distribution is based upon the following assumptions. A spherical, linear-elastic core-shell Au/Ag or Ag/Au nanoparticle is confined in an isotropic and linear-elastic

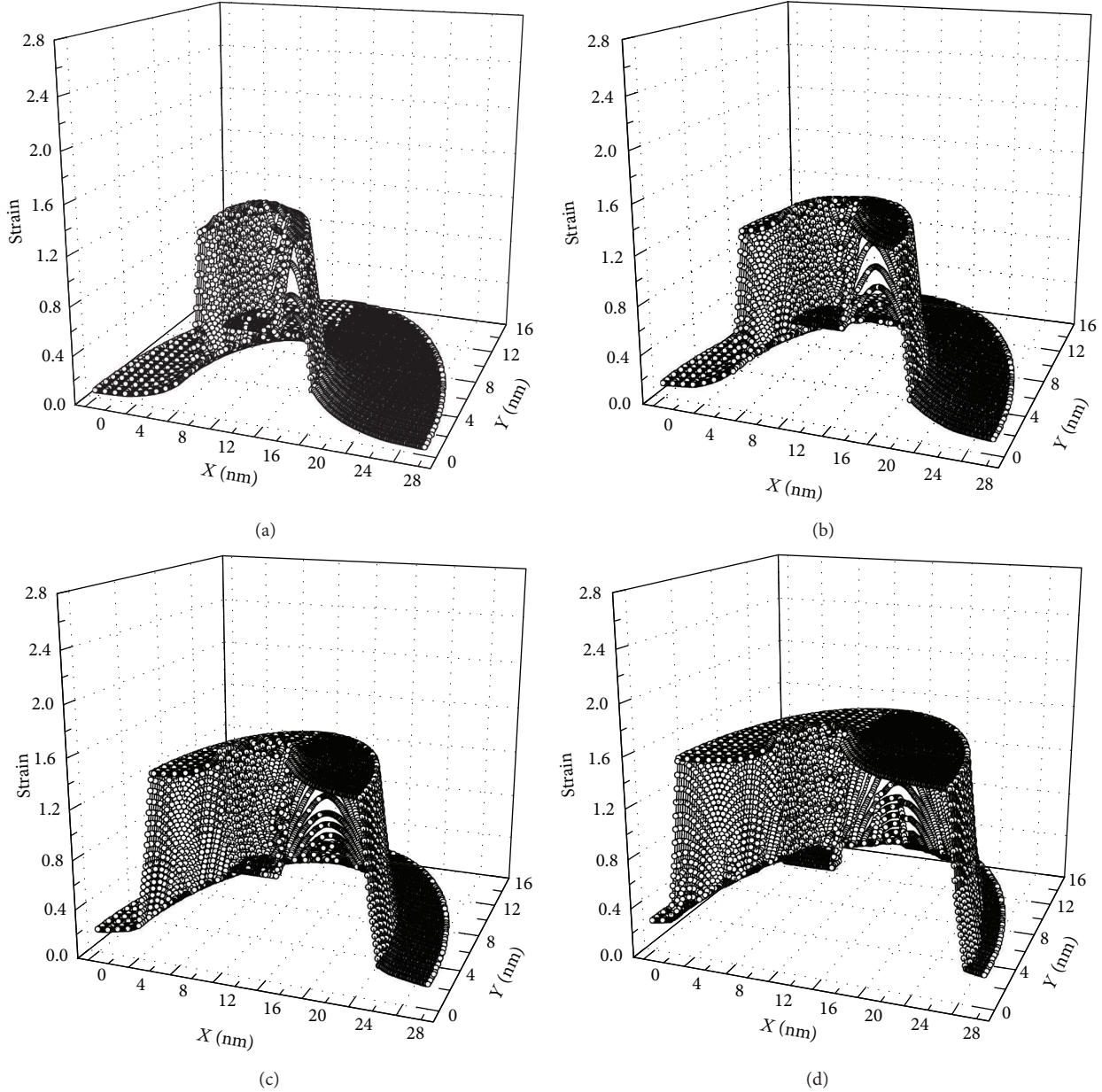


FIGURE 2: X-Y plane strain profiles for Au/Ag nanoparticles with the shell thickness of (a) 2.5 nm, (b) 5 nm, (c) 7.5 nm, and (d) 10 nm, respectively.

matrix. The Au/Ag or Ag/Au nanoparticle surface is welded to the Al_2O_3 matrix. The core size is 2.5 nm and the shell thickness is 2.5 nm, 5 nm, 7.5 nm, and 10 nm for each nanoparticle, respectively. The thermal expansion mismatch between the nanoparticles and Al_2O_3 matrix leads to a substantial strain in the confined Au/Ag or Ag/Au nanoparticles. Young's modulus is taken to be 170 GPa, 76 GPa, and 360 GPa for Au, Ag, and Al_2O_3 , while Poisson's ratio is taken to be 0.42, 0.38, and 0.24 for Au, Ag, and Al_2O_3 , respectively.

3. Results and Discussion

The morphological cross-sectional strain distributions for the core-shell Au/Ag nanoparticles embedded in Al_2O_3 thin film

with the shell thickness of 2.5 nm, 5 nm, 7.5 nm, and 10 nm are presented in Figures 1(a)–1(d), respectively. It can be found that the strain distributes inhomogeneously, which can be tuned by the shell thickness. Correspondingly, the X-Y plane strain profiles for embedded Au/Ag nanoparticle with the shell thickness of 2.5 nm, 5 nm, 7.5 nm, and 10 nm are shown in Figures 2(a)–2(d), respectively. Figures 2(a)–2(d) illustrate quantitatively that there is a large compressive strain applied on the Au/Ag nanoparticle by the Al_2O_3 matrix. The strain is weaker in the core than that in the shell. It reaches the maximum at the interface and decreases with the layer away from the interface. With the shell thickness increasing, it can be seen that the strain existing in the core-shell Au/Ag nanoparticles becomes stronger. The strain distribution in

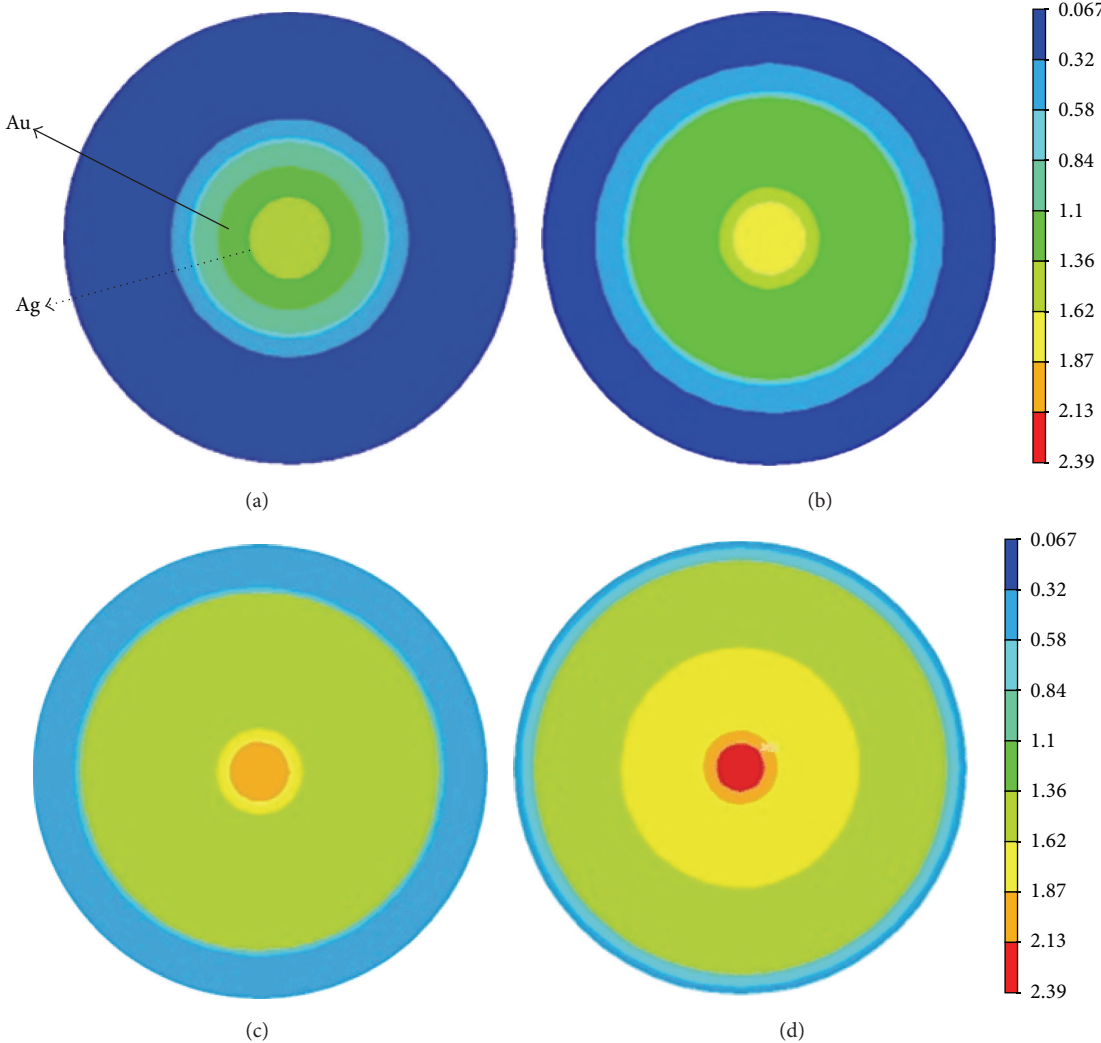


FIGURE 3: Morphological cross-sectional strain distribution of confined Ag/Au nanoparticles with the shell thickness of (a) 2.5 nm, (b) 5 nm, (c) 7.5 nm, and (d) 10 nm, respectively.

the core keeps homogenous. However, the inhomogeneity of strain distribution existing in the shell is enhanced.

Similarly, the morphological cross-sectional strain distributions for Ag/Au nanoparticles embedded in Al_2O_3 thin films with the shell thickness of 2.5 nm, 5 nm, 7.5 nm, and 10 nm are presented in Figures 3(a)–3(d), respectively. The X-Y plane strain profiles for embedded Ag/Au nanoparticle with the shell thickness of 2.5 nm, 5 nm, 7.5 nm, and 10 nm are illustrated in Figures 4(a)–4(d), respectively. It also can be seen that there is a compressive strain applied on the Ag/Au nanoparticles by the Al_2O_3 matrix. However, the strain distributes quite differently from that in the Au/Ag nanoparticle, which reaches the maximum in the core and decreases monotonously from the core to the shell in the Ag/Au nanoparticles. With the shell thickness increasing, the strain increases as well. The strain distribution in the core keeps homogenous, and the inhomogeneity of strain distribution existing in the shell is enhanced.

For a comparison, Figure 5 illustrates the strain distributions and the strain gradient for the Au/Ag and Ag/Au nanoparticles with the shell thickness of 2.5 nm, 5 nm, 7.5 nm, and 10 nm, respectively. It can be found that, for both of Au/Ag and Ag/Au nanoparticles, the strain is enhanced with the increasing of the shell thickness. Moreover, the strain increases faster for Ag/Au than that for Au/Ag nanoparticles. For these two core-shell nanoparticles with the same shell thickness, the strain on the core is larger for Ag/Au than that for Au/Ag nanoparticles, which can be due to the larger Young's modulus of Au than that of Ag. The strain gradient in the shell decreases gradually with the increasing of the shell thickness for both of Ag/Au ad Au/Ag nanoparticles. However, the strain gradient in the shell decreases faster for Au/Ag than that for Ag/Au nanoparticles. The homogeneous strain distribution in the core and the inhomogeneous strain in the shell can have a significant influence on the microstructure and morphology of Au/Ag and Ag/Au nanoparticles, which

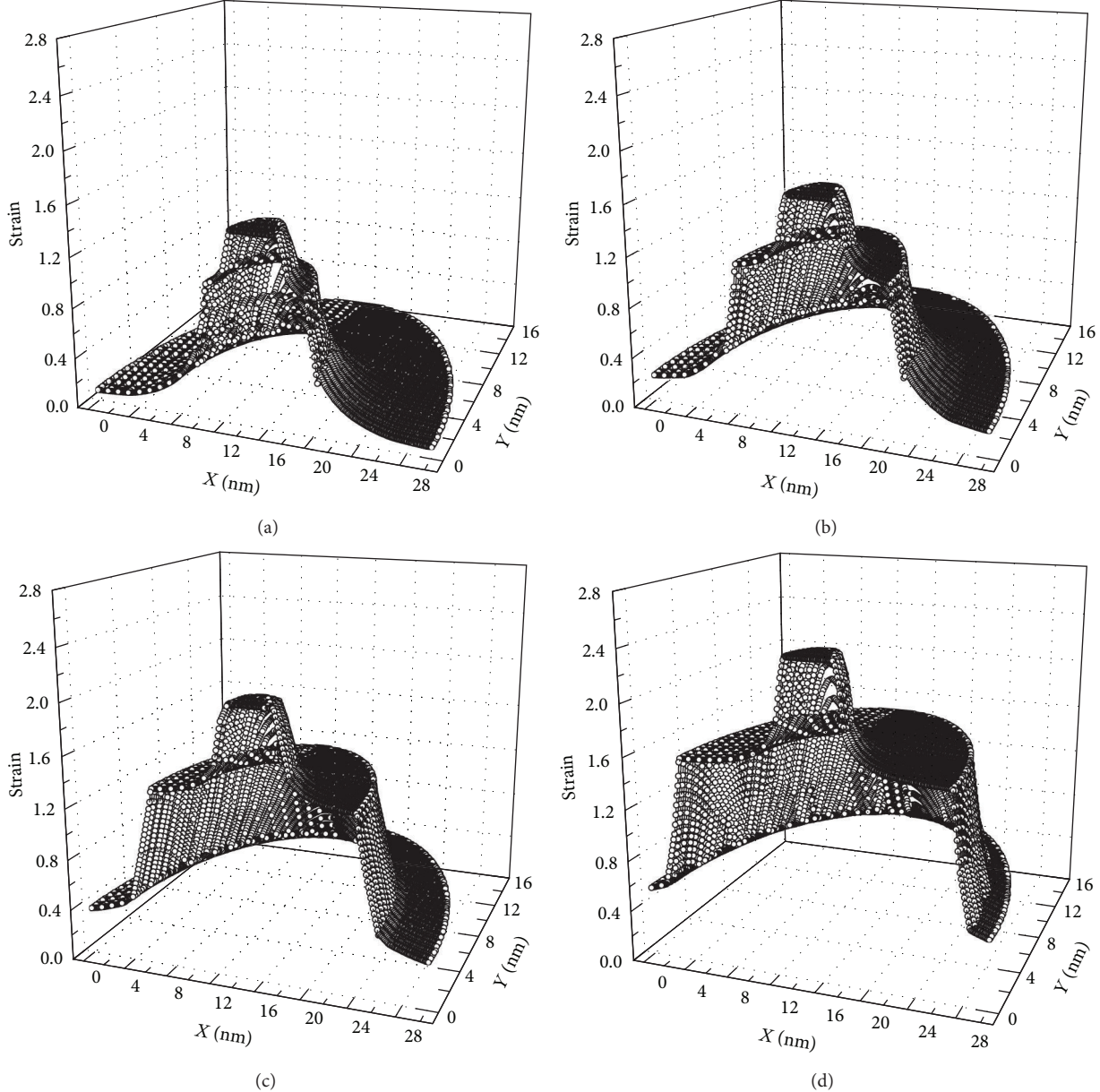


FIGURE 4: X-Y plane strain profiles of Ag/Au nanoparticles with the shell thickness of (a) 2.5 nm, (b) 5 nm, (c) 7.5 nm, and (d) 10 nm, respectively.

plays an important role in tuning the surface states and surface plasmon resonance of Au/Ag and Ag/Au nanoparticles.

4. Conclusion

In summary, the shell thickness-dependent strain distributions of the Au/Ag and Ag/Au core-shell nanoparticles embedded in Al_2O_3 matrix have been investigated by FEM calculations, respectively. The simulation results clearly indicate that there is a substantial strain applied on both the Au/Ag and Ag/Au core-shell nanoparticles by the Al_2O_3 matrix, and the strain distributes homogeneously in the core and

inhomogeneously in the shell. For the Au/Ag nanoparticle, the strain reaches the maximum at the interface and is weaker in the core than that in the shell. For the Ag/Au nanoparticles, the strain decreases monotonously from the core to the shell. For these two nanoparticles with the same shell thickness, the strain in the core is larger for Ag/Au than that for Au/Ag nanoparticles. With the shell thickness increasing, both of the strains in Au/Ag and Ag/Au nanoparticles are enhanced, and the strain gradient in the shell decreases gradually. These results demonstrate an effective method to manipulate the strain distributions of the Au/Ag and Ag/Au nanoparticles by tuning the thickness of the shell, which plays an important role in optical properties of Au/Ag and Ag/Au nanoparticles.

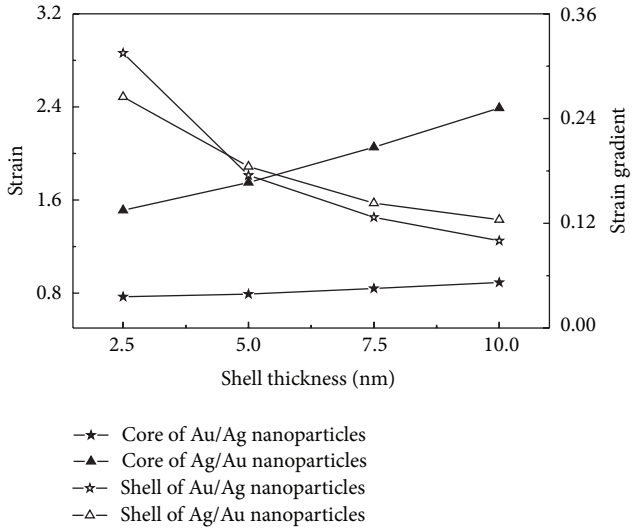


FIGURE 5: Strain on the core, strain gradient in the shell of the Au/Ag and Ag/Au nanoparticles with the shell thickness of 2.5 nm, 5 nm, 7.5 nm, and 10 nm, respectively.

Conflict of Interests

The authors declare that there is no conflict of interests regarding the publication of this paper.

Acknowledgment

This work is supported by National Natural Science Foundation of China (Grant nos. 11164008, 51461019, 11174226, and 51371129).

References

- [1] B. Wiley, Y. Sun, and Y. Xia, "Synthesis of silver nanostructures with controlled shapes and properties," *Accounts of Chemical Research*, vol. 40, no. 10, pp. 1067–1076, 2007.
- [2] L. Lu, A. Kobayashi, K. Tawa, and Y. Ozaki, "Silver nanoplates with special shapes: controlled synthesis and their surface plasmon resonance and surface-enhanced Raman scattering properties," *Chemistry of Materials*, vol. 18, no. 20, pp. 4894–4901, 2006.
- [3] Y.-S. Shon and E. Cutler, "Aqueous synthesis of alkanethiolate-protected Ag nanoparticles using bunte salts," *Langmuir*, vol. 20, no. 16, pp. 6626–6630, 2004.
- [4] Z. S. Pillai and P. V. Kamat, "What factors control the size and shape of silver nanoparticles in the citrate ion reduction method?" *The Journal of Physical Chemistry B*, vol. 108, no. 3, pp. 945–951, 2004.
- [5] J. H. Hodak, A. Henglein, M. Giersig, and G. V. Hartland, "Laser-induced inter-diffusion in AuAg core–shell nanoparticles," *The Journal of Physical Chemistry B*, vol. 104, no. 49, pp. 11708–11718, 2000.
- [6] I. Srnová-Šloufová, F. Lednický, A. Gemperle, and J. Gemperlová, "Core-shell (Ag)Au bimetallic nanoparticles: analysis of transmission electron microscopy images," *Langmuir*, vol. 16, no. 25, pp. 9928–9935, 2000.
- [7] C. C. Li, L. Sun, Y. Q. Sun, and T. Teranishi, "One-pot controllable synthesis of au@ag heterogeneous nanorods with highly tunable plasmonic absorption," *Chemistry of Materials*, vol. 25, no. 13, pp. 2580–2590, 2013.
- [8] L. H. Lu, G. Y. Sun, H. J. Zhang et al., "Fabrication of core-shell Au-Pt nanoparticle film and its potential application as catalysis and SERS substrate," *Journal of Materials Chemistry*, vol. 14, no. 6, pp. 1005–1009, 2004.
- [9] F. Hubenthal, N. Borg, and F. Träger, "Optical properties and ultrafast electron dynamics in gold-silver alloy and core-shell nanoparticles," *Applied Physics B: Lasers and Optics*, vol. 93, no. 1, pp. 39–45, 2008.
- [10] J. Schmitt, P. Mächtle, D. Eck, H. Möhwald, and C. A. Helm, "Preparation and optical properties of colloidal gold monolayers," *Langmuir*, vol. 15, no. 9, pp. 3256–3266, 1999.
- [11] U. Kreibig and M. Vollmer, *Optical Properties of Metal Clusters*, Springer, Berlin, Germany, 1995.
- [12] P. Mulvaney, "Surface plasmon spectroscopy of nanosized metal particles," *Langmuir*, vol. 12, no. 3, pp. 788–800, 1996.
- [13] A. K. Samal, L. Polavarapu, S. Rodal-Cedeira, L. M. Liz-Marzán, J. Pérez-Juste, and I. Pastoriza-Santos, "Size tunable Au@Ag core-shell nanoparticles: synthesis and surface-enhanced raman scattering properties," *Langmuir*, vol. 29, no. 48, pp. 15076–15082, 2013.
- [14] O. Peña-Rodríguez and U. Pal, "Au@Ag core-shell nanoparticles: efficient all-plasmonic Fano-resonance generators," *Nanoscale*, vol. 3, no. 9, pp. 3609–3612, 2011.
- [15] J. B. Lassiter, H. Sobhani, J. A. Fan et al., "Fano resonances in plasmonic nanoclusters: geometrical and chemical tunability," *Nano Letters*, vol. 10, no. 8, pp. 3184–3189, 2010.
- [16] J. A. Fan, C. Wu, K. Bao et al., "Self-assembled plasmonic nanoparticle clusters," *Science*, vol. 328, no. 5982, pp. 1135–1138, 2010.
- [17] N. Liu, T. Weiss, M. Mesch et al., "Planar metamaterial analogue of electromagnetically induced transparency for plasmonic sensing," *Nano Letters*, vol. 10, no. 4, pp. 1103–1107, 2010.
- [18] S. Mukherjee, H. Sobhani, J. B. Lassiter, R. Bardhan, P. Nordlander, and N. J. Halas, "Fanoshells: nanoparticles with built-in Fano resonances," *Nano Letters*, vol. 10, no. 7, pp. 2694–2701, 2010.
- [19] D. Gammon, "Quantum dots: strain is a problem no more," *Nature Nanotechnology*, vol. 7, no. 10, pp. 621–622, 2012.
- [20] P. J. Simmonds, C. D. Yerino, M. Sun et al., "Tuning quantum dot luminescence below the bulk band gap using tensile strain," *ACS Nano*, vol. 7, no. 6, pp. 5017–5023, 2013.
- [21] A. Wellner, V. Paillard, C. Bonafos et al., "Stress measurements of germanium nanocrystals embedded in silicon oxide," *Journal of Applied Physics*, vol. 94, no. 9, pp. 5639–5642, 2003.
- [22] A. Cheung, G. de M. Azevedo, C. J. Glover et al., "Structural perturbations within Ge nanocrystals in silica," *Applied Physics Letters*, vol. 84, no. 2, article 278, 2004.
- [23] H. G. Chew, F. Zheng, W. K. Choi, W. K. Chim, Y. L. Foo, and E. A. Fitzgerald, "Influence of reductant and germanium concentration on the growth and stress development of germanium nanocrystals in silicon oxide matrix," *Nanotechnology*, vol. 18, no. 6, Article ID 065302, 2007.
- [24] T. Benabbas, Y. Androussi, and A. Lefebvre, "A finite-element study of strain fields in vertically aligned InAs islands in GaAs," *Journal of Applied Physics*, vol. 86, no. 4, pp. 1945–1950, 1999.
- [25] Q. X. Pei, C. Lu, and Y. Y. Wang, "Effect of elastic anisotropy on the elastic fields and vertical alignment of quantum dots," *Journal of Applied Physics*, vol. 93, no. 3, pp. 1487–1492, 2003.

- [26] C. Yuan, Q. Liu, and B. Xu, "Strain-induced structural phase transition of Si nanoparticles," *The Journal of Physical Chemistry C*, vol. 115, no. 33, pp. 16374–16377, 2011.
- [27] C. L. Yuan, B. Xu, and W. Lei, "Strain-induced direct band gap LaAlO_3 nanocrystals," *Materials Letters*, vol. 68, no. 1, pp. 392–394, 2012.
- [28] C. L. Yuan, H. Cai, P. S. Lee, J. Guo, and J. He, "Tuning photoluminescence of Ge/GeO_2 core/shell nanoparticles by strain," *Journal of Physical Chemistry C*, vol. 113, no. 46, pp. 19863–19866, 2009.
- [29] H. Huebner, D. L. Dewhurst, D. E. Smith et al., *The Finite Element Method for Engineers*, John Wiley & Sons, New York, NY, USA, 2001.
- [30] C. L. Johnson, E. Snoeck, M. Ezcurdia et al., "Effects of elastic anisotropy on strain distributions in decahedral gold nanoparticles," *Nature Materials*, vol. 7, no. 2, pp. 120–124, 2008.
- [31] Z. W. Shan, G. Adesso, A. Cabot et al., "Ultrahigh stress and strain in hierarchically structured hollow nanoparticles," *Nature Materials*, vol. 7, no. 12, pp. 947–952, 2008.
- [32] J. Grönqvist, N. Søndergaard, F. Boxberg, T. Guhr, S. Åberg, and H. Q. Xu, "Strain in semiconductor core-shell nanowires," *Journal of Applied Physics*, vol. 106, no. 5, Article ID 053508, 2009.
- [33] D. Baretton, S. Madsen, B. Lassen, and M. Willatzen, "Comparison of wurtzite atomistic and piezoelectric continuum strain models: implications for the electronic band structure," *Superlattices and Microstructures*, vol. 47, no. 1, pp. 134–138, 2010.

Research Article

Experimental Determination of Effective Minority Carrier Lifetime in HgCdTe Photovoltaic Detectors Using Optical and Electrical Methods

**Haoyang Cui, Jialin Wang, Chaoqun Wang, Can Liu, Kaiyun Pi,
Xiang Li, Yongpeng Xu, and Zhong Tang**

Shanghai University of Electric Power, Shanghai 200090, China

Correspondence should be addressed to Haoyang Cui; cuihy@shiep.edu.cn

Received 28 November 2014; Accepted 24 January 2015

Academic Editor: Wen Lei

Copyright © 2015 Haoyang Cui et al. This is an open access article distributed under the Creative Commons Attribution License, which permits unrestricted use, distribution, and reproduction in any medium, provided the original work is properly cited.

This paper presents experiment measurements of minority carrier lifetime using three different methods including modified open-circuit voltage decay (PIOCVD) method, small parallel resistance (SPR) method, and pulse recovery technique (PRT) on *pn* junction photodiode of the HgCdTe photodetector array. The measurements are done at the temperature of operation near 77 K. A saturation constant background light and a small resistance paralleled with the photodiode are used to minimize the influence of the effect of junction capacitance and resistance on the minority carrier lifetime extraction in the PIOCVD and SPR measurements, respectively. The minority carrier lifetime obtained using the two methods is distributed from 18 to 407 ns and from 0.7 to 110 ns for the different Cd compositions. The minority carrier lifetime extracted from the traditional PRT measurement is found in the range of 4 to 20 ns for $x = 0.231\text{--}0.4186$. From the results, it can be concluded that the minority carrier lifetime becomes longer with the increase of Cd composition and the pixels dimensional area.

1. Introduction

Minority carrier lifetime is an important characteristic to evaluate the quality of photovoltaic material and the performance of the photoelectronic devices [1]. The basic theory of minority carrier recombination through recombination centers was put forth in 1952 [2]. Even though many techniques have been developed in order to determine the minority carrier lifetime for Si-based or Ge-based devices, the carrier lifetime for the HgCdTe photovoltaic infrared focal plane array (IRFPA) photodetector [3–6] is still a puzzling question, especially for the *pn* junction devices. This is because the instability of HgCdTe material, in which the characteristics may change during the formation process of device, results in the differences between the actual and design parameters such as carrier concentration and the junction depth and so forth. These issues have many uncertainties effects on the minority carrier lifetime in the *pn* junction device.

Previous studies results show that the lifetime obtained is widely distributed in the range of $\text{ns}\sim\mu\text{s}$ [7] for different

testing techniques, Cd composition, active junction area, and growth conditions. Since the investigation of the carrier lifetime is beneficial to understand the recombination mechanism, the measurements must be carried out on the actual devices to extract the minority carrier lifetime. Here, on the junction type HgCdTe IRFPA, we compare minority carrier lifetimes measured by PIOCVD method [8, 9], SPR method [10], and PRT [11] for a series of Cd compositions and the pixels dimensional area.

2. Device Description and Experimental Setup

The $\text{Hg}_{1-x}\text{Cd}_x\text{Te}$ photovoltaic array detector was grown by MBE epitaxy on GaAs substrates. An ion implantation was fabricated on the *p*-type HgCdTe layer through B^+ ion implantation to form the n^+ region. The acceptor and donor concentration were $N_a \approx 8 \times 10^{15} \text{ cm}^{-3}$ and $N_d \approx 1 \times 10^{17} \text{ cm}^{-3}$, respectively. The n^+ heavy-doping area was $50 \times 50 \mu\text{m}^2$ or $28 \times 28 \mu\text{m}^2$. A ZnS film was evaporated on the surface

as a passivation layer. The metal contacts were deposited on either side of the *n*-on-*p* junctions in preparation for photovoltaic measurements. The sample was mounted in a liquid nitrogen-cooled Dewar for measurements and the temperature was close to 77 K.

The transient photovoltage of the photodetector was stimulated by the incident laser pulse, which was generated by an optical parametric oscillator (OPO) and difference frequency generator (DFG) pumped with a picosecond Nd:YAG pulsed laser. The laser pulse duration was 30 ps and the repetition rate was 10 Hz. An Oriel THL (tungsten halogen lamp, Oriel 63355) was used as the bias light source to stimulate the steady-state photovoltage. The nanosecond electric pulses in the PRT measurement were generated by an Agilent 33250A. The sample under test was connected via BNC coaxial cable in series with a 50 Ohm matched load resistance. An Agilent Infiniium 54832B oscilloscope was used to record the optical and electrical methods signals obtained.

3. Lifetime Measurement Techniques and Results Discussions

3.1. Photo-Induced Open-Circuit Voltage Decay Method. Theoretically, when the HgCdTe photodiode is excited by the pulsed laser, the photoresponse shows a rapid increase and slow decay process. As it has been analyzed in the previous report [8, 9], however, the decay curve profiles are dominated by the *RC* discharge time constant and trap energy level capture effects on excess carrier's relaxation. In order to minimize the effects of the equivalent junction capacitor and the carrier traps in the HgCdTe photodiode, a constant background illumination has been introduced in the traditional OCVD method, which can be called photo-induced open-circuit voltage decay (PIOCVD) method.

The composition of $\text{Hg}_{1-x}\text{Cd}_x\text{Te}$ in our experiments is $x = 0.231$ ($\lambda_{\text{Eg}} \sim 8.6 \mu\text{m}$), $x = 0.305$ ($\lambda_{\text{Eg}} \sim 4.6 \mu\text{m}$), $x = 0.343$ ($\lambda_{\text{Eg}} \sim 3.7 \mu\text{m}$), and $x = 0.418$ ($\lambda_{\text{Eg}} \sim 2.9 \mu\text{m}$). The detectors were processed into $50 \times 50 \mu\text{m}^2$ area of planar structures. By increasing the bias light intensity, the steady-state photovoltage will saturate the junction potential barrier of the photodiode. When the steady-state photovoltage does not increase with the rising of the background intensity, the photogenerated carriers recombination will dominate the decay time constant, which is related to the minority carrier lifetime. In agreement with this picture, photovoltage transient decay can be fitted by a one-order exponential function.

Figure 1 shows the situation that the DC photovoltage has been saturated. The photovoltage transient decay time constant can be determined from the best fit to the experiment, and consequently the minority carrier lifetime is obtained. The results show that the minority carrier lifetime is in the range of 18~407 ns for $x_{\text{Cd}} = 0.231\sim0.4186$ at 77 K. With the Cd composition increasing, the minority carrier lifetimes show an increasing tendency. By comparing the lifetime values of different pixels in one-component array, it is found that there are some distinctions between the different pixels, which can be attributed to the nonuniformity of the HgCdTe

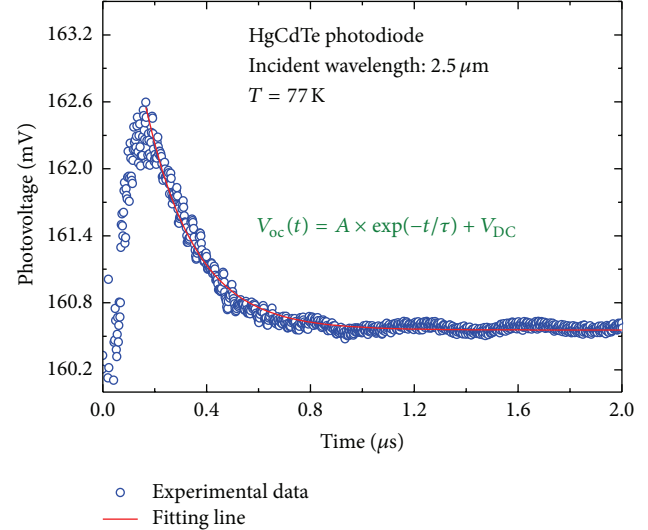


FIGURE 1: Photovoltaic transient profile of the HgCdTe photodiode illuminated by the laser pulses and the saturate bias light intensity.

material or due to the fabrication process variations of the detector.

3.2. Small Parallel Resistance Method. In order to minimize the effects of the equivalent junction, we can parallel a small resistance in the load circuit of the photodiode in the transient photovoltage measurement, which is called the small parallel resistance (SPR) method [10]. In this situation, the load resistance combines with the junction series resistance to parallel with the junction shunt resistance. Although all these resistances contribute to the *RC* discharge time constant and impact the photovoltage decay curve, the influence of the junction shunt resistance on the *RC* constant can be minimized because the load resistance and the junction series resistance are much less than the junction shunt resistance. Thus, the delay effect of the *RC* discharging process on the photovoltaic decay curve is weakened and the time constant will be dominated by the minority carrier recombination, consequently.

The dependence of bias light intensity on the photovoltage decay profile in SPR is very different from that in the PIOCVD measurement. Figure 2 is the photovoltage of the HgCdTe photodiode illuminated by laser pulses with different bias light intensity when a 50Ω resistance has been connected in the load circuit. Since the bias light illuminating nearly does not influence the transient photovoltage curves, *RC* discharging can be excluded from the photovoltage decay process; therefore, the minority carrier lifetime can be correlated to the decay time constant. The area size measured in the experiment is $50 \times 50 \mu\text{m}^2$ and $28 \times 28 \mu\text{m}^2$. The one-order exponential function can fit well with the experiment indicating that transient photovoltage decay is an exponential characteristic, which is shown in Figure 3. Thus, the photo-generated minority carrier lifetime can be extracted. Using this method, we measured the minority carrier lifetimes for different Cd components and different area dimensions of the

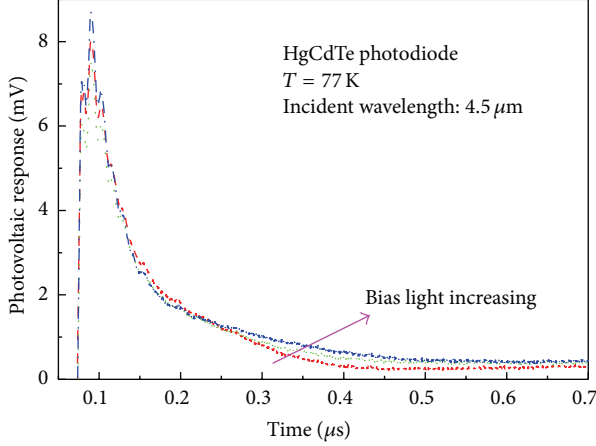


FIGURE 2: Photoresponse of the HgCdTe photovoltaic detector illuminated by laser pulses with different bias light intensity with a small resistance paralleled in the load circuit.

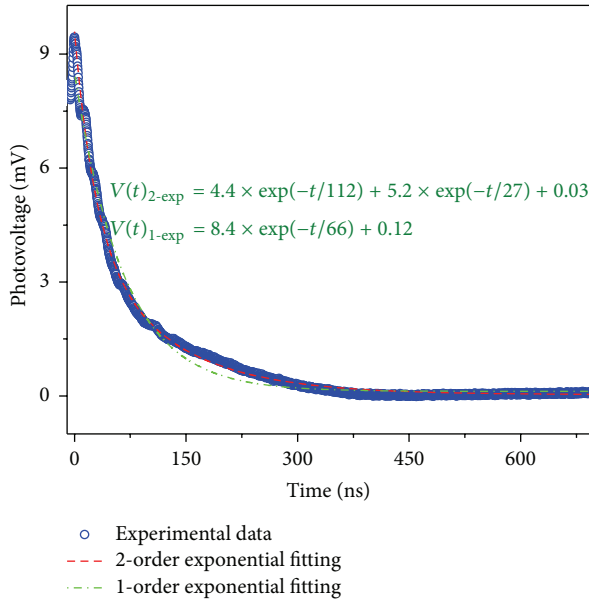


FIGURE 3: Photovoltaic profile of the detector illuminated by laser pulse.

HgCdTe photodiode. They show that the carrier lifetime is in the range of 0.7~110 ns at 77 K. The lifetime becomes longer with the increase of Cd composition that is consistent with the PIOCVD measurement result. The results also show that the minority carrier lifetime decreases with decreasing area because of perimeter surface recombination effects, which coincides with previous works [12, 13].

3.3. Pulse Recovery Technique. The pulse recovery technique (PRT) [11] is a widely used method to determine the minority carrier lifetime in the pn junction diodes, which was developed in 1954. When the photodiode is rapidly switched from forward into reverse bias, the excess minority carriers which remained from forward bias injection must recombine

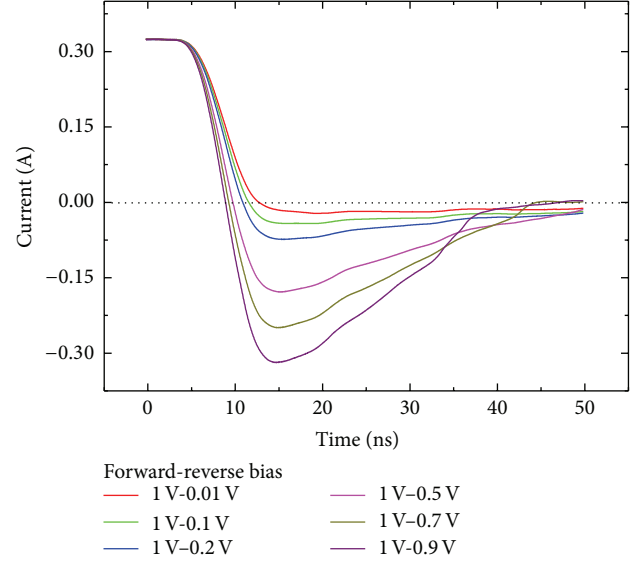


FIGURE 4: Reverse recovery current transient recorded on the diode as a function of varying initial reverse bias.

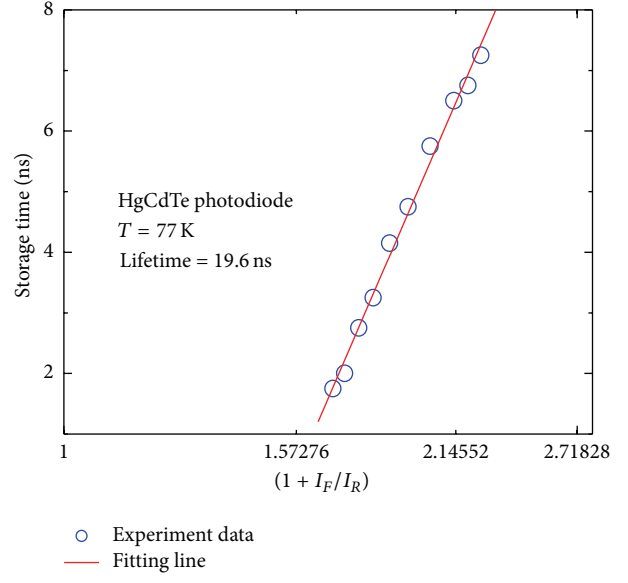


FIGURE 5: The storage time versus the current ratio I_F/I_R .

before current flow through the diode can drop to near zero [14]. There are two different decay phases which can be distinguished in the reverse current signals: one is the constant recovery current component and the other one is the reverse current dropping to near zero subsequently. Figure 4 shows the reverse recovery current transient recorded on the device as a function of varying initial reverse bias. The average minority carrier lifetime τ can be calculated from t_s and the ratio of forward current to reverse current, which is shown in Figure 5.

The active area of the devices used in this experiment is $50 \times 50 \mu\text{m}^2$ and $28 \times 28 \mu\text{m}^2$. The lifetime distributes in the range of 4 to 30 ns for $x_{\text{Cd}} = 0.231 \sim 0.419$ at 77 K. The

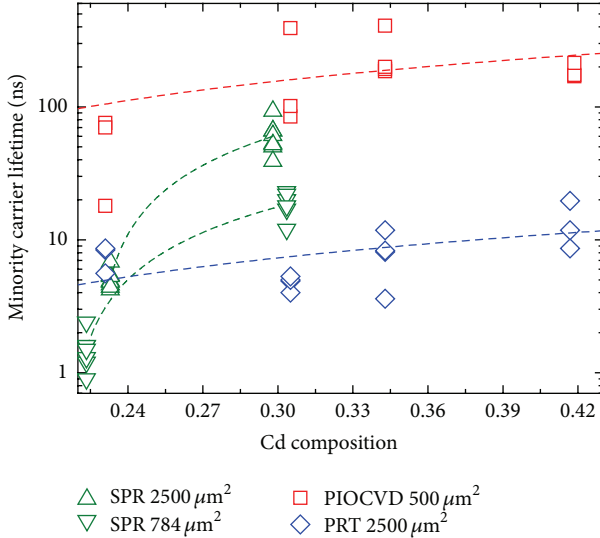


FIGURE 6: The variation of the extracted lifetime values with Cd composition using three experimental methods.

results also show that the value of the lifetime becomes longer with the increase of Cd composition. This is also consistent with the PIOCVD and SPR measurement results.

3.4. Results Discussions. From the above discussion, we measured the HgCdTe photodiode with different Cd compositions and the pixels dimensional area using the three different techniques including PIOCVD, SPR, and PRT. The minority carrier lifetime extracted from these methods is summarized and shown in Figure 6. It is clear that no matter which kind of experiment methods is adopted the minority carrier lifetime values obtained from these methods show the same increasing trend with the increase of Cd compositions. The values of the minority carrier lifetime show the increase with the increase of Cd composition. On the other hand, the minority carrier lifetimes extracted from the three methods are unequal. For example, the carrier lifetime obtained from PIOCVD is sometimes bigger than the ones from PRT. This is because the *RC* effect cannot be avoided in a *pn* junction photodiode no matter in what bias-light conditions in PIOCVD measurement. Since the *RC* discharging process delays the photovoltage decay cure, the minority carrier lifetime is bigger than the real values. In addition, the entire region of the device is in a high-injection condition, and the minority carrier lifetimes are larger than low injection [1], consequently. For the PRT measurements, recombination theory dictates that the minority carrier lifetime will be affected seriously by the surface recombination. Particularly, for the thin base region photovoltaic device, its dominance effect is even more pronounced. The effective minority lifetime profile can be given by including both surface recombination and diffusion of carriers:

$$\tau_{\text{eff}} = \frac{d}{S} + \frac{d^2}{\pi^2 D}, \quad (1)$$

where d is the simple thickness perpendicular to the surface plane, S is the surface recombination velocity, and D is the diffusion coefficient. This equation describes the effective carrier lifetime as a function of depth due to the surface recombination and diffusion of carriers within the sample to the surface. In this reason, the measured value is smaller than the base region value. Another correlate point to be cleared up is the influence of pixels dimensional area on the minority carrier lifetime measurement. Form Figure 6, one can see that the minority carrier lifetime of HgCdTe photodiode with the pixels dimensional area of $2500 \mu\text{m}^2$ is larger than that with the pixels dimension area of $784 \mu\text{m}^2$ in the SPR measurements. Because the HgCdTe IRFPA was fabricated to the planar junction structure, the active area is related to the junction area. Large decrease in the lifetime with decreasing device size suggests that surface recombination plays an important role in limiting effective device minority carrier lifetime which may be interpreted as the effect of specific surface area on the minority carrier lifetime [15]. The smaller the pixel dimension area is, the larger the specific surface area is, and the greater the effect of surface recombination is, consequently.

4. Conclusion

In summary, the work described in this paper presented the two kinds of minority carrier lifetime optical measurement methods including the PIOCVD method and the SPR method and the electrical method based on PRT. In the optical measurement method, a constant bias light illumination and a small resistance parallel in the load circuit were used to minimize the junction *RC* discharging process, respectively. The measurement results of the three methods show that the values of the minority carrier lifetime will increase with the increase of Cd compositions. It also shows that the lifetime of PIOCVD is larger than that of PRT, which can be attributed to the *RC* discharging effect in PIOCVD and strong surface recombination effect in PRT. The experiment methods and the conclusion of this paper will have significance for the HgCdTe device design and optimization.

Conflict of Interests

The authors declare that they have no conflict of interests related to this work.

Acknowledgment

The project is supported by the National Natural Science Foundation of China (61107081).

References

- [1] S. Johnston, K. Zaunbrecher, R. Ahrenkiel, D. Kuciauskas, D. Albin, and W. Metzger, "Simultaneous measurement of minority-carrier lifetime in single-crystal CdTe using three transient decay techniques," *IEEE Journal of Photovoltaics*, vol. 4, no. 5, pp. 1295–1300, 2014.

- [2] D. K. Schröder, "Carrier lifetimes in silicon," *IEEE Transactions on Electron Devices*, vol. 44, no. 1, pp. 160–170, 1997.
- [3] W. C. Qiu and W. D. Hu, "Laser beam induced current microscopy and photocurrent mapping for junction characterization of infrared photodetectors," *Science China Physics, Mechanics & Astronomy*, vol. 58, no. 2, pp. 1–13, 2015.
- [4] W.-D. Hu, X.-S. Chen, Z.-H. Ye et al., "Dependence of ion-implant-induced LBIC novel characteristic on excitation intensity for long-wavelength HgCdTe-based photovoltaic infrared detector pixel arrays," *IEEE Journal on Selected Topics in Quantum Electronics*, vol. 19, no. 5, Article ID 4100107, 2013.
- [5] W. Hu, Z. Ye, L. Liao et al., "A 128×128 long-wavelength/mid-wavelength two-color HgCdTe infrared focal plane array detector with ultra-low spectral crosstalk," *Optics Letters*, vol. 39, pp. 5130–5133, 2014.
- [6] J. Liang, W. Hu, Z. Ye et al., "Improved performance of HgCdTe infrared detector focal plane arrays by modulating light field based on photonic crystal structure," *Journal of Applied Physics*, vol. 115, no. 18, Article ID 184504, 2014.
- [7] D. Y. Tang and Z. Y. Mi, *Introduction to Optoelectronic Devices*, Shanghai Science and Technology Literature Press, 1989.
- [8] H. Cui, Z. Li, Z. Ye, X. Hu, and W. Lu, "Methods for determining minority carrier lifetime in HgCdTe photovoltaic detectors," in *Proceedings of the 34th International Conference on Infrared, Millimeter, and Terahertz Waves (IRMMW-THz '09)*, September 2009.
- [9] H. Cui, N. Tang, and Z. Tang, "Experimental determination of minority carrier lifetime and recombination mechanisms in MCT photovoltaic detectors," in *Proceedings of the 12th International Conference on Numerical Simulation of Optoelectronic Devices (NUSOD '12)*, pp. 39–40, August 2012.
- [10] H. Cui, C. Wang, J. Wang et al., "Measurement of minority carrier lifetime in infrared photovoltaic detectors using parallel circuit method," *Optical and Quantum Electronics*, 2014.
- [11] V. K. Khanna, "Physical understanding and technological control of carrier lifetimes in semiconductor materials and devices: a critique of conceptual development, state of the art and applications," *Progress in Quantum Electronics*, vol. 29, no. 2, pp. 59–163, 2005.
- [12] P. J. Drummond, D. Bhatia, and J. Ruzyllo, "Measurement of effective carrier lifetime at the semiconductor-dielectric interface by Photoconductive Decay (PCD) Method," *Solid-State Electronics*, vol. 81, pp. 130–134, 2013.
- [13] H. Jeong, H. Song, Y. Pak et al., "Enhanced light absorption of silicon nanotube arrays for organic/inorganic hybrid solar cells," *Advanced Materials*, vol. 26, no. 21, pp. 3445–3450, 2014.
- [14] D. L. Polla, S. P. Tobin, M. B. Reine, and A. K. Sood, "Experimental determination of minority-carrier lifetime and recombination mechanisms in p-type $Hg_{1-x}Cd_xTe$," *Journal of Applied Physics*, vol. 52, no. 8, pp. 5182–5194, 1981.
- [15] P. G. Neudeck, "Perimeter governed minority carrier lifetimes in 4H-SiC p⁺n diodes measured by reverse recovery switching transient analysis," *Journal of Electronic Materials*, vol. 27, no. 4, pp. 317–323, 1998.

Research Article

Modeling and Simulation of a Resonant-Cavity-Enhanced InGaAs/GaAs Quantum Dot Photodetector

W. W. Wang, F. M. Guo, and Y. Q. Li

Shanghai Key Laboratory of Multidimensional Information Processing, Key Laboratory of Polar Materials & Devices, School of Information Science Technology, East China Normal University, No. 500, Dong Chuan Road, Shanghai 200241, China

Correspondence should be addressed to F. M. Guo; fmguo@ee.ecnu.edu.cn

Received 27 November 2014; Accepted 25 December 2014

Academic Editor: Wen Lei

Copyright © 2015 W. W. Wang et al. This is an open access article distributed under the Creative Commons Attribution License, which permits unrestricted use, distribution, and reproduction in any medium, provided the original work is properly cited.

We simulated and analyzed a resonant-cavity-enhanced InGaAs/GaAs quantum dot n-i-n photodiode using Crosslight Apsys package. The resonant cavity has a distributed Bragg reflector (DBR) at one side. Comparing with the conventional photodetectors, the resonant-cavity-enhanced photodiode (RCE-PD) showed higher detection efficiency, faster response speed, and better wavelength selectivity and spatial orientation selectivity. Our simulation results also showed that when an AlAs layer is inserted into the device structure as a blocking layer, ultralow dark current can be achieved, with dark current densities 0.0034 A/cm at 0 V and 0.026 A/cm at a reverse bias of 2 V. We discussed the mechanism producing the photocurrent at various reverse bias. A high quantum efficiency of 87.9% was achieved at resonant wavelength of 1030 nm with a FWHM of about 3 nm. We also simulated InAs QD RCE-PD to compare with InGaAs QD. At last, the photocapacitance characteristic of the model has been discussed under different frequencies.

1. Introduction

Low dimensional III-V semiconductor nanostructures have been widely studied on their electronic and optical properties for device applications. Among the nanostructures, the resonant-cavity-enhanced photodetectors (RCE-PDs) have been extensively studied due to their novel physical mechanism and special device applications over the past two decades [1–7]. A RCE-PD is usually constructed by placing multiple active layers at the peak positions of a standing wave in a resonant cavity, sandwiched between two distributed Bragg reflectors (DBRs).

The DBR mirrors are usually made of quarter wave stacks with a periodic modulation of refractive indices. Metals are usually not used as mirrors because they do not provide wavelength selectivity [2]. RCE-PDs also have the ability of wavelength selectivity. When light is incident on the detector, the light will enter the cavity and interfere in the internal cavity which consisted of two mirrors if the wavelength and the cavity mode match. So optical field is enhanced and more light will be absorbed, generating more carriers in the cavity. Compared with the conventional detectors, the responsivity is greatly improved. This makes the RCE-PD with high

detection efficiency, fast response speed, ability to work in the absence of bias voltage, and their wavelength selectivity and spatial orientation selectivity especially suitable for optical fiber communication system that requires high wavelength accuracy.

1.06 μm is a specific wavelength used in Nd:YAG laser systems. These systems have been widely deployed in industrial manufacturing, medicine, remote sensing, space communication, and so forth. To achieve high sensitive detection at this wavelength, resonant-cavity-enhanced-(RCE-) PDs with quantum dots (QDs) as absorption layers were explored to reach a peak quantum efficiency of 65–75% [8–10]. However, DBR mirrors make it difficult for the device to extract photogenerated carriers. To solve this problem, Bennett et al. and Sun et al. fabricated an InGaAs/GaAs quantum dot n-i-n RCE-PDs with only a bottom DBR mirror which still has the resonant coupling nature and achieved peak photoresponsivity of 0.75 A/W at 1.4 V [11, 12].

2. Materials and Methods

The device structure to be imported into APSYS was constructed according to the structure in [12]. As shown in

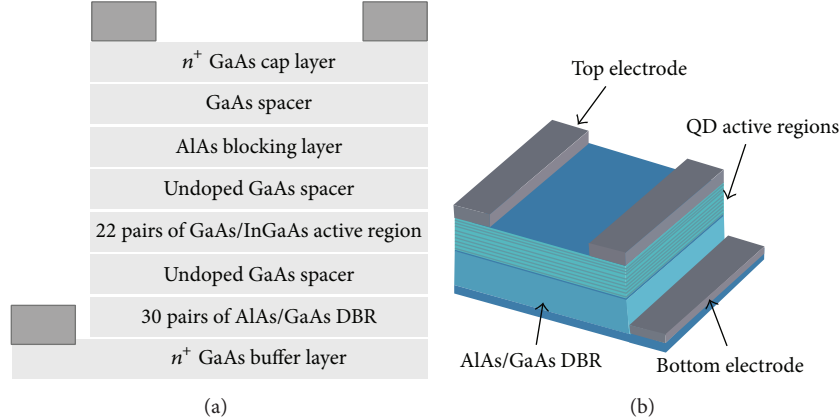


FIGURE 1: (a) The schematic diagram of the resonant-cavity-enhanced photodetector (RCE-PD). (b) The simplified 3D view of the device constructed.

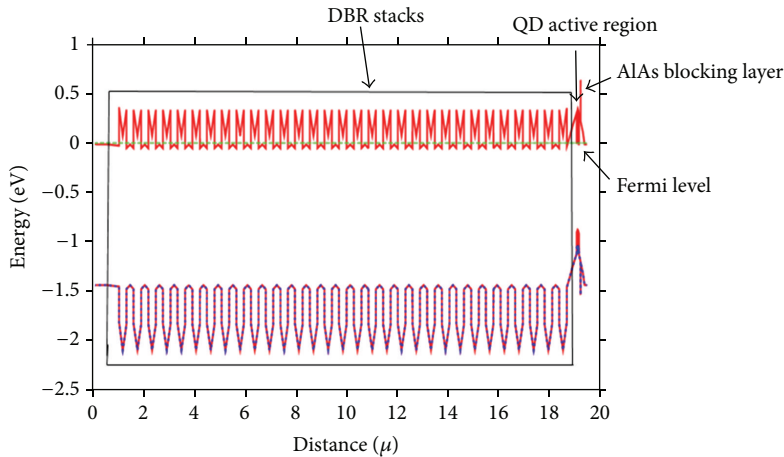


FIGURE 2: Energy band diagram profile along epitaxial growth direction under equilibrium.

Figure 1(a), it consists of a Si-doped $1\text{ }\mu\text{m}$ GaAs buffer layer and a DBR (n -doped) with 30 pairs of quarter-wavelength ($\lambda/4$) GaAs/AlAs layers. The active region is 380 nm thick undoped GaAs spacer and 23 periods of $6\text{ nm-In}0.5\text{Ga}0.5\text{As}$ QDs layers. Finally, the top layers in sequence are 50 nm undoped GaAs spacer, 3 nm thick AlAs blocking layer, 157 nm GaAs spacer, and a $175\text{ nm }n^+\text{ GaAs cap layer}$. The doping concentration for all the n^+ layers is $1 \times 10^{18}\text{ cm}^{-3}$. QD sheet density of $3 \times 10^{10}\text{ cm}^{-2}$ and a square ($80\text{ }\mu\text{m} \times 80\text{ }\mu\text{m}$) opening was left on the top for optical access. The temperature is set to be room temperature. Plotted in Figure 1(b) is a simplified 3D structure view of the device constructed by Lumerical software. The energy band diagram of the device at thermal equilibrium along the epitaxial growth direction is plotted in Figure 2.

Figure 3(a) is the simulated QD PL spectrum at room temperature. The peak at $1.13\text{ }\mu\text{m}$ is emission from the quantum dots and 960 nm is from the wetting layer [9, 13]. Figure 3(b) is the gain of the absorption layer at different incident wavelengths. The largest gain appearing at $1.13\text{ }\mu\text{m}$ indicated that electron-hole pairs generated in the active region reached a maximum.

3. Results and Discussion

Figure 4(a) is the current-voltage characteristics of the InGaAs QD RCE photodetector simulated at 1030 nm wavelength. The suppressed dark current in the n-i-n structure is attributed to the blocking effect by the AlAs layer. The current increases as the reverse bias increases. In the process of optical transition, the excited electrons from the conduction band and the excited holes from the valence band will form excitons in QDs. The quantum dots can capture the excitons very effectively. Potential barrier prevents the electron-hole from moving in the opposite direction. Thus the tunneling probability through the potential barrier is very small. Exciton ionization is mainly thermal ionization. The electron can escape from the quantum dots producing a photocurrent at a certain temperature. The escape of electrons and holes changes electric potential, resulting in a decrease of the effective potential barrier, which makes bound electrons and holes in the quantum dots tunnel through the barrier, thus increasing the photocurrent. It is observed that the dark current increases a little at 0.5 V or less. When the bias is 0.5 V , photocurrent is only 0.02 A/cm . The slow increase of photocurrent density at lower applied voltage is because

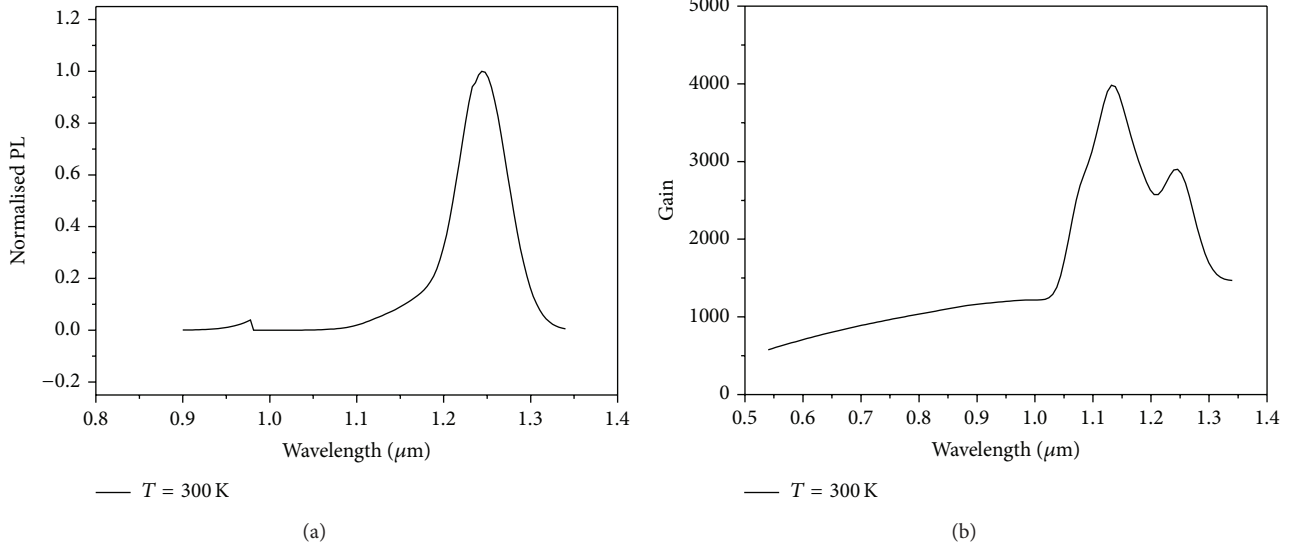
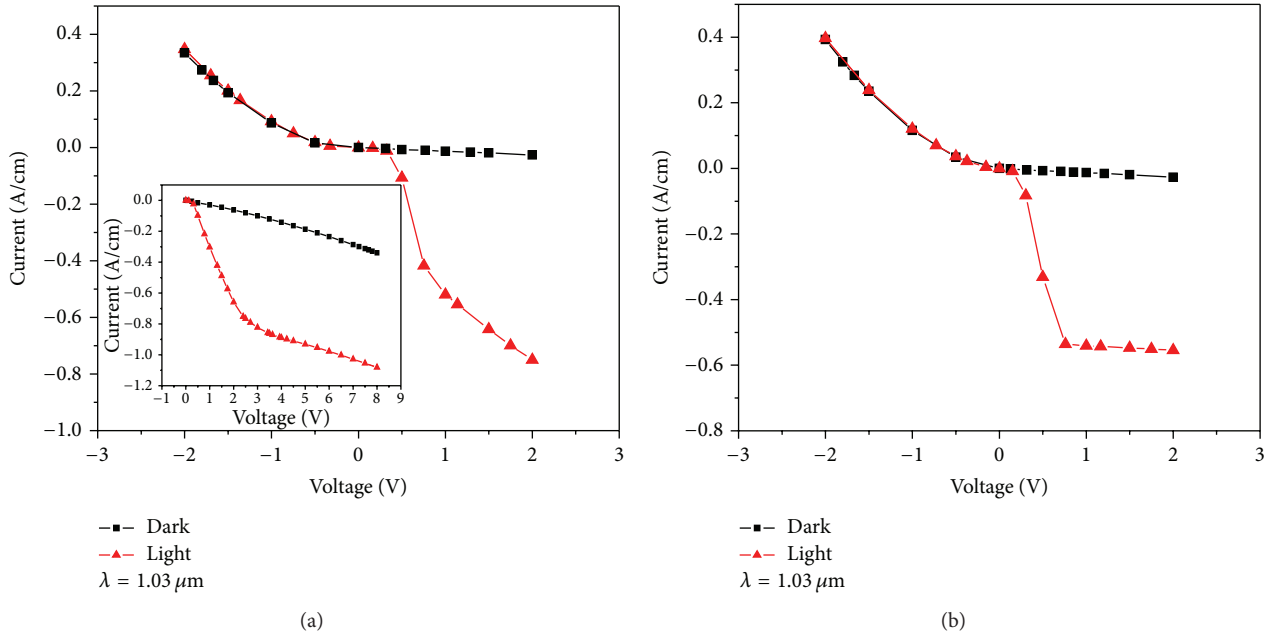


FIGURE 3: (a) Simulated PL spectrum. (b) Absorption layer gain spectrum.

FIGURE 4: (a) Current-voltage characteristics of the InGaAs QD RCE photodetector. The inset shows the I - V characteristics at high bias voltage. (b) Current-voltage characteristics of the InAs QD RCE photodetector.

the main mechanism for photocurrent generation is due to thermal ionization. We also found that as the bias increased from 0.5 V to 2 V the photocurrent density increased 1 order of magnitude from 0.02 A/cm to 0.34 A/cm. This rapid increase of photocurrent density is because the interaction of thermal ionization and tunneling ionization caused exciton ionization.

We also simulated I - V characteristic curve at high bias, as shown in Figure 4(a) inset. Photocurrent increases as the bias voltage increases. But when bias voltage exceeds 2 volts, photocurrent stays at about the same value as the bias voltage increases. This is because the majority of excitons are ionized

when bias voltage is above 2 volts and thus would not generate photocurrent.

The electric current characteristic (I - V) of InAs QD RCE simulated still to compare with InGaAs QD. But it is seen from Figure 4(b) that the photocurrent reaches saturation under low bias. So, the paper has discussed the effect of the resonant cavity, showing why the InGaAs/GaAs quantum dot is, rather than others quantum dot (InAs/GaAs).

The quantum efficiency of a QD-RCE photodetector is determined by the cavity resonant wavelength relative to the exciton absorption peak. When these two wavelengths overlap, the photodetector has the ideal quantum efficiency,

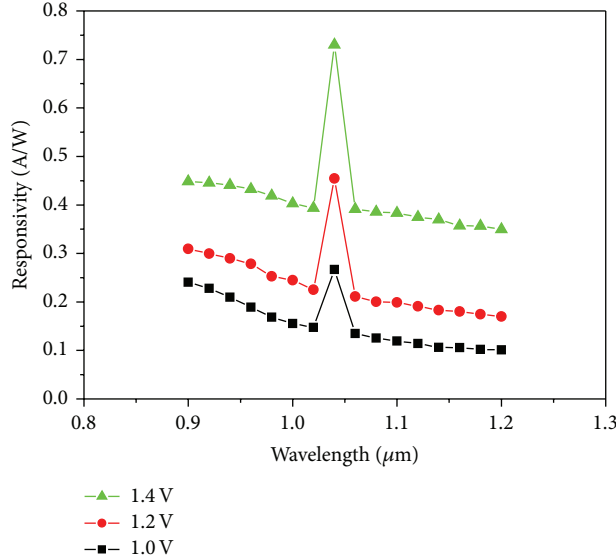


FIGURE 5: Responsivity spectra of the RCE photodetector under different reverse bias voltages.

showing wavelength selectivity. Full width at half maximum (FWHM) can reflect the wavelength selectivity of RCE photodetector. Consider

$$\text{FWHM} = \frac{\lambda_0^2 (1 - \sqrt{R_1 R_2} e^{-\xi \alpha d})}{2\pi n_g L_{\text{eff}} \sqrt[4]{R_1 R_2} e^{-\xi \alpha d/2}}. \quad (1)$$

Here, R_1 and R_2 are the reflection coefficients of the top DBR and the bottom DBR, respectively. α is the absorption coefficient and d the thickness of the absorption layer. L_{eff} is the equivalent cavity length, n_g is the group refraction rate, λ_0 is the mode wavelength, and ξ is the standing wave enhancement factor.

The device photocurrent spectra at different bias voltages were simulated. Figure 5 shows the spectral responsivity simulation of the RCE photodetector under different applied reverse bias voltages. The resonant peak wavelength was at 1030 nm with 3 nm full width at half maximum (FWHM). The responsivity increases with the applied reversed bias between 0 V and 3 V and maintains the same shape. The responsivity is approximately 0.25 A/W at 1.0 V bias and increases to 0.73 W/A upon 1.4 V bias and the quantum efficiency is 30.1% and 87.9%, respectively, which agrees with the reported results in [12].

Figure 6(a) shows the C-V simulation performed at $F = 100$ KHz, 1 MHz, and 10 MHz in InGaAs QDs. More carriers will extend across the QDs and the excited state and the ground state will be filled with increasing reverse bias. So, the higher the reverse bias, the larger the capacitance value, as a result of the greater portion of the QD assembly being populated [14–17]. We also simulated C-V characteristic of InAs QD RCE to compare with InGaAs QD as shown in Figure 6(b). The photocurrent has reached saturation at 1.0 V. It is similar to Figure 4(b), the I - V characteristic. The theoretical fit of the capacitance is obtained using a simple

model based on the definition of the capacitance ($C = dQ/dV$) [18] where the charge is given by the integral of the density of states and the energy distribution:

$$C_{\text{dot}} = qAL \sum_i \frac{\partial}{\partial V_{\text{dot}}} \left(\int D_i(E, V_{\text{dot}}) \times f(E, V_{\text{dot}}) dE \right). \quad (2)$$

The summation is assumed over all i subbands, where $D_i(E, V_{\text{dot}})$ is the electron density of state for i th subband in QDs, $f(E, V_{\text{dot}})$ is the Fermi-Dirac energy distribution, V_{dot} is the voltage across the quantum dots scaled by level-arm relation when the band bending is neglected, and L is the level arm coefficient.

Comparing with 90.3%, the experimentally measured results for quantum efficiency and the discrepancy in the device responsivity in our computed result can be attributed to the number of quantum dots used in simulation. The device in the experimental result has 22 pairs of QDs, whilst in simulation the lowest quantum dot number allowed was limited by the calculation procedure. And to some extent, this result further demonstrated QD RCE-PD's potential in achieving high quantum efficiency, high response rate, and better wavelength selectivity.

4. Conclusions

In summary, we have simulated an n-i-n RCE photodetector grown on a GaAs substrate with operating wavelength at 1.03 μ m. The responsivity is 0.73 A/W at 1.4 V bias with a FWHM of 3 nm. A high quantum efficiency of 87.9% was observed in the calculation. The device has reduced dark current of 0.0034 A/cm at the bias of 0 V and 0.026 A/cm at the reverse bias of 2.0 V.

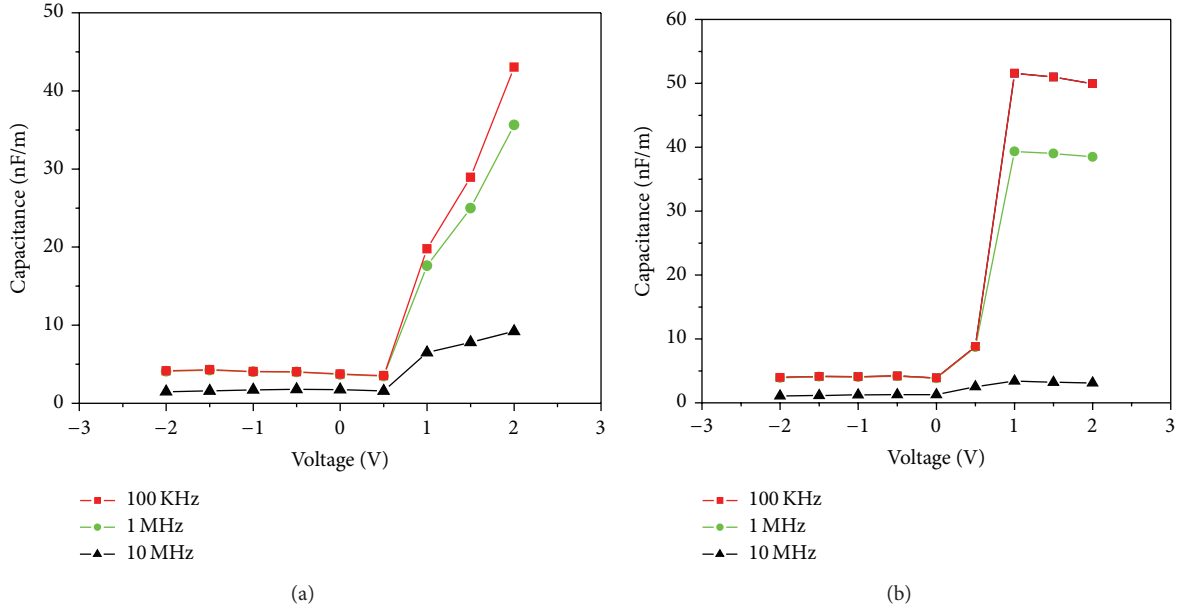


FIGURE 6: (a) C-V simulation figure of the InGaAs QD RCE photodetector under different frequencies. (b) C-V characteristics of the InAs QD RCE photodetector.

Conflict of Interests

The authors declare that there is no conflict of interests regarding the publication of this paper.

Acknowledgments

This work was supported by National Scientific Research Plan (2011CB932903) and State Scientific and Technological Commission of Shanghai (no. 118014546) and State Key Laboratory of Functional Materials for Informatics and National Laboratory for Terahertz Solid State Technology, Chinese Academy of Science.

References

- [1] A. Shen, H. C. Liu, M. Gao et al., "Resonant-cavity-enhanced p-type GaAs/AlGaAs quantum-well infrared photodetectors," *Applied Physics Letters*, vol. 77, no. 15, pp. 2400–2402, 2000.
- [2] A. Ramam, G. K. Chowdhury, and S. J. Chua, "An approach to the design of highly selective resonant-cavity-enhanced photodetectors," *Applied Physics Letters*, vol. 86, Article ID 171104, 3 pages, 2005.
- [3] Q. Han, X. H. Yang, Z. C. Niu et al., "1.55 μ m GaInNAs resonant-cavity-enhanced photodetector grown on GaAs," *Applied Physics Letters*, vol. 87, no. 11, Article ID 111105, 3 pages, 2005.
- [4] S. Q. Liu, Q. Han, B. Zhu et al., "High-performance metamorphic InGaAs resonant cavity enhanced photodetector grown on GaAs substrate," *Applied Physics Letters*, vol. 98, no. 20, Article ID 201104, 3 pages, 2011.
- [5] Q. Han, Z. C. Niu, L. H. Peng et al., "High-performance 1.55 μ m low-temperature-grown GaAs resonantcavity-enhanced photodetector," *Appliec Physics Letters*, vol. 89, Article ID 131104, 3 pages, 2006.
- [6] N. Guo, W. Hu, X. Chen, L. Wang, and W. Lu, "Enhanced plasmonic resonant excitation in a grating gated field-effect transistor with supplemental gates," *Optics Express*, vol. 21, no. 2, pp. 1606–1614, 2013.
- [7] M. Casalino, G. Coppola, M. Gioffr et al., "Microcavity silicon photodetectors at 1.55 μ m," *Advances in OptoElectronics*, vol. 2011, Article ID 965967, 10 pages, 2011.
- [8] O. Baklenov, H. Nie, K. A. Anselm, J. C. Campbell, and B. G. Streetman, "Multi-stacked quantum dot resonant-cavity photodetector operating at 1.06 μ m," *Electronics Letters*, vol. 34, no. 7, pp. 694–695, 1998.
- [9] H. Nie, O. Baklenov, P. Yuan, C. Lenox, B. G. Streetman, and J. C. Campbell, "Quantum-dot resonant-cavity separate absorption, charge, and multiplication avalanche photodiode operating at 1.06 μ m," *IEEE Photonics Technology Letters*, vol. 10, no. 7, pp. 1009–1011, 1998.
- [10] H. Zhang, H. Z. Zheng, P. Xu et al., "Tuning of detection wavelength in a resonant-cavity-enhanced quantum-dot-embedded photodiode by changing detection angle," *Chinese Physics Letters*, vol. 22, no. 6, pp. 1405–1408, 2005.
- [11] A. J. Bennett, D. C. Unitt, P. See et al., "Microcavity single-photon-emitting diode," *Applied Physics Letters*, vol. 86, no. 18, Article ID 181102, 3 pages, 2005.
- [12] X. M. Sun, H. Zhang, H. Zhu et al., "High responsivity resonant-cavity-enhanced InGaAs/GaAs quantum-dot photodetector for wavelength of ~1 μ m at room temperature," *Electronics Letters*, vol. 45, no. 6, pp. 329–331, 2009.
- [13] J. C. Campbell, D. L. Huffaker, H. Deng, and D. G. Deppe, "Quantum dot resonant cavity photodiode with operation near 1.3 μ m wavelength," *Electronics Letters*, vol. 33, no. 15, pp. 1337–1339, 1997.
- [14] H. Zhang, H.-Z. Zheng, P. Xu et al., "Tuning of detection wavelength in a resonant-cavity-enhanced quantum-dot-embedded photodiode by changing detection angle," *Chinese Physics Letters*, vol. 22, no. 6, pp. 1405–1408, 2005.

- [15] O. Saad, M. Baira, R. Ajjal et al., "Capacitance-voltage analysis of InAs quantum dots grown on InAlAs/InP(001)," *Microelectronics Journal*, vol. 39, no. 1, pp. 7–11, 2008.
- [16] G. R. Li, X. Zhou, F. H. Yang, P. H. Tan, H. Z. Zheng, and Y. P. Zeng, "Photo-capacitance response of internal tunnelling coupling in quantum-dot-imbedded heterostructures under selective photo-excitation," *Journal of Physics Condensed Matter*, vol. 16, no. 36, pp. 6519–6525, 2004.
- [17] W. Lu, Y. M. Mu, X. Q. Liu et al., "Direct observation of above-quantum-step quasibound states in GaAs/Al_xGa_{1-x}As/vacuum heterostructures," *Physical Review B—Condensed Matter and Materials Physics*, vol. 57, no. 16, pp. 9787–9791, 1998.
- [18] G. Medeiros-Ribeiro, F. G. Pikus, P. M. Petroff, and A. L. Efros, "Single-electron charging and Coulomb interaction in InAs self-assembled quantum dot arrays," *Physical Review B—Condensed Matter and Materials Physics*, vol. 55, no. 3, pp. 1568–1573, 1997.

Research Article

Determination of Temperature-Dependent Stress State in Thin AlGaN Layer of AlGaN/GaN HEMT Heterostructures by Near-Resonant Raman Scattering

Yanli Liu,¹ Xifeng Yang,^{1,2} Dunjun Chen,¹ Hai Lu,¹ Rong Zhang,¹ and Youdou Zheng¹

¹Key Laboratory of Advanced Photonic and Electronic Materials, School of Electronic Science and Engineering, Nanjing University, Nanjing 210093, China

²Jiangsu Laboratory of Advanced Functional Materials and College of Physics and Engineering, Changshu Institute of Technology, Changshu 215500, China

Correspondence should be addressed to Dunjun Chen; djchen@nju.edu.cn

Received 28 November 2014; Accepted 17 December 2014

Academic Editor: Wen Lei

Copyright © 2015 Yanli Liu et al. This is an open access article distributed under the Creative Commons Attribution License, which permits unrestricted use, distribution, and reproduction in any medium, provided the original work is properly cited.

The temperature-dependent stress state in the AlGaN barrier layer of AlGaN/GaN heterostructure grown on sapphire substrate was investigated by ultraviolet (UV) near-resonant Raman scattering. Strong scattering peak resulting from the A_1 (LO) phonon mode of AlGaN is observed under near-resonance condition, which allows for the accurate measurement of Raman shifts with temperature. The temperature-dependent stress in the AlGaN layer determined by the resonance Raman spectra is consistent with the theoretical calculation result, taking lattice mismatch and thermal mismatch into account together. This good agreement indicates that the UV near-resonant Raman scattering can be a direct and effective method to characterize the stress state in thin AlGaN barrier layer of AlGaN/GaN HEMT heterostructures.

1. Introduction

Recently, AlGaN/GaN heterostructures have attracted considerable attention due to their potential use in high-power, high-temperature, and high-frequency electronic devices [1–5]. The high-temperature application is one important advantage of the AlGaN/GaN-based devices over GaAs-based and Si devices [6–8]. It is well known that the strain and stress in the AlGaN barrier layer due to lattice mismatch (LMM) and thermal mismatch between AlGaN and the underlying layers have important effect on the formation and transport properties of two-dimensional electron gas (2DEG) in AlGaN/GaN heterostructures [9–11]. Therefore, the investigation on the temperature dependence of stress or strain in AlGaN barrier layer is necessary for understanding the temperature-dependent electrical properties of AlGaN/GaN heterostructure and improving the reliability of the AlGaN/GaN based devices.

In previous reports, the strain or stress in the AlGaN layer of AlGaN/GaN heterostructures was characterized typically by using X-ray diffraction [12, 13]. However, the reflection peaks of some asymmetric planes in AlGaN barrier layer are always invisible due to the thin thickness and poor interference of the plane [12]. So, the in-plane lattice constant and the biaxial strain of AlGaN layer cannot be measured directly using this method. Raman spectroscopy is an effective method for the residual stress measurement of crystal films. However, in the prior studies on Raman measurements of AlGaN/GaN heterostructures, the visible (532 nm, 488 nm) Raman spectroscopy is mainly used to detect the stress and 2DEG channel temperature by measuring the phonon frequency of GaN averaged over the whole buffer layer [14, 15], which cannot reflect directly the stress state in the AlGaN barrier layer.

In this work, we investigated the temperature-dependent stress state in the thin AlGaN barrier layer of AlGaN/GaN

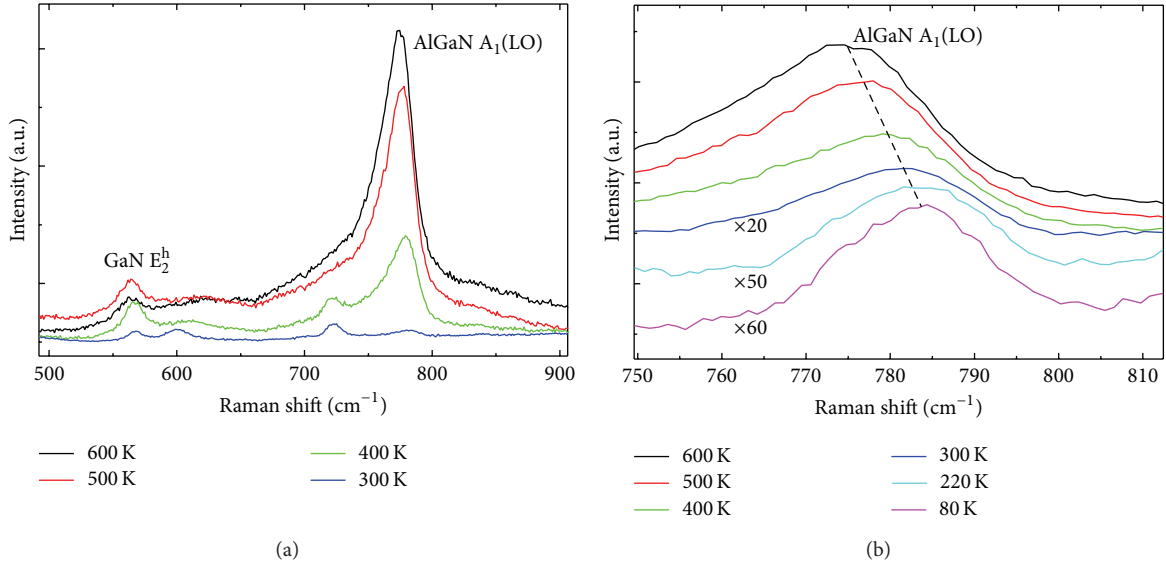


FIGURE 1: (a) UV Raman spectra of AlGaN/GaN heterostructure with varying temperature and (b) the local amplified graph of the $A_1(\text{LO})$ mode of AlGaN.

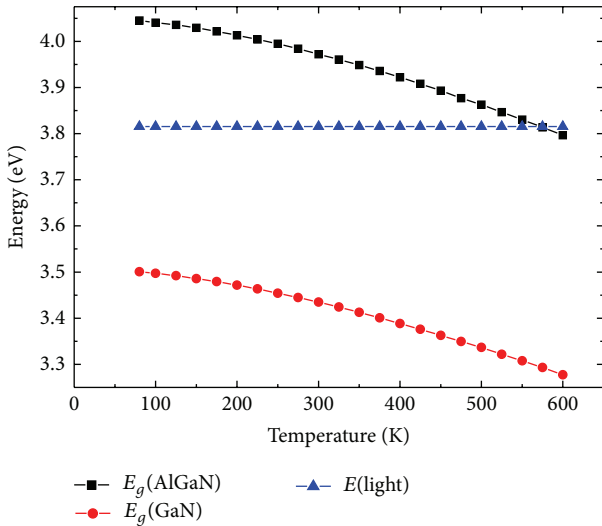


FIGURE 2: Temperature-dependent band gaps of the AlGaN/GaN heterostructure.

heterostructure by means of UV near-resonant Raman scattering. The Raman measured results are in good agreement with those from theoretical calculation, taking LMM and thermal mismatch into account together.

2. Experiment

The AlGaN/GaN heterostructure used in this study was grown on sapphire substrate by metal-organic chemical vapor deposition. The sample consists of a 2 μm thick unintentionally doped GaN layer, a 1 nm thick AlN spacer layer, and a 25 nm thick undoped $\text{Al}_{0.27}\text{Ga}_{0.73}\text{N}$ barrier layer.

The Raman scattering spectra were recorded by using an HR800 Jobin-Yvon spectrometer equipped with a liquid-nitrogen-cooled charge-coupled device in a backscattering geometry. A 325 nm He-Cd laser was used as an excitation source. A temperature stage with a quartz window was used to heat the sample from 80 to 600 K in flowing nitrogen.

3. Results and Discussion

3.1. The Stress in AlGaN Barrier Layer Determined by Near-Resonant Raman Scattering. The temperature-dependent UV Raman spectra of AlGaN/GaN heterostructure are shown in Figure 1. Compared to the visible Raman spectrum of AlGaN/GaN heterostructure [19], a new peak near 785 cm^{-1} occurs in the UV Raman spectrum. This peak corresponds to the $A_1(\text{LO})$ mode of the AlGaN layer according to the Al-composition dependent $A_1(\text{LO})$ phonon frequency [20]. As shown in Figure 1, the $A_1(\text{LO})$ phonon mode of the AlGaN layer shows enhancement effect in intensity and red shift in frequency with increasing temperature.

The temperature dependence of the intensity of the $A_1(\text{LO})$ phonon mode in AlGaN can be explained by studying the resonant Raman scattering in the structure with varying temperatures. By solving the Schrodinger and Poisson equations self-consistently using the Silvaco Atlas software, we can get the band diagram of the structure with varying temperature. The band gaps of AlGaN and GaN in the temperature range of 80–600 K are shown in Figure 2. The band gap of the AlGaN barrier layer is closer to the excitation energy than that of the GaN layer in the whole temperature range. The resonant Raman scattering arises from the AlGaN barrier layer. The band gap of the AlGaN barrier layer decreases and becomes closer and closer to the excitation energy with the increasing temperature. So, the intensity of the $A_1(\text{LO})$ phonon mode of AlGaN increases with the increasing temperature.

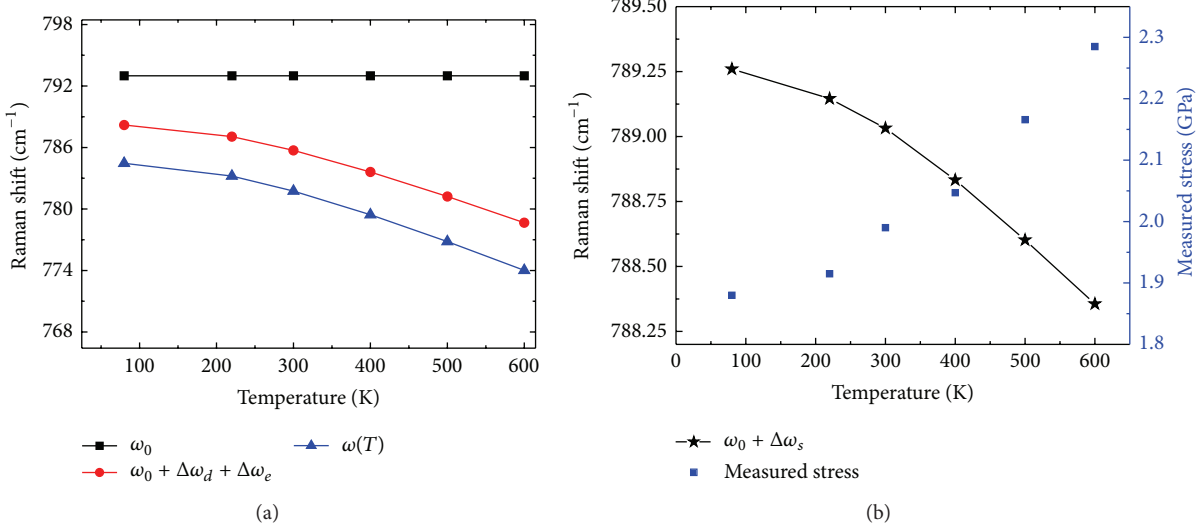


FIGURE 3: (a) Raman shift of A₁(LO) mode of AlGaN as a function of temperature together with the contribution of thermal expansion of lattice and phonon decay effects. (b) Temperature-dependent stress in AlGaN and its contribution to the Raman shift.

TABLE 1: Model parameters for AlGaN, GaN, and substrate [16].

Material	θ_1 (K)	θ_2 (K)	θ_3 (K)	θ_4 (K)	X_1 (10 ⁻⁷ /K)	X_2 (10 ⁻⁷ /K)	X_3 (10 ⁻⁷ /K)	X_4 (10 ⁻⁷ /K)
GaN								
<i>a</i>	75	581.25	1684.375		0.487	52.152	4.21	
<i>c</i>	75	590.625	1675		0.621	47.312	1.125	
AlN								
<i>a</i>	125	600	1852.5		-4.348	44.074	35.056	
<i>c</i>	100	528.75	1723.75		-5.174	29.857	39.565	
Al_{0.27}Ga_{0.73}N								
<i>a</i>	88.5	586.313	1729.77		-0.0818	4.997	1.254	
<i>c</i>	81.75	573.919	1688.16		-0.0943	4.26	1.1504	
Sapphire								
<i>a</i>	135	565.625	1231.25	5468.75	1.2176	53.401	35.613	23.661
<i>c</i>	135	598.438	1468.75	5198.438	2.856	72.079	23.202	29.087

There are several reasons for the frequency shift of phonon mode with varying temperature. The anharmonicity of the crystal lattice gives rise to the thermal expansion of lattice and phonon decay [21, 22]. The frequency shifts due to these two effects are denoted as $\Delta\omega_e(T)$ and $\Delta\omega_d(T)$, respectively. In an isotropic approximation, the term $\Delta\omega_e(T)$ is given by [21, 22]

$$\Delta\omega_e(T) = -\omega_0\gamma \int_0^T [\alpha_c(\tilde{T}) + 2\alpha_a(\tilde{T})] d\tilde{T}, \quad (1)$$

where α_a and α_c are the temperature-dependent thermal expansion coefficients along *a*- and *c*-directions, ω_0 is the harmonic frequency of the optical phonon mode, and γ is the Grüneisen parameter. Here, the thermal expansion coefficient with variable temperature was described within multifrequency Einstein model [16]. Consider

$$\alpha = \sum_{i=1}^n X_i \frac{(\theta_i/T)^2 \exp(\theta_i/T)}{[\exp(\theta_i/T) - 1]^2}, \quad (2)$$

where X_i and θ_i are model parameters listed in Table 1.

Taking into account symmetric decays of the zone-center phonons into two phonons and three phonons with frequencies $\omega_0/2$ and $\omega_0/3$, respectively, the term $\Delta\omega_d(T)$ can be described by [23]

$$\begin{aligned} \Delta\omega_d(T) = & A \left[1 + 2n\left(T, \frac{\omega_0}{2}\right) \right] \\ & + B \left[1 + 3n\left(T, \frac{\omega_0}{3}\right) + 3n^2\left(T, \frac{\omega_0}{3}\right) \right], \end{aligned} \quad (3)$$

where A and B are constants and $n(T, \omega) = [\exp(\hbar\omega/k_B T) - 1]^{-1}$ is the Bose-Einstein distribution function which describes the thermal occupation number of phonon states. The parameters γ , ω_0 , A , and B for AlGaN are 1.56, 793 cm⁻¹, -4.646 cm⁻¹, and -0.115 cm⁻¹, respectively. The contributions of the thermal expansion of lattice and phonon decay effect to the frequency shift of A₁(LO) mode in AlGaN are shown in Figure 3(a).

Besides the phonon frequency shift due to the thermal expansion of lattice and the decay of optical phonon into phonon with lower energy, the temperature-dependent stress

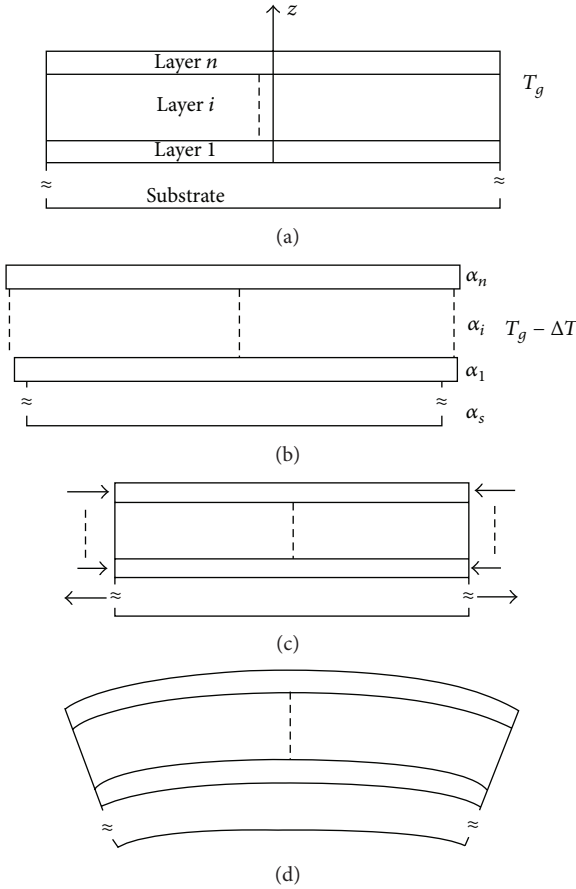


FIGURE 4: Schematic of the generation of thermal stress in multilayer structure.

in crystalline also contributes to the frequency shift, which is denoted as $\Delta\omega_s(T)$ [24]. Consider

$$\Delta\omega_s(T) = 2\tilde{a}_\lambda\sigma_{xx} + \tilde{b}_\lambda\sigma_{zz}. \quad (4)$$

For A_1 (LO) mode in $Al_{0.27}Ga_{0.73}N$, the phonon deformation potentials \tilde{a}_λ , \tilde{b}_λ equal 1.001 and $-1.576 \text{ cm}^{-1}/\text{GPa}$, respectively [24]. The temperature-dependent phonon frequency should be written as

$$\omega(T) = \omega_0 + \Delta\omega_e(T) + \Delta\omega_d(T) + \Delta\omega_s(T). \quad (5)$$

According to the measured $\omega(T)$ and the calculated $\Delta\omega_e(T)$ and $\Delta\omega_d(T)$ as shown in Figure 3(a), the temperature-dependent $\Delta\omega_s(T)$ and the corresponding stress in AlGaN can be obtained. The results are shown in Figure 3(b). The measured stress in AlGaN increased from 1.88 GPa at 80 K to 2.28 GPa at 600 K.

3.2. Theoretical Calculation. In order to identify the accuracy of the stress determination in thin AlGaN barrier layer by analyzing near-resonant Raman spectroscopy, we calculate the temperature-dependent stress state of AlGaN layer theoretically by applying a stress model with multilayer structure. The total stress in the AlGaN barrier layer of AlGaN/GaN

heterostructure grown on sapphire substrate consists of two parts: one is thermal stress due to thermal mismatch between AlGaN and the underlying GaN/substrate and the other is induced by LMM between AlGaN and GaN.

Figure 4 shows the analysis of thermal stress generated in multilayer structure [25]. An elastic multilayer structure at growth temperature T_g is shown schematically in Figure 4(a), where i denote layer number. When temperature decreases ΔT , there are unconstrained strains in different layers. Hence, the free thermal strain, $\alpha_i\Delta T$, is generated in this layer i , as shown in Figure 4(b). Then, in order to achieve displacement compatibility, uniform tensile/compressive stresses are imposed on the individual layers (Figure 4(c)). Finally, the whole structure bends due to the asymmetric stresses in the multilayer structure (Figure 4(d)).

Based on the logical analysis described in Figure 4, the thermal stress in the AlGaN/GaN/sapphire structure can be calculated using the analytical model proposed by Hsueh and Evans [26] which decomposes thermal strain into a uniform component and a bending component. The thermal stress in AlGaN by taking a first-order approximation (i.e., ignoring terms with orders of t_i higher than one) is expressed as follows [25]:

$$\sigma_{\text{thermal}} = \int_{T_g}^T Y_2 \left[\alpha_{a,s} - \alpha_{a,2} + 4 \frac{Y_1 t_1 (\alpha_{a,1} - \alpha_{a,s})}{Y_s t_s} + 4 \frac{Y_2 t_2 (\alpha_{a,2} - \alpha_{a,s})}{Y_s t_s} \right] dT, \quad (6)$$

where the subscripts s , 1, and 2 denote the substrate, GaN, and AlGaN, respectively, Y is biaxial modulus given in terms of elastic constants C_{ij} as $Y = C_{11} + C_{12} - 2C_{13}^2/C_{33}$, and t is layer thickness. Here, the elastic constants, biaxial modulus, and lattice constant of AlGaN are calculated from Vegard's law. The above parameters are listed in Table 2.

Based on the above analysis, the temperature-dependent thermal stress in AlGaN layer can be calculated numerically. The calculated result as shown in the insert of Figure 5 indicates that the biaxial compressive stress in AlGaN layer decreases with the increasing temperature in the temperature range of 80–600 K below growth temperature.

Besides the thermal stress, the stress due to LMM between AlGaN and GaN also contributes to the total stress in AlGaN. This stress can be calculated using the following equations [10]:

$$\begin{aligned} \varepsilon_{xx} &= \frac{a_1 - a_2}{a_2} = \frac{a_1}{a_2} - 1, \\ \sigma_{\text{LMM}} &= \left(C_{11} + C_{12} - \frac{2C_{13}^2}{C_{33}} \right) \varepsilon_{xx}, \end{aligned} \quad (7)$$

where a_1 , a_2 are lattice constants of strain-free GaN and $Al_{0.27}Ga_{0.73}N$ in c -plane, respectively. C_{ij} is elastic constant of $Al_{0.27}Ga_{0.73}N$. These parameters are also listed in Table 2. The stress due to LMM between AlGaN and GaN is 3.272 GPa. The total stress in AlGaN which is the sum of σ_{thermal} and σ_{LMM} with varying temperature is also shown in Figure 5.

TABLE 2: Parameters used in theoretical calculation.

Material	C_{11} (GPa)	C_{12} (GPa)	C_{13} (GPa)	C_{33} (GPa)	Y (GPa)	t (μm)	a (\AA)
GaN ^a	390	145	106	398	478.5	2	3.206
AlN ^b	410	149	99	389	508.6		3.131
$\text{Al}_{0.27}\text{Ga}_{0.73}\text{N}$	395.5	146	104	395.6	486.7	0.025	3.1858
sapphire	496	164	115	498	606.9	800	

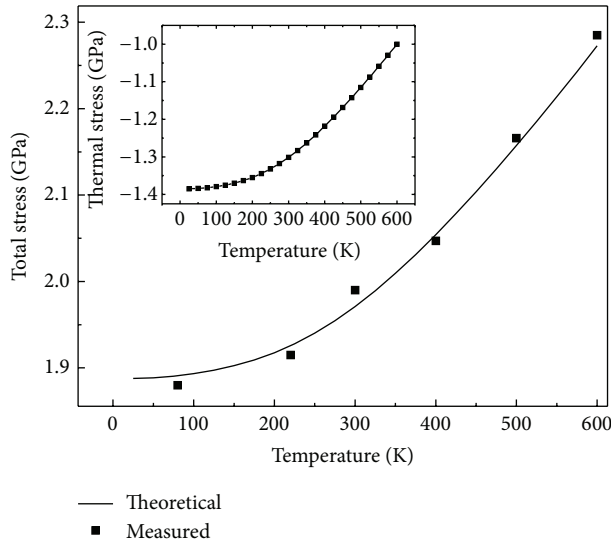
^aPolian et al. [17].^bMcNeil et al. [18].

FIGURE 5: Temperature-dependent stress in AlGaN barrier layer determined by Raman scattering and theoretical calculation. The inset shows the temperature dependence of thermal stress in AlGaN.

The total stress increases from 1.89 GPa at 80 K to 2.27 GPa at 600 K, which is consistent with the result obtained from near-resonant Raman scattering.

4. Conclusions

The temperature-dependent stress state in the AlGaN barrier layer of AlGaN/GaN heterostructure was investigated by UV near-resonant Raman scattering. Strong scattering peak resulting from the $A_1(\text{LO})$ phonon mode of AlGaN is observed under near-resonance condition. The temperature-dependent stress in the AlGaN layer determined by the resonance Raman spectra is consistent with the theoretical calculation result. This good agreement indicates that the UV near-resonant Raman scattering can be a direct and effective method to characterize the stress state in thin AlGaN barrier layer of AlGaN/GaN HEMT heterostructures.

Conflict of Interests

The authors declare that there is no conflict of interests regarding the publication of this paper.

Acknowledgments

This work was supported by the National 973 Project, China (2012CB619306, 2011CB301900), NSFC (nos. 61274075 and 61474060), NSF of Jiangsu Province, China (BK2011010), and Ph.D. Programs Foundation of Ministry of Education of China (20110091110032).

References

- [1] U. K. Mishra, P. Parikh, and Y.-F. Wu, "AlGaN/GaN HEMTs—an overview of device operation and applications," *Proceedings of the IEEE*, vol. 90, no. 6, pp. 1022–1031, 2002.
- [2] M. A. Khan, Q. Chen, J. W. Yang, M. S. Shur, B. T. Dermott, and J. A. Higgins, "Microwave operation of GaN/AlGaN-doped channel heterostructure field effect transistors," *IEEE Electron Device Letters*, vol. 17, no. 7, pp. 325–327, 1996.
- [3] Y.-F. Wu, A. Saxler, M. Moore et al., "30-W/mm GaN HEMTs by Field Plate Optimization," *IEEE Electron Device Letters*, vol. 25, no. 3, pp. 117–119, 2004.
- [4] Y. Dora, A. Chakraborty, L. McCarthy, S. Keller, S. P. Denbaars, and U. K. Mishra, "High breakdown voltage achieved on AlGaN/GaN HEMTs with integrated slant field plates," *IEEE Electron Device Letters*, vol. 27, no. 9, pp. 713–715, 2006.
- [5] X.-D. Wang, W.-D. Hu, X.-S. Chen, and W. Lu, "The study of self-heating and hot-electron effects for AlGaN/GaN double-channel HEMTs," *IEEE Transactions on Electron Devices*, vol. 59, no. 5, pp. 1393–1401, 2012.
- [6] N. Maeda, K. Tsubaki, T. Saitoh, and N. Kobayashi, "High-temperature electron transport properties in AlGaN/GaN heterostructures," *Applied Physics Letters*, vol. 79, no. 11, pp. 1634–1636, 2001.
- [7] R. Gaska, Q. Chen, J. Yang, A. Osinsky, M. A. Khan, and M. S. Shur, "High-temperature performance of AlGaN/GaN HFET's on SiC substrates," *IEEE Electron Device Letters*, vol. 18, no. 10, pp. 492–494, 1997.
- [8] T. Egawa, H. Ishikawa, M. Umeno, and T. Jimbo, "Recessed gate AlGaN/GaN modulation-doped field-effect transistors on sapphire," *Applied Physics Letters*, vol. 76, no. 1, pp. 121–123, 2000.
- [9] O. Ambacher, J. Smart, J. R. Shealy et al., "Two-dimensional electron gases induced by spontaneous and piezoelectric polarization charges in N- And Ga-face AlGaN/GaN heterostructures," *Journal of Applied Physics*, vol. 85, no. 6, pp. 3222–3233, 1999.
- [10] W. D. Hu, X. S. Chen, Z. J. Quan, C. S. Xia, W. Lu, and P. D. Ye, "Self-heating simulation of GaN-based metal-oxide-semiconductor high-electron-mobility transistors including hot electron and quantum effects," *Journal of Applied Physics*, vol. 100, no. 7, Article ID 074501, 2006.

- [11] N. Guo, W.-D. Hu, X.-S. Chen, L. Wang, and W. Lu, "Enhanced plasmonic resonant excitation in a grating gated field-effect transistor with supplemental gates," *Optics Express*, vol. 21, no. 2, pp. 1606–1614, 2013.
- [12] M. K. Öztürk, H. Altuntaş, S. Çörekçi, Y. Hongbo, S. Özçelik, and E. Özbay, "Strain-stress analysis of AlGaN/GaN heterostructures with and without an AlN buffer and interlayer," *Strain*, vol. 47, no. 2, pp. 19–27, 2011.
- [13] D. Chen, B. Shen, K. Zhang et al., "High-temperature characteristics of strain in AlGaN/GaN heterostructures," *Japanese Journal of Applied Physics*, vol. 45, no. 1, pp. 18–20, 2006.
- [14] M. Kuball, S. Rajasingam, A. Sarua et al., "Measurement of temperature distribution in multifinger AlGaN/GaN heterostructure field-effect transistors using micro-Raman spectroscopy," *Applied Physics Letters*, vol. 82, no. 1, pp. 124–126, 2003.
- [15] R. J. T. Simms, J. W. Pomeroy, M. J. Uren, T. Martin, and M. Kuball, "Channel temperature determination in high-power AlGaN/GaN HFETs using electrical methods and Raman spectroscopy," *IEEE Transactions on Electron Devices*, vol. 55, no. 2, pp. 478–482, 2008.
- [16] R. R. Reeber and K. Wang, "Lattice parameters and thermal expansion of important semiconductors and their substrates," *MRS Proceedings*, vol. 622, Article ID T6.35, 2000.
- [17] A. Polian, M. Grimsditch, and I. Grzegory, "Elastic constants of gallium nitride," *Journal of Applied Physics*, vol. 79, no. 6, pp. 3343–3344, 1996.
- [18] L. E. McNeil, M. Grimsditch, and R. H. French, "Vibrational spectroscopy of aluminum nitride," *Journal of the American Ceramic Society*, vol. 76, no. 5, pp. 1132–1136, 1993.
- [19] D. J. Chen, B. Shen, X. L. Wu et al., "Temperature characterization of Raman scattering in an AlGaN/GaN heterostructure," *Applied Physics A*, vol. 80, no. 8, pp. 1729–1731, 2005.
- [20] M. Kuball, "Raman spectroscopy of GaN, AlGaN and AlN for process and growth monitoring/control," *Surface and Interface Analysis*, vol. 31, no. 10, pp. 987–999, 2001.
- [21] G. Irmer, M. Wenzel, and J. Monecke, "The temperature dependence of the LO(Γ) and TO(Γ) phonons in GaAs and InP," *Physica Status Solidi (b)*, vol. 195, no. 1, pp. 85–95, 1996.
- [22] J. Menéndez and M. Cardona, "Temperature dependence of the first-order Raman scattering by phonons in Si, Ge, and -Sn: anharmonic effects," *Physical Review B*, vol. 29, no. 4, pp. 2051–2059, 1984.
- [23] M. Balkanski, R. F. Wallis, and E. Haro, "Anharmonic effects in light scattering due to optical phonons in silicon," *Physical Review B*, vol. 28, no. 4, pp. 1928–1934, 1983.
- [24] J.-M. Wagner and F. Bechstedt, "Phonon deformation potentials of α -GaN and -AlN: an *ab initio* calculation," *Applied Physics Letters*, vol. 77, no. 3, pp. 346–348, 2000.
- [25] C. H. Hsueh, "Thermal stresses in elastic multilayer systems," *Thin Solid Films*, vol. 418, no. 2, pp. 182–188, 2002.
- [26] C. H. Hsueh and A. G. Evans, "Residual stresses in metal/ceramic bonded strips," *Journal of the American Ceramic Society*, vol. 68, no. 5, pp. 241–248, 1985.

Research Article

Photoresponse of Long-Wavelength AlGaAs/GaAs Quantum Cascade Detectors

Liang Li¹ and Dayuan Xiong^{1,2}

¹Key Laboratory of Polar Materials and Devices, Ministry of Education, East China Normal University, Shanghai 200241, China

²Shanghai Key Laboratory of Multidimensional Information Processing, East China Normal University, Shanghai 200241, China

Correspondence should be addressed to Dayuan Xiong; dyxiong@ee.ecnu.edu.cn

Received 27 November 2014; Accepted 4 January 2015

Academic Editor: Wen Lei

Copyright © 2015 L. Li and D. Xiong. This is an open access article distributed under the Creative Commons Attribution License, which permits unrestricted use, distribution, and reproduction in any medium, provided the original work is properly cited.

We study the photoresponse and photocurrents of long-wavelength infrared quantum cascade detectors (QCDs) based on AlGaAs/GaAs material system. The photocurrent spectra were measured at different temperatures from 20 K to 100 K with a low noise Fourier transforming infrared spectrometer. The main response peak appeared at $8.9\text{ }\mu\text{m}$ while four additional response peaks from $4.5\text{ }\mu\text{m}$ to $10.1\text{ }\mu\text{m}$ were observed as well. We confirmed that the photocurrent comes from phonon assisted tunneling and the multipeak behavior comes from the complicated optical transition in the quantum cascade structure. This work is valuable for the future design and optimization of QCD devices.

1. Introduction

Quantum cascade detectors (QCDs) are photovoltaic detectors. They can operate under zero bias applied and consequently do not suffer any dark current which is expected as a promising alternative of quantum well infrared photodetectors (QWIPs) [1, 2]. For focal plane array (FPA) application, the QCDs perform pure photoresponse current to reach a longer integration time [3] and lower noise equivalent temperature difference (NETD) [4]. Based on bound-to-bound intraband transition, the line width of QCDs is narrow, which means high selectivity to wavelength. Moreover, QCDs have been shown to work at higher temperature [5] and been reported in different materials and all infrared atmospheric windows [5–9].

To prevent false-alarm and improve detection accuracy, two color FPAs were studied and fabricated [10–12]. Conventionally, two-color detection is achieved by two single-color detectors fabricated together. So, secondary photoresponse peaks are undesired which would act as cross talk and noise in response spectra. QCDs perform excellent for the narrowband detection. But confined with their multisized quantum wells, the photoexcited transitions are complicated. As a result, several secondary peaks appear. To eliminate cross

talk and further improve the detector's performance, detailed study on the secondary peaks is of particularly importance.

2. Materials and Methods

The samples under study are GaAs/AlGaAs QCDs designed to operate at $8.9\text{ }\mu\text{m}$ [3, 13]. The wafer used to fabricate this QCD sample was grown by molecular beam epitaxy (MBE), and the layer sequence from substrate to top was 400 nm n-doped GaAs bottom contact (Si-doped to $1 \times 10^{18}\text{ cm}^{-3}$), 40 periods of 7 coupled $\text{Al}_{0.33}\text{Ga}_{0.67}\text{As}/\text{GaAs}$ superlattice active region, and 350 nm n-doped GaAs top contact in which doping concentration is equal to the bottom contact. The first QW of each period absorbs incident light and is n-doped with the doping concentration $5 \times 10^{17}\text{ cm}^{-3}$. The thickness of different QWs and barriers is $68/56.5/20/39.55/23/31/28/31/34/31/38/31/48/22.6\text{ }(\text{\AA})$ in roman and bold, respectively. The mesa size is $200 \times 200\text{ }\mu\text{m}^2$ and electrical contacts were formed by a standard lift-off deposition of AuGe/Ni/Au (100/20/400 nm). To theoretically describe the electronic properties of QCDs, we applied the standard eight-band $k \cdot p$ model. As shown in Figure 1, the electrons which the energy $h\nu = E_8 - E_1$ could be excited from E_1 to E_8 . E_7 is designed to equal E_8 which

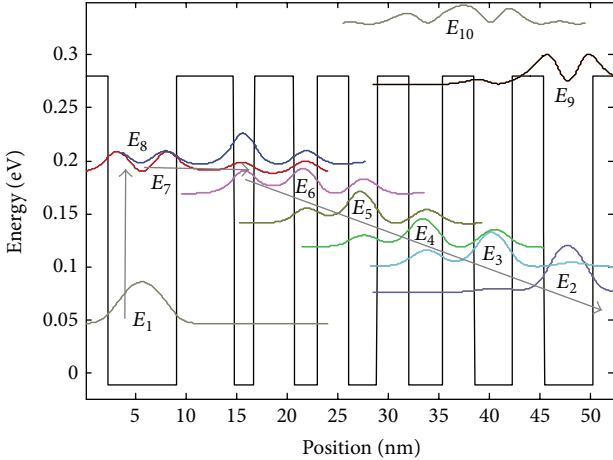


FIGURE 1: Self-consisted calculated conduction band structure of one period.

could allow the excited electrons resonant tunneling to reduce the recombination possibility and contribute to effective transport. Then, excited electrons tended to transport in the direction $E_7 \rightarrow E_6 \rightarrow E_5 \rightarrow E_4 \rightarrow E_3 \rightarrow E_2 \rightarrow E_{1,\text{next-period}}$ by LO-phonon assisted tunneling due to the coupling of wavefunction of adjacent wells.

3. Results and Discussion

Considering the complicated interactions between the inter-subbands in QCDs, the absorption and response spectrum is not so pure and sensitive to $8.9\mu\text{m}$ only. With the diffusion and tunneling of electrons, more than one absorption process could be figured out theoretically as Figure 2(a) dashed line indicated. Besides, we measured response photocurrent spectra under zero bias voltage at different temperature. QCD sample is soldered on a copper heat sink and placed in a closed cycle helium cryostat. The measurements were performed by using a SR570 low noise current preamplifier and a Fourier transform infrared spectrometer (Nicolet 6700). Response photocurrent spectra at different temperatures are shown as solid lines in Figure 2(a).

Three clear photoresponse peaks were found immediately in Figure 2(a) which are $E_1 \rightarrow E_7/E_8$, $E_2 \rightarrow E_8$, and $E_1 \rightarrow E_9$ processes. Other two peaks could be seen after zooming in which are corresponding to $E_2 \rightarrow E_9$ and $E_2 \rightarrow E_{10}$ transitions. It is to be noticed that the valley at 1250 cm^{-1} is a background absorption so that the peak at 1270 cm^{-1} is actually a fake one.

To further improve the detector's performance, detailed study on the formation of multiphoton spectra is needed. As is known, photocurrent I_p could be expressed as [14]

$$I_p = n_p ev, \quad (1)$$

where n_p is the quantity of photogenerated carriers, e is electron charge, and v is the transport velocity. Moreover, for a certain wavelength λ , the photocurrent could be given by

$$I_p(\lambda) = n_p(\lambda) ev(\lambda). \quad (2)$$

Equations (1) and (2) are true when the electron concentration is high enough to be photoexcited. Otherwise, the I_p is also restricted to electron concentration. Besides, corresponding to different photoexcited transitions, the transport paths are not all the same in QCDs, which would lead to different $v(\lambda)$. At low temperature condition, the impurities are ionized less and mainly distributed in E_1 subband. Thus the optical excited transitions primarily occur from E_1 to E_7 , E_8 , and E_9 , respectively. With temperature rises, more impurities will be ionized and electron concentration will get higher. Consequently, more quantum states of E_1 subband would be occupied. According to Pauli exclusion principle and Hund's rules, electrons would tend to be distributed at higher energy levels such as E_2 by means of diffusion and tunneling. Then, optical transition from E_2 is enhanced as Figures 2(b) and 2(c) indicated.

The calculated electrons distribution at different temperatures is presented in Figure 3. It can be seen that electron density at E_2 subband is hard to be identified at 50 K, while the density at E_2 or even other subbands becomes larger with temperature increases. At temperature higher than 40 K, the electron density grows exponentially rapidly as the inset Figure 3 indicated, and corresponding to Figure 2(b), the response of $E_2 \rightarrow E_8$ transition becomes clear at 40 K. This indicated that our QCD can be operated around 80 K, but the electron concentration of E_2 grows to ten times as that at 40 K which would be a nonignorable cross talk.

In addition, band-gap and barrier height would be influenced by temperature. Energy levels would be rearranged by structure variation of quantum wells, especially the quasibound energy levels such as E_9 . As for photoconductive QWIPs working at nonzero applied bias, the bound-to-quasibound transition appears redshift with temperature rises [15]. But for QCDs, null bias working condition makes the transport mechanisms different. As is expected, $E_1 \rightarrow E_9$ transition appears blueshift with temperature getting higher as Figure 2(d) indicated. The experiment results and calculated energy gap between E_1 and E_9 are shown in Figure 4. A general agreement has been obtained.

From responsivity and dark current, we can deduce the Johnson noise limited detectivity given by [2]

$$D^* = R(\lambda) \sqrt{\frac{R_0 A}{4kT}}, \quad (3)$$

where $R(\lambda)$ is the peak responsivity, R_0 is the device resistance at null bias, A is the mesa surface, and T is the temperature of the sample. We obtained $D^*(\lambda = 8.9) = 1.4 \times 10^{10}$ Jones at 80 K as Figure 5 presented. Moreover, after the elimination of secondary response peaks, the g factor in spectra would get higher, leading to a higher D^* .

In our QCD detector samples, the $E_1 \rightarrow E_7$ and $E_1 \rightarrow E_8$ transitions are expected to be the primary optical transitions. The spectra noises which act as cross talk could be classified in two categories. The first category is the transitions from E_1 to non- E_7/E_8 subbands such as $E_1 \rightarrow E_9$ and the second is excited from non- E_1 (for example, $E_2 \rightarrow E_8$) energy levels. For the first category, thicker barriers would reduce the overlap of wavefunctions, leading to a lower transition

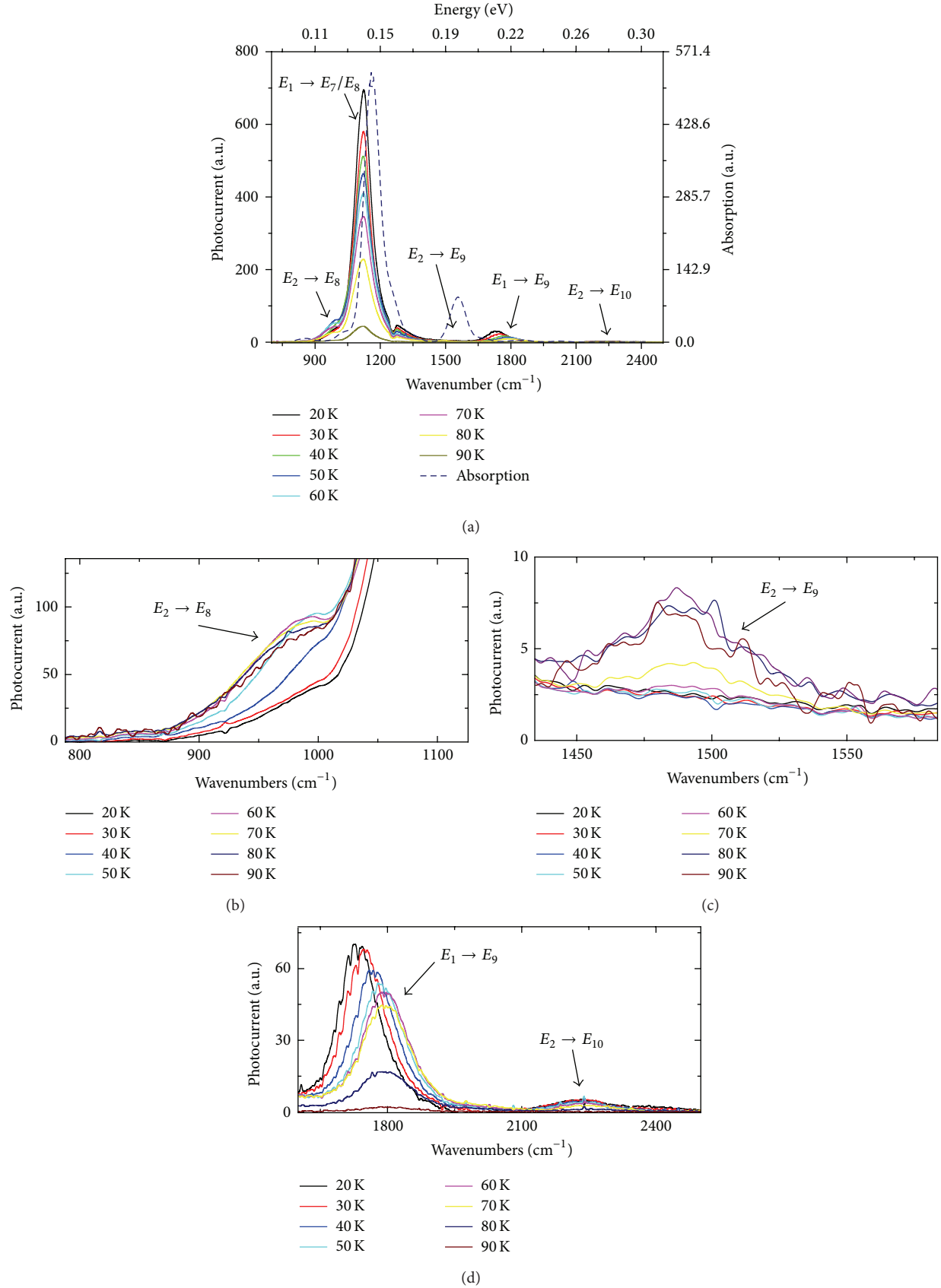


FIGURE 2: (a) Calculated absorption spectra at 300 K (dashed line) and measured photoresponse spectra (solid line). (b) Details (normalized) around $E_2 \rightarrow E_8$. (c) Details (normalized) around $E_2 \rightarrow E_9$. (d) Details around $E_1 \rightarrow E_9$ and $E_2 \rightarrow E_{10}$.

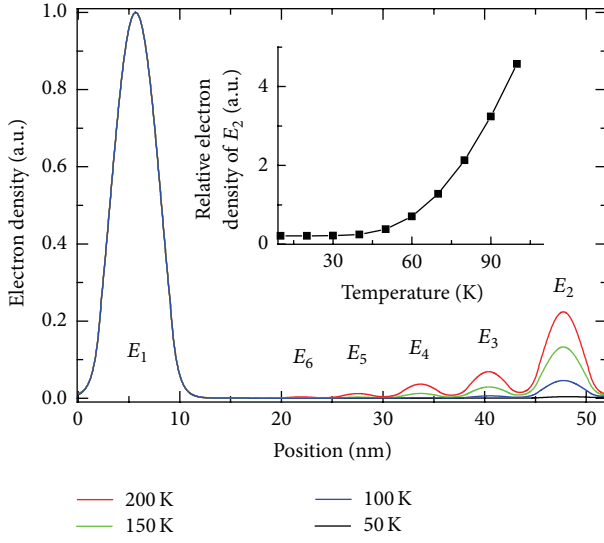


FIGURE 3: Calculated electron density at different temperatures (normalized). Inset is the electron concentration ratio of E_2 and E_1 subband.

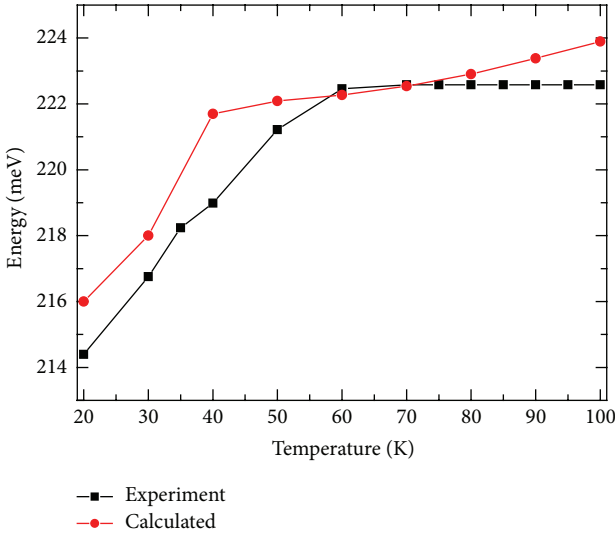


FIGURE 4: Calculated and experiment $E_1 \rightarrow E_g$ transition peak energy.

rate. For the second category, an effective way is to reduce the electron occupation of ground states at non- E_1 subbands.

4. Conclusion

In conclusion, we have demonstrated a GaAs/AlGaAs multipeak quantum cascade detector. The main response peak appeared at $8.9\text{ }\mu\text{m}$ while four other response peaks from $4.5\text{ }\mu\text{m}$ to $10.1\text{ }\mu\text{m}$ were observed and analyzed. We confirmed that the multipeak performance comes from the complicated optical transition in the quantum cascade structure. This work is valuable for the design and optimization of QCD devices.

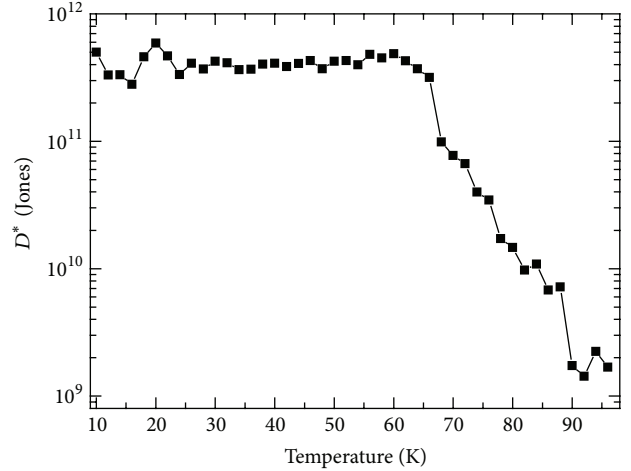


FIGURE 5: Peak wavelength detectivity.

Conflict of Interests

The authors declare that there is no conflict of interests regarding the publication of this paper.

Acknowledgments

This work was supported by the National Nature Science Foundation of China (Grant no. 61106092) and the State Key Development Program for Basic Research of China (Grants no. 2013CB632802).

References

- [1] L. Gendron, C. Koeniguer, X. Marcadet et al., "Quantum cascade detection," in *Electro-Optical and Infrared Systems: Technology and Applications*, vol. 5612 of *Proceedings of SPIE*, 63, December 2004.
- [2] Q. Li, Z. F. Li, N. Li et al., "High-polarization-discriminating infrared detection using a single quantum well sandwiched in plasmonic micro-cavity," *Scientific Reports*, vol. 4, article 6332, 2014.
- [3] L. Gendron, C. Koeniguer, V. Berger, and X. Marcadet, "High resistance narrow band quantum cascade photodetectors," *Applied Physics Letters*, vol. 86, no. 12, Article ID 121116, 2005.
- [4] A. Delga, L. Doyennette, V. Berger, M. Carras, V. Trinité, and A. Nedelcu, "Performances of quantum cascade detectors," *Infrared Physics and Technology*, vol. 59, pp. 100–107, 2013.
- [5] D. Hofstetter, M. Graf, T. Aellen, J. Faist, L. Hvozdara, and S. Blaser, "23 GHz operation of a room temperature photovoltaic quantum cascade detector at $5.35\text{ }\mu\text{m}$," *Applied Physics Letters*, vol. 89, no. 6, Article ID 061119, 2006.
- [6] S.-Q. Zhai, J.-Q. Liu, X.-J. Wang et al., "19 μm quantum cascade infrared photodetectors," *Applied Physics Letters*, vol. 102, no. 19, Article ID 191120, 2013.
- [7] S. Q. Zhai, J. Q. Liu, N. Kong et al., "Strain-compensated InP-based InGaAsInAlAs quantum cascade infrared detectors for $3\text{--}5\text{ }\mu\text{m}$ atmospheric window," in *International Symposium on Photoelectronic Detection and Imaging 2011: Advances in Infrared Imaging and Applications*, vol. 8193 of *Proceedings of SPIE*, Beijing, China, September 2011.

- [8] L. Gendron, C. Koeniguer, X. Marcadet, and V. Berger, "Quantum cascade detectors," *Infrared Physics and Technology*, vol. 47, no. 1-2, pp. 175–181, 2005.
- [9] S. Sakr, P. Crozat, D. Gacemi et al., "GaN/AlGaN waveguide quantum cascade photodetectors at lambda approximate to 1.55 μm with enhanced responsivity and similar to 40 GHz frequency bandwidth," *Applied Physics Letters*, vol. 102, Article ID 011135, 2013.
- [10] E. Bellotti and D. D'Orsogna, "Numerical analysis of HgCdTe simultaneous two-color photovoltaic infrared detectors," *IEEE Journal of Quantum Electronics*, vol. 42, no. 4, pp. 418–426, 2006.
- [11] W.-D. Hu, X.-S. Chen, Z.-H. Ye, and W. Lu, "An improvement on short-wavelength photoresponse for a heterostructure HgCdTe two-color infrared detector," *Semiconductor Science and Technology*, vol. 25, no. 4, Article ID 045028, 2010.
- [12] W. D. Hu, Z. H. Ye, L. Liao et al., "128 \times 128 long-wavelength/mid-wavelength two-color HgCdTe infrared focal plane array detector with ultralow spectral cross talk," *Optics Letters*, vol. 39, no. 17, pp. 5184–5187, 2014.
- [13] J. Liu, N. Kong, L. Li et al., "High resistance AlGaAs/GaAs quantum cascade detectors grown by solid source molecular beam epitaxy operating above liquid nitrogen temperature," *Semiconductor Science and Technology*, vol. 25, no. 7, Article ID 075011, 2010.
- [14] B. F. Levine, "Quantum-well infrared photodetectors," *Journal of Applied Physics*, vol. 74, no. 8, p. R1, 1993.
- [15] X. H. Liu, X. H. Zhou, N. Li et al., "Effects of bias and temperature on the intersubband absorption in very long wavelength GaAs/AlGaAs quantum well infrared photodetectors," *Journal of Applied Physics*, vol. 115, no. 12, Article ID 124503, 2014.

Research Article

Influence of Codoping on the Optical Properties of ZnO Thin Films Synthesized on Glass Substrate by Chemical Bath Deposition Method

G. Shanmuganathan and I. B. Shameem Banu

Department of Physics, B.S.Abdur Rahman University, Chennai 600048, India

Correspondence should be addressed to G. Shanmuganathan; shan25@bsauniv.ac.in

Received 18 June 2014; Accepted 5 August 2014; Published 31 August 2014

Academic Editor: Weida Hu

Copyright © 2014 G. Shanmuganathan and I. B. S. Banu. This is an open access article distributed under the Creative Commons Attribution License, which permits unrestricted use, distribution, and reproduction in any medium, provided the original work is properly cited.

Fe and K simultaneously doped ZnO thin films $Zn_{0.99}K_{0.01}(Fe)_xO$ ($x = 1, 2, 3$, and 4%) were synthesized by chemical bath deposition method. The XRD investigation reveals that all the doped ZnO thin films are in hexagonal wurtzite crystal structure without impurity phases. With increase in Fe concentration, the growth of thin films along c axis is evident from the XRD which indicates the increase in intensity along (002) direction. The same is visible from the surface morphology which shows the formation of hexagonal structure for higher Fe concentration. The topography shows gradual variation with Fe incorporation. The optical energy band gap obtained from the transmittance spectrum decreases from 3.42 to 3.06 eV with increase in Fe concentration indicating the red shift and this trend is consistent with the earlier experimental results. The UV emission is centered around 3.59 eV. The optical constants such as refractive index, extinction coefficient, and absorption coefficient which are essential for the optoelectronic applications were also determined.

1. Introduction

Zinc oxide is an amazing material for numerous applications such as photodetectors, antireflecting coating, thin film solar cell, LEDs, and lithium-ion batteries [1–5] due to its wide band gap (3.445 eV) and high binding energy (60 eV) [1, 6]. Due to its unique optical, semiconductor, and optical properties, ZnO thin films have been extensively studied for various applications. Several methods such as chemical bath deposition, MOCVD, melt growth, ion implementation, DC reactive magnetron cosputtering, and hydrothermal and simple chemical pyrolysis have been used to synthesize ZnO thin films [7–13]. Of late, ZnO thin films are being fabricated by codoping for enhancing the efficiency of ZnO film in optoelectronic devices.

Alkali elements are well-known materials for tuning ZnO optical and electrical behaviors. Alkali doped ZnO films have been broadly investigated in recent decades. Kim et al. reported that, when K doped ZnO thin films were synthesized on Al_2O_3 (001), the optical properties were improved [14].

Xu et al. also reported that the optical emission was emerged while K doped ZnO was annealed during different temperatures [15]. Depending on the different types of substrates such as Si (111), ZnO exhibited different emissions such as green and yellow emissions at 529–567 nm and 600–640 nm due to oxygen vacancy and oxygen interstitials, respectively [16]. For Na-doped ZnO, the carrier mobility was $2.1 \text{ cm}^2 \text{ V}^{-1} \text{ s}^{-1}$ and structural and optical properties were reported elsewhere [17, 18]. Li doped ZnO is also used for developing the ferroelectric, optical, and multiphonon properties of ZnO semiconductor [19, 20]. In latest decades, Fe doped ZnO has been synthesized for optical properties [21] because Fe is well-known optical emitter in doped ZnO. Zhang et al. reported [22] that the optical mechanism of ZnO alloyed with Fe ion. Not only optical properties but also Fe is well known as a doping element for altering the magnetic and electrical properties [23–25]. The extensive literature survey shows that only few works were reported on the optical properties of dual doped ZnO films. Some experimental works such as Al-K [26], Li-N [27], Li-Mg [28], Fe-Co [29], and Fe-N [30]

reported the dual doped ZnO to investigate the optical and magnetic properties. However, the combination of alkali and transition metals (TM) dual doped ZnO is rarely reported.

As per the literature till date the study on the optical properties of K and Fe doped ZnO thin films has not been reported yet. Both Fe and K when doped to ZnO separately, they modify the band gap and also the luminescence characteristics and hence, the Fe and K simultaneously doped to ZnO can bring out some interesting results and so in the present study, (K, Fe) codoped ZnO thin films were investigated for the influence on the optical properties. The optical properties of K doped ZnO films show that 1% of K exhibited better optical properties [31]. For further optical investigation, the transition metal Fe is added into ZnO:K (1%) due to its excellent optical emission property. The simple chemical bath deposition method is employed to fabricate these films. The influence of Fe concentration on the optical behavior has been revealed in the transmittance and photoluminescence sections. In the present work, 1% K doped ZnO would be indicated as ZnO:K (1%). The main purpose of this study is to examine the effect of Fe ion concentration on optical properties of ZnO:K (1%) films.

2. Experimental Work

Codoped (K, Fe) ZnO films were synthesized by chemical bath deposition method. Here, ZnCl_2 (AR MERCK), KOH (AR MERCK), KCH_3COO (AR MERCK), and $\text{FeSO}_4 \cdot 7\text{H}_2\text{O}$ (AR MERCK) were the precursor materials and doping source materials, respectively. Initially, ZnCl_2 and KOH were dissolved in the triple distilled water with 1:1 ratio and stirred using magnetic stirrer at 60°C for 10 minutes. Then one percentage of potassium acetate was added in 1:1 ratio prepared homogeneous solution. After that, different percentages of Fe (1 at %, 2 at %, 3 at %, and 4 at %) were added to the solution for doping. In the synthesized homogenous solution, HCl is added to keep the pH at 8. The solution was cooled to room temperature and microglass slide was used as substrate. The substrate was cleaned by HCl, acetone, and double distilled water. Then the cleaned substrate was immersed vertically in the solution using substrate holder. Finally, the solution was steadily stirred by magnetic stirrer to get the uniformly coating on the substrate. After 45 minutes of deposition, the uniform coated substrates were taken out from the solutions and cleaned with double distilled water and then dried in air. Finally, thin films are kept in the furnace and calcined at 400°C for 1 hour.

3. Results and Discussion

3.1. Structural Analysis. The XRD pattern of codoped (K, Fe) ZnO thin films is shown in Figure 1. All the thin films exhibit hexagonal crystal phase and it is confirmed with standard JCPDS card (PDF numbers 891397 and 890510) number. In XRD pattern, the three prominent peaks such as (100), (002), and (101) were obtained for all films without any secondary phase. In our previous report, three prominent peaks such as (100), (002), and (101) were observed for ZnO:K (1%)

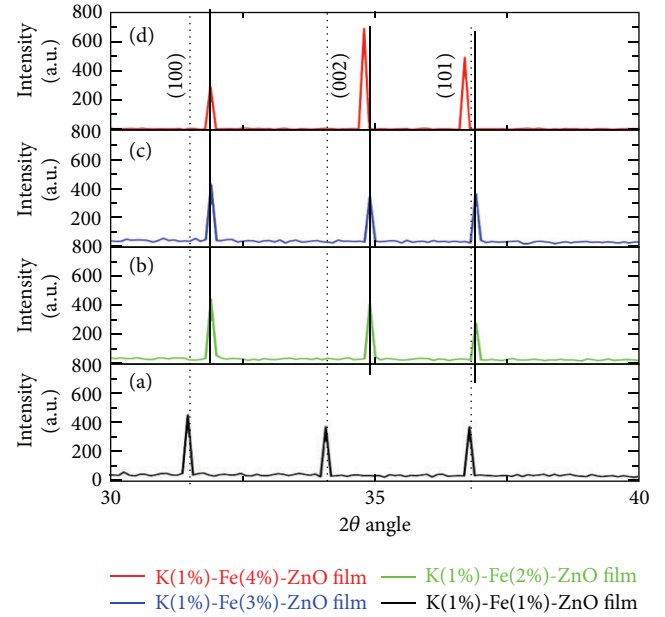


FIGURE 1: XRD pattern of (K (1%), Fe) codoped ZnO for Fe concentrations: (a) 1%, (b) 2%, (c) 3%, and (d) 4%.

thin film [31]. In the present work, when Fe concentration is increased, the crystal properties of the codoped ZnO thin films have changed. The low intensity peak was observed for ZnO:K (1%) [31]. However, in the present work, it is observed that when Fe is introduced, the intensity of three prominent peaks has changed. The variation in intensity indicates the incorporation of Fe ions in the lattice of ZnO site. In the doping process, the three prominent peaks are shifted from higher to lower angles due to the different ionic radius of Fe such as Fe^{3+} and Fe^{2+} . For 2, 3, and 4% of Fe, the three prominent peaks shifted to higher angle than 1% Fe due to the inclusion of Fe^{3+} (0.068 nm) [11, 32]. For 4% Fe, the (002) peak shifts to lower angle due to the high ionic radius (0.078) of Fe^{2+} [33, 34]. In the entire XRD pattern, the intensity of (002) plane varied for different Fe ion concentrations which indicates that the film is grown along *c*-axis. In the XRD pattern, the high intensity of (002) plane reveals the improved crystallinity [35]. The full width at half maximum of (002) peaks is significantly varied with various Fe concentrations. For 4% Fe, the FWHM is lower than others. Saha et al. reported that the low FWHM reveals the deterioration of the crystallinity [36]. For the codoped ZnO film, average crystal size and average crystal strain were calculated and are summarized in Table 1.

The crystalline sizes of thin films are calculated using Scherrer formula:

$$D = \frac{0.9\lambda}{\beta \cos \theta} \quad (1)$$

3.2. Surface Morphology Analysis and EDAX Spectrum. Figure 2 shows the surface morphology of (K, Fe) codoped ZnO films investigated by field emission scanning electron

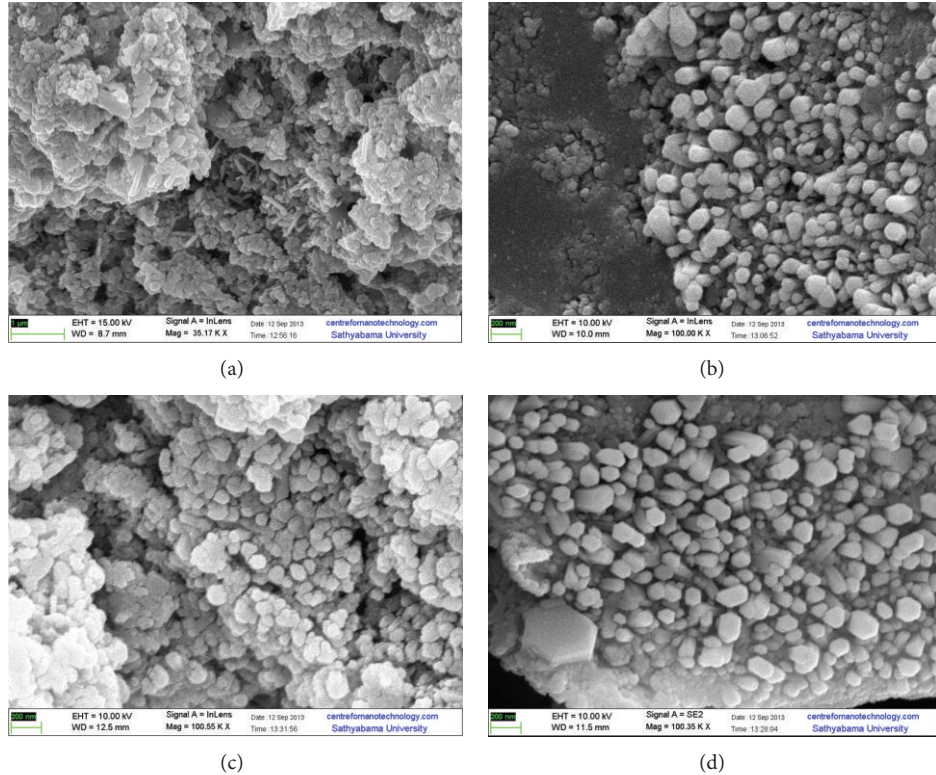


FIGURE 2: Surface morphology (FESEM) of (K (1%), Fe) codoped ZnO for Fe concentrations: (a) 1%, (b) 2%, (c) 3%, and (d) 4%.

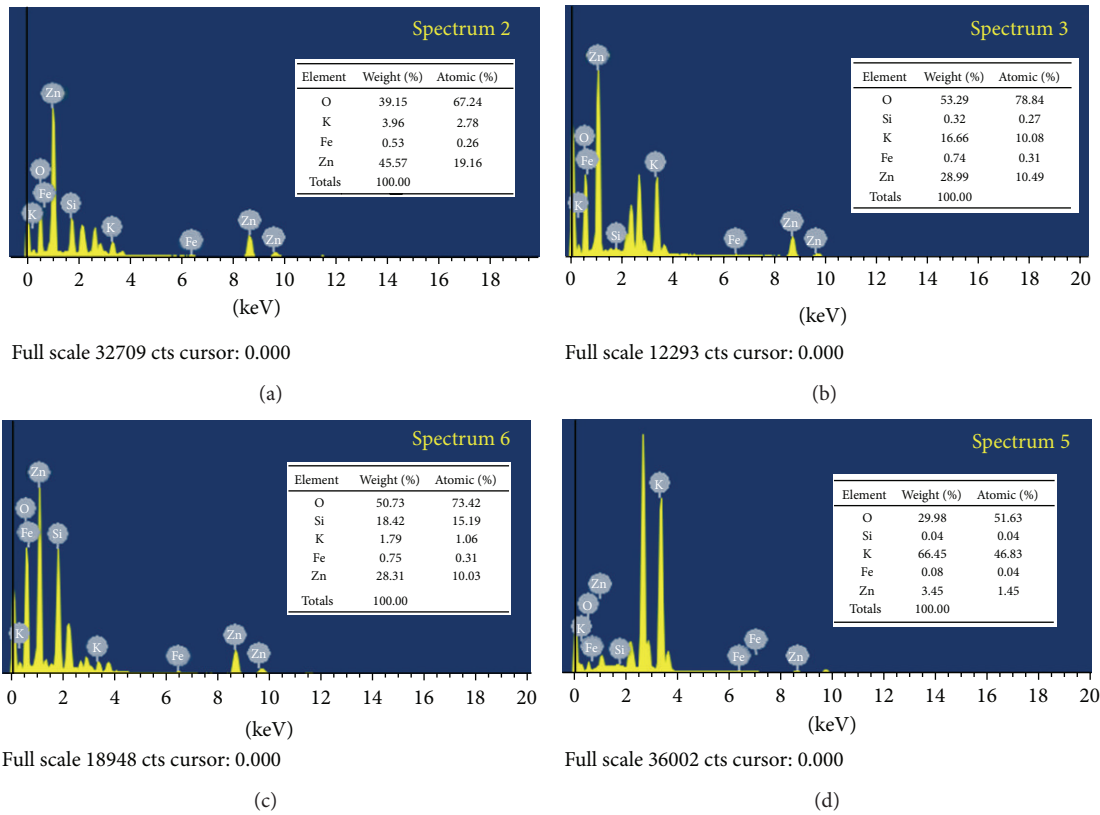


FIGURE 3: EDAX spectrum of (K (1%), Fe) codoped ZnO for Fe concentrations: (a) 1%, (b) 2%, (c) 3%, and (d) 4%.

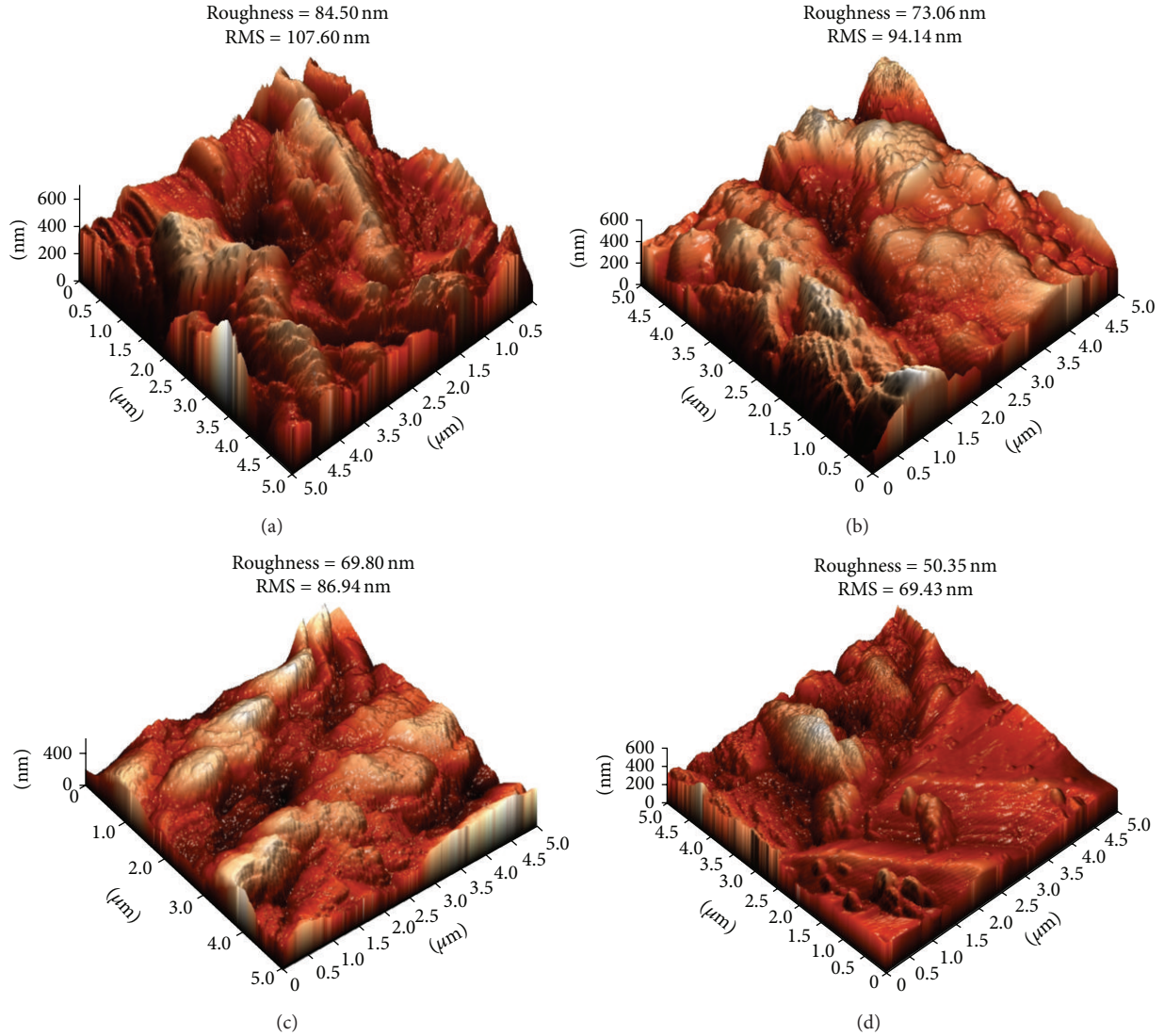


FIGURE 4: Atomic force microscope of (K (1%), Fe) codoped ZnO for Fe concentrations: (a) 1%, (b) 2%, (c) 3%, and (d) 4%.

microscope (SUPRA “55”). SEM image shows that morphology changes with Fe doping concentrations. The film exhibits small grains of varied size at different level of Fe. The element compositions such as Zn, O, K, and Fe were confirmed by energy dispersive analysis X-ray spectroscopy and are shown in Figure 3. In all EDAX spectrums, the substrate peak is presented between 2.4 and 2.5 eV [31].

3.3. Surface Topology. In Figure 4 three-dimensional (3D) surface topography of (K, Fe) codoped ZnO thin films is presented. Surface topography was scanned at $5 \times 5 \mu\text{m}$ in tapping mode. The average roughness and root mean square values were determined. The average roughness is 84.50 nm, 73.06 nm, 69.80 nm, and 50.35 nm at level 1, 2, 3, and 4% Fe, respectively. The RMS values are 107.60 nm, 94.14 nm, 86.94 nm, and 69.43 nm for 1, 2, 3, and 4% Fe, respectively. The decreases in average roughness and RMS show that the crystalline quality of the codoped ZnO thin films has been

improved by increase in Fe concentration. The low roughness indicates the enhancement of crystalline quality [37].

3.4. Transmittance Spectrum and Optical Band Gap. The transmittance spectrum of (K, Fe) codoped ZnO nanofilms is shown in Figure 5. The (K, Fe) codoped ZnO thin films exhibit a low transmittance as seen in Figure 5. In the visible region, the transmittance is 50%, 45%, 25%, and 10% for 1, 2, 3, and 4% Fe, respectively, and the transmittance is found to decrease with increase in Fe dopant concentration. The film thickness is one of the main factors for low transmittance. In the doping process, the film thickness is 4.348 μm , 4.690 μm , 5.078 μm , and 6.520 μm for 1, 2, 3, and 4% Fe, respectively. Xu et al. have reported that the optical transmittance obviously reduced in the visible region due to the Fe ion concentrations [38, 39]. Prajapati et al. have studied that the low transmittance was obtained for Fe doped ZnO thin films due to lattice defects into ZnO lattice [40].

TABLE 1: The peak position, FWHM, average crystalline size, lattice constant, and average lattice strain for the (K, Fe) codoped ZnO thin films.

Materials	Peak positions			FWHM of peaks			Average crystalline size (nm)	Lattice constant (nm)		Average crystalline strain (nm)
	(100)	(002)	(001)	(100)	(002)	(101)		<i>a</i>	<i>b</i>	
K (1%)-Fe (1%)-ZnO film	31.49	34.10	36.80	0.1088	0.1060	0.1076	77.39	0.3043	0.5270	0.0879
K (1%)-Fe (2%)-ZnO film	31.90	34.90	36.90	0.1105	0.1095	0.1081	76.47	0.2862	0.4957	0.0882
K (1%)-Fe (3%)-ZnO film	31.90	34.90	36.90	0.1102	0.1093	0.1088	76.08	0.3004	0.5203	0.0882
K (1%)-Fe (4%)-ZnO film	31.90	34.80	36.70	0.1014	0.1009	0.1002	82.55	0.3012	0.5217	0.0815

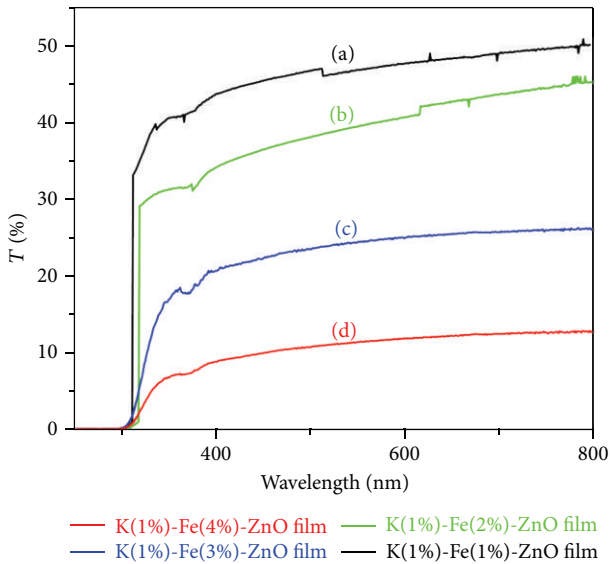


FIGURE 5: UV transmittance of (K (1%), Fe) codoped ZnO for Fe concentrations: (a) 1%, (b) 2%, (c) 3%, and (d) 4%.

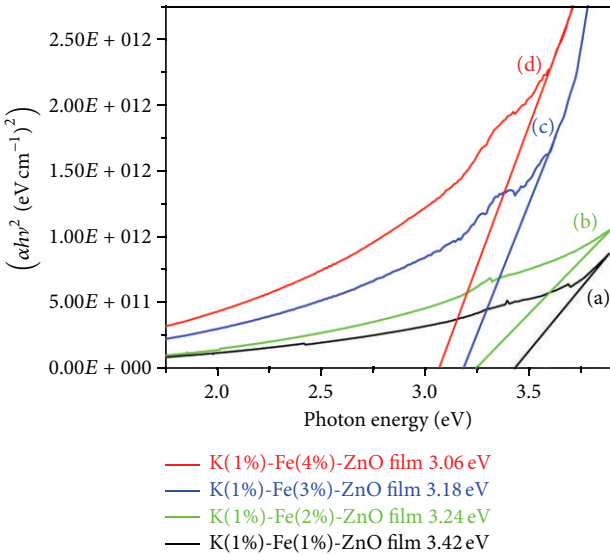


FIGURE 6: Optical band gap of (K (1%), Fe) codoped ZnO for Fe concentrations: (a) 1%, (b) 2%, (c) 3%, and (d) 4%.

Due to the film thickness, the incident light is much absorbed and so the transmittance light intensity is less pronounced. This fact is well reported by the absorption coefficient values of these thin films (Figure 9).

The optical band gap of codoped (K, Fe) nano-ZnO films is calculated from the following formula:

$$\alpha = \frac{1}{d} \ln \left(\frac{1}{T} \right), \quad (2)$$

$$(\alpha h\nu)^2 = A (h\nu - E_g),$$

where $h\nu$ is photon energy and E_g is energy gap. The optical band gaps of codoped ZnO films are shown in Figure 6. The optical energy gap can be obtained by extrapolating the linear part to x -axis. In our previous work, the band gap was 3.94 eV for ZnO:K (1%) film [31]. The energy gap reduces due to the increase in Fe doping concentration. The band gap values are 3.42 eV, 3.24 eV, 3.18 eV, and 3.06 eV for 1, 2, 3, and 4 at % Fe, respectively, thus indicating the red shift. C. S. Prajapati et al. reported that when Fe ion was doped with ZnO, the optical band gap changes [40]. However, Xu and Li reported that the band gap of ZnO was increased by Fe ion concentrations [38]. The red shift was also observed for ZnO thin films due to the high doping material, renormalization effect [41], and film thickness [21, 42]. Among the three factors, the change in the optical band gap also depends on the thickness of the thin film.

3.5. Optical Constants. The refractive index of codoped ZnO films is calculated from the following formula:

$$n = \left(\frac{1+R}{1-R} \right) + \sqrt{\left(\frac{4R}{(1-R)^2} \right) - k^2}, \quad (3)$$

$$k = \frac{\alpha\lambda}{4\pi}.$$

The refractive index of codoped ZnO thin films as function of wavelength is shown in Figure 7. The refractive index varies with variation in Fe concentrations. In the visible region the light is normally dispersed due to the contribution of virtual electronic transition [43] and lower dense medium. For the 375 nm, the refractive index of codoped ZnO thin film is 5.3, 3.2, 4.3, and 6.2 for 1, 2, 3, and 4% Fe, respectively. The thin

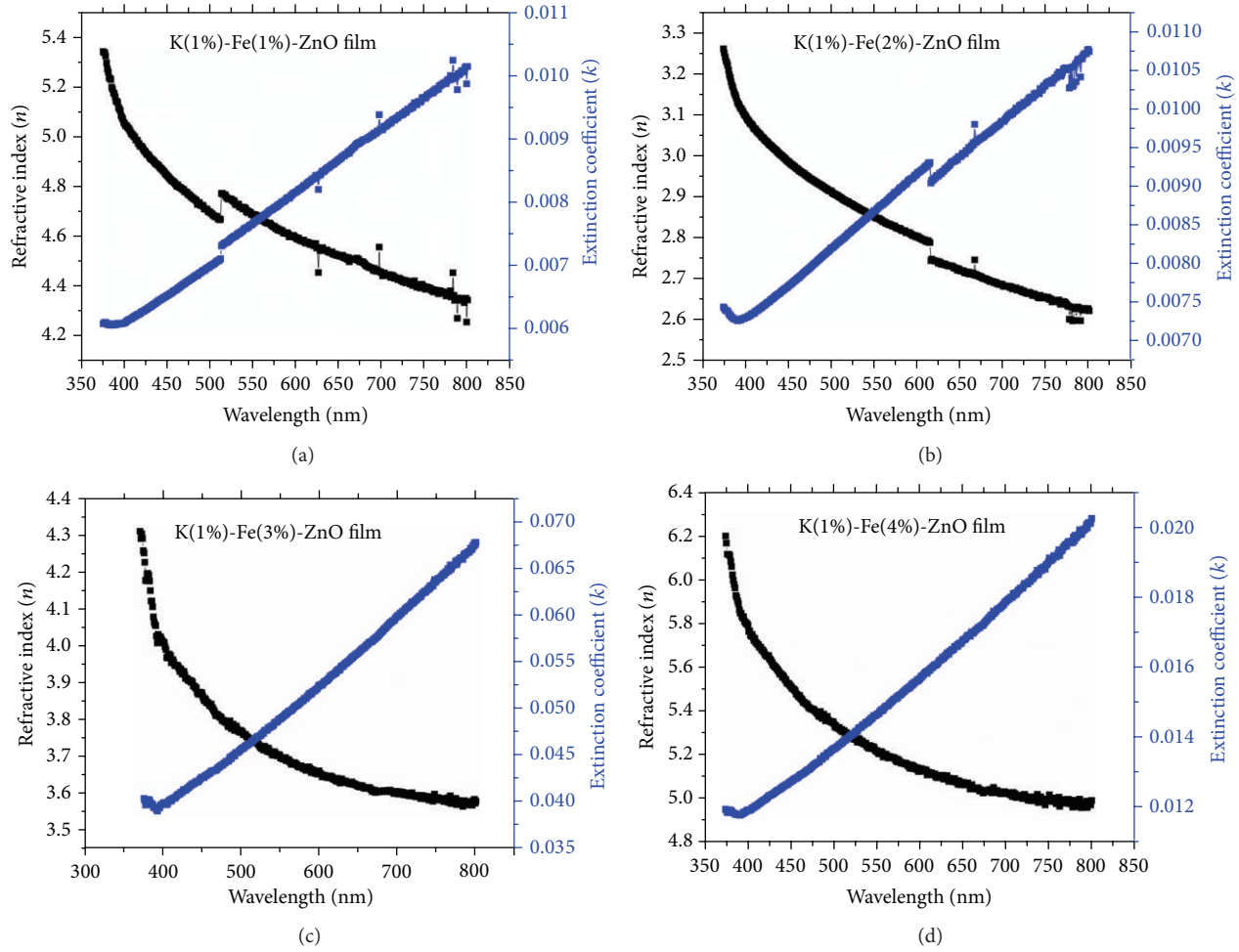


FIGURE 7: Refractive index of (K (1%), Fe) codoped ZnO for Fe concentrations: (a) 1%, (b) 2%, (c) 3%, and (d) 4%.

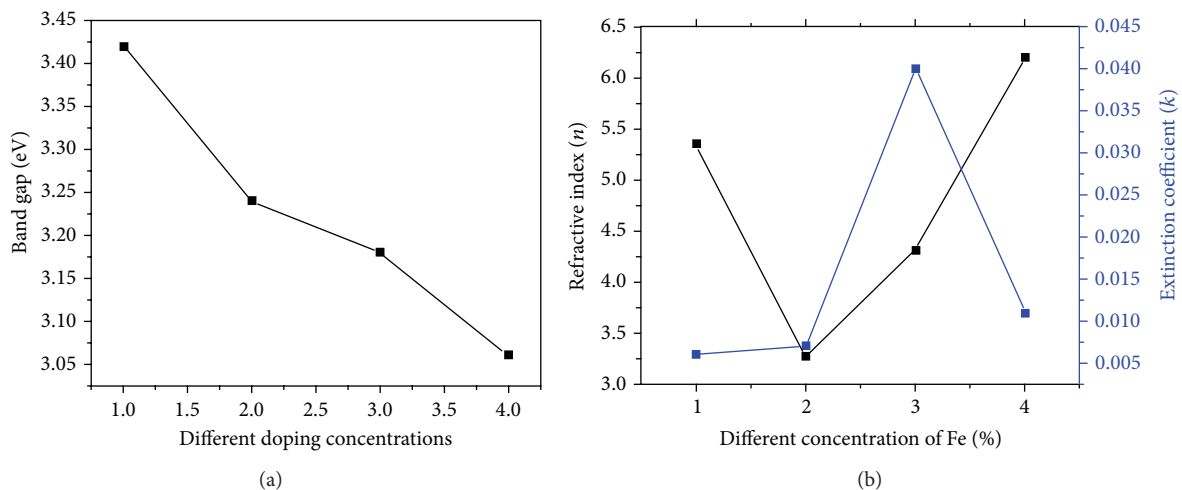


FIGURE 8: The figure shows (a) band gap versus different Fe % and (b) refractive index and extinction coefficient versus different Fe %.

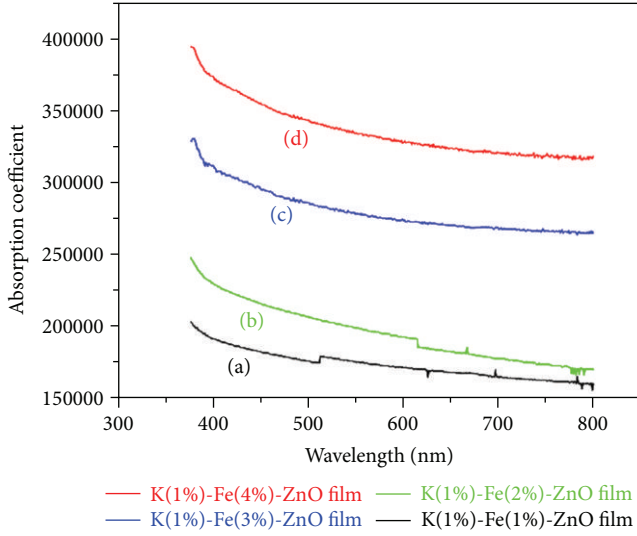


FIGURE 9: Absorption coefficient of (K (1%), Fe) codoped ZnO for Fe concentrations: (a) 1%, (b) 2%, (c) 3%, and (d) 4%.

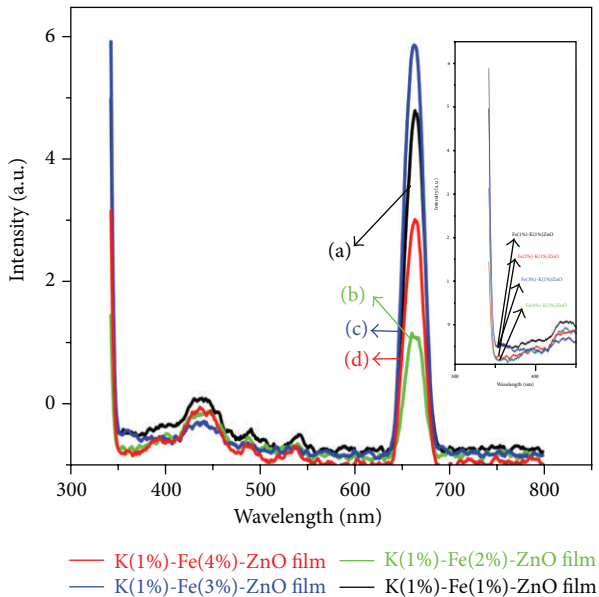


FIGURE 10: Photoluminescence spectrum of (K (1%), Fe) codoped ZnO for Fe concentrations: (a) 1%, (b) 2%, (c) 3%, and (d) 4%.

films exhibit significant changes and are also suitable for integrated optical device application. The normal dispersion indicates that the films do not have voids or any defects. The lower values of extinction coefficient indicate the smoothness of the thin film.

Figure 8 shows the variation of optical band gap, refractive index, and extinction coefficient of Fe concentrations. In Figure 8(a), the optical band gap decreases significantly with increases in Fe concentrations. Figure 8(b) shows that the refractive index of codoped ZnO films is increased (at $\lambda = 375$ nm) considerably for different doping (Fe) concentrations. This indicates that the light normally travels

through the medium. Moreover, the extinction coefficient (k) reveals the well smoothness of thin films surface.

Figure 9 shows the absorption coefficient (α) of (K, Fe) codoped ZnO thin films for different Fe doping concentrations. For ZnO:K (1%), α was $2.75 \times 10^5 \text{ cm}^{-1}$ [31]. In the UV region at $\lambda = 375$ nm, absorption coefficient is $2.03 \times 10^5 \text{ cm}^{-1}$, $2.48 \times 10^5 \text{ cm}^{-1}$, $3.30 \times 10^5 \text{ cm}^{-1}$, and $3.95 \times 10^5 \text{ cm}^{-1}$ for 1, 2, 3, and 4% of Fe, respectively. In the present investigation, in the UV region, the absorption of light depends on the thickness of the film. The higher absorption of ZnO thin films is suitable for antireflecting coating (ARC) and optoelectronic applications [44].

3.6. Photoluminescence Study. Figure 10 shows the photoluminescence spectrum of (K, Fe) codoped ZnO films at room temperature. Generally, UV emissions exist in the range between 360 nm and 380 nm [45]. The UV emission was observed at 389 nm for ZnO:K (1%) [31]. In the present PL spectrum, UV emission appears around 345 nm (3.59 eV) due to the free exciton [46]. However, in the photoluminescence spectrum, the intensity of UV emission significantly varies for 1, 2, and 3% of Fe ion concentrations but the UV intensity is reduced for 4% Fe ion concentration. This may be due to the low concentration of Zn and O and it can be seen in EDAX spectrum. This is the evidence for the variation of UV intensity in the photoluminescence. The weak blue emission is presented with low intensity at 437 nm due to the low interstitial of Zn [47]. The red emission is obtained in the range between 661 nm and 663 nm due to the surplus of oxygen or interstitials of oxygen [48]. The peak position of the photoluminescence depends on the contribution between the free exciton and transition between free electrons to acceptor bound holes [49]. And also the position and intensity of UV and red emissions in PL are enhanced by incorporation of Fe ion in ZnO lattice site. In this study photoluminescence spectrum clearly reveals that the codoped ZnO thin films are defect free.

4. Conclusion

In the current work, the optical properties of (K, Fe) codoped ZnO thin films synthesized on glass substrate by chemical bath deposition technique have been investigated. The X-ray diffraction analysis confirms the hexagonal crystal structure of ZnO thin films. The grains with hexagonal morphology were observed for different Fe ion concentrations. The average thin film surface roughness decreases with increase of Fe ion concentration. The optical transmittance decreases due to the film thickness. The optical band gap of codoped ZnO thin films decreases due to different doping concentration. The different optical properties such as refractive index and absorption coefficient revealed that the optical behavior of thin films and the low extinction coefficient value indicate the better quality of the film. The absorption coefficient shows an increase with doping concentration. The photoluminescence spectrum revealed that the codoped ZnO thin films are mostly defect free. The present study shows that codoped (K,

Fe) ZnO thin films can be suitable candidates for antireflecting coating (ARC) and optoelectronic devices.

Conflict of Interests

The authors declare that there is no conflict of interests regarding the publication of this paper.

References

- [1] S. M. Hatch, J. Briscoe, A. Sapelkin et al., "Influence of anneal atmosphere on ZnO-nanorod photoluminescent and morphological properties with self-powered photodetector performance," *Journal of Applied Physics*, vol. 113, no. 20, Article ID 204501, 2013.
- [2] Y. Lu, X. Zhang, J. Huang et al., "Investigation on antireflection coatings for Al:ZnO in silicon thin-film solar cells," *Optik*, vol. 124, no. 18, pp. 3392–3395, 2013.
- [3] M. Bär, J.-P. Theisen, R. G. Wilks et al., "Lateral inhomogeneity of the Mg/(Zn+Mg) composition at the (Zn,Mg)O/CuIn(S,Se)2 thin-film solar cell interface revealed by photoemission electron microscopy," *Journal of Applied Physics*, vol. 113, no. 19, Article ID 193709, 2013.
- [4] R. Juday, E. M. Silva, J. Y. Huang, P. G. Caldas, R. Prioli, and F. A. Ponce, "Strain-related optical properties of ZnO crystals due to nanoindentation on various surface orientations," *Journal of Applied Physics*, vol. 113, no. 18, Article ID 183511, 2013.
- [5] S. M. Abbas, S. T. Hussain, S. Ali, N. Ahmad, N. Ali, and S. Abbas, "Structure and electrochemical performance of ZnO/CNT composite as anode material for lithium-ion batteries," *Journal of Materials Science*, vol. 48, no. 16, pp. 5429–5436, 2013.
- [6] Z. Zeng, C. S. Garoufalidis, A. F. Terzis, and S. Baskoutas, "Linear and nonlinear optical properties of ZnO/ZnS and ZnS/ZnO core shell quantum dots: effects of shell thickness, impurity, and dielectric environment," *Journal of Applied Physics*, vol. 114, no. 2, Article ID 023510, 2013.
- [7] D. Chu, T. Hamada, K. Kato, and Y. Masuda, "Growth and electrical properties of ZnO films prepared by chemical bath deposition method," *Physica Status Solidi A*, vol. 206, no. 4, pp. 718–723, 2009.
- [8] D. N. Montenegro, V. Hortelano, O. Martínez et al., "Influence of metal organic chemical vapour deposition growth conditions on vibrational and luminescent properties of ZnO nanorods," *Journal of Applied Physics*, vol. 113, no. 14, Article ID 143513, 2013.
- [9] W. Mtangi, M. Schmidt, F. D. Auret et al., "A study of the T₂ defect and the emission properties of the E3 deep level in annealed melt grown ZnO single crystals," *Journal of Applied Physics*, vol. 113, no. 12, Article ID 124502, 2013.
- [10] J. E. Stehr, X. J. Wang, S. Filippov et al., "Defects in N, O and N, Zn implanted ZnO bulk crystals," *Journal of Applied Physics*, vol. 113, no. 10, Article ID 103509, 2013.
- [11] G. Chen, J. J. Peng, C. Song, F. Zeng, and F. Pan, "Interplay between chemical state, electric properties, and ferromagnetism in Fe-doped ZnO films," *Journal of Applied Physics*, vol. 113, no. 10, Article ID 104503, 2013.
- [12] J. Joo, B. Y. Chow, M. Prakash, E. S. Boyden, and J. M. Jacobson, "Face-selective electrostatic control of hydrothermal zinc oxide nanowire synthesis," *Nature Materials*, vol. 10, pp. 596–601, 2011.
- [13] S. S. Shinde, A. P. Korade, C. H. Bhosale, and K. Y. Rajpure, "Influence of tin doping onto structural, morphological, optoelectronic and impedance properties of sprayed ZnO thin films," *Journal of Alloys and Compounds*, vol. 551, pp. 688–693, 2013.
- [14] S.-K. Kim, S. A. Kim, C.-H. Lee, H.-J. Lee, S.-Y. Jeong, and C. R. Cho, "The structural and optical behaviors of K-doped ZnO/Al₂O₃(0001) films," *Applied Physics Letters*, vol. 85, no. 3, pp. 419–421, 2004.
- [15] L. Xu, F. Gu, J. Su, Y. Chen, X. Li, and X. Wang, "The evolution behavior of structures and photoluminescence of K-doped ZnO thin films under different annealing temperatures," *Journal of Alloys and Compounds*, vol. 509, no. 6, pp. 2942–2947, 2011.
- [16] J. Lü, K. Huang, J. Zhu, X. Chen, X. Song, and Z. Sun, "Preparation and characterization of Na-doped ZnO thin films by sol-gel method," *Physica B*, vol. 405, no. 15, pp. 3167–3171, 2010.
- [17] W. Liu, F. Xiu, K. Sun et al., "Na-doped p-type ZnO microwires," *Journal of the American Chemical Society*, vol. 132, no. 8, pp. 2498–2499, 2010.
- [18] S. Kumar and R. Thangavel, "Structural and optical properties of Na doped ZnO nanocrystalline thin films synthesized using sol-gel spin coating technique," *Journal of Sol-Gel Science and Technology*, vol. 67, no. 1, pp. 50–55, 2013.
- [19] M. Joseph, H. Tabata, and T. Kawai, "Ferroelectric behavior of Li-doped ZnO thin films on Si(100) by pulsed laser deposition," *Applied Physics Letters*, vol. 74, no. 17, pp. 2534–2536, 1999.
- [20] S. Kalyanaraman, R. Vettumperumal, and R. Thangavel, "Study of multiple phonon behavior in Li-doped ZnO thin films fabricated using the sol-gel spin-coating technique," *Journal of the Korean Physical Society*, vol. 62, no. 5, pp. 804–808, 2013.
- [21] T. Rattana, S. Suwanboon, P. Amornpitoksuk, A. Haidoux, and P. Limswan, "Improvement of optical properties of nanocrystalline Fe-doped ZnO powders through precipitation method from citrate-modified zinc nitrate solution," *Journal of Alloys and Compounds*, vol. 480, no. 2, pp. 603–607, 2009.
- [22] Y. Zhang, L. Wu, H. Li et al., "Influence of Fe doping on the optical property of ZnO films," *Journal of Alloys and Compounds*, vol. 473, no. 1-2, pp. 319–322, 2009.
- [23] M. Benhaliliba, Y. S. Ocak, and A. Tab, "Characterization of coated fe-doped zinc oxide nanostructures," *Journal of Nano- & Electronic Physics*, vol. 5, no. 3, 2013.
- [24] J. Wang, J. Wan, and K. Chen, "Facile synthesis of superparamagnetic Fe-doped ZnO nanoparticles in liquid polyols," *Materials Letters*, vol. 64, no. 21, pp. 2373–2375, 2010.
- [25] A. Sawalha, M. Abu Abdeen, and A. Sedky, "Electrical conductivity study in pure and doped ZnO ceramic system," *Physica B*, vol. 404, no. 8–11, pp. 1316–1320, 2009.
- [26] J. Xu, S. Shi, X. Zhang, and Y. Wang, "Structural and optical properties of (Al, K)-co-doped ZnO thin films deposited by a sol-gel technique," *Materials Science in Semiconductor Processing*, vol. 16, no. 3, pp. 732–737, 2013.
- [27] D. Zhang, J. Zhang, Z. Guo, and X. Miao, "Optical and electrical properties of zinc oxide thin films with low resistivity via Li-N dual-acceptor doping," *Journal of Alloys and Compounds*, vol. 509, no. 20, pp. 5962–5968, 2011.
- [28] S. Aksoy, Y. Caglar, S. Ilican, and M. Caglar, "Sol-gel derived Li-Mg co-doped ZnO films: preparation and characterization via XRD, XPS, FESEM," *Journal of Alloys and Compounds*, vol. 512, no. 1, pp. 171–178, 2012.

- [29] J. J. Beltrán, J. A. Osorio, C. A. Barrero, C. B. Hanna, and A. Punnoose, "Magnetic properties of Fe doped, Co doped, and Fe+Co co-doped ZnO," *Journal of Applied Physics*, vol. 113, no. 17, Article ID 17C308, 2013.
- [30] S. Ghosh, M. Mandal, and K. Mandal, "Effects of Fe doping and Fe-N-codoping on magnetic properties of SnO₂ prepared by chemical co-precipitation," *Journal of Magnetism and Magnetic Materials*, vol. 323, no. 8, pp. 1083–1087, 2011.
- [31] G. Shanmuganathan, I. B. S. Banu, S. Krishnan, and B. Ranaganathan, "Influence of K-doping on the optical properties of ZnO thin films grown by chemical bath deposition method," *Journal of Alloys and Compounds*, vol. 562, pp. 187–193, 2013.
- [32] B. Zhang, S. Zhou, H. Wang, and Z. Du, "Raman scattering and photoluminescence of Fe-doped ZnO nanocantilever arrays," *Chinese Science Bulletin*, vol. 53, no. 11, pp. 1639–1643, 2008.
- [33] C. S. Prajapati, A. Kushwaha, and P. P. Sahay, "Experimental investigation of spray-deposited Fe-doped ZnO nanoparticle thin films: structural, microstructural and optical properties," *JTTEES*, vol. 22, p. 1232, 2013.
- [34] L. Xu and X. Li, "Influence of Fe-doping on the structural and optical properties of ZnO thin films prepared by sol-gel method," *Journal of Crystal Growth*, vol. 312, no. 6, pp. 851–855, 2010.
- [35] L. C. Yang, R. X. Wang, S. J. Xu et al., "Effects of annealing temperature on the characteristics of Ga-doped ZnO film metal-semiconductor-metal ultraviolet photodetectors," *Journal of Applied Physics*, vol. 113, no. 8, Article ID 084501, 2013.
- [36] S. Saha and V. Gupta, "Al and Fe co-doped transparent conducting ZnO thin film for mediator-less biosensing application," *Journal of Applied Physics*, vol. 1, Article ID 042112, 3 pages, 2013.
- [37] K. A. Eswar, A. Azlinda, H. F. Husairi, M. Rusop, and S. Abdullah, "Post annealing effect on thin film composed ZnO nano-particles on porous silicon," *Nano Bulletin*, vol. 2, p. 130212-3, 2013.
- [38] L. Xu and X. Li, "Influence of Fe-doping on the structural and optical properties of ZnO thin films prepared by sol-gel method," *Journal of Crystal Growth*, vol. 312, no. 6, pp. 851–855, 2010.
- [39] S. M. Salaken, E. Farzana, and J. Podder, "Effect of Fe-doping on the structural and optical properties of ZnO thin films prepared by spray pyrolysis," *Chinese Institute of Electronics*, vol. 34, Article ID 073003, 6 pages, 2013.
- [40] C. S. Prajapati, A. Kushwaha, and P. P. Sahay, "Experimental investigation of spray-deposited fe-doped ZnO nanoparticle thin films: structural, microstructural, and optical properties," *Journal of Thermal Spray Technology*, vol. 22, no. 7, pp. 1230–1241, 2013.
- [41] T. Wang, Y. Liu, Q. Fang et al., "Morphology and optical properties of Co doped ZnO textured thin films," *Journal of Alloys and Compounds*, vol. 509, no. 37, pp. 9116–9122, 2011.
- [42] M. Öztas and M. Bedir, "Thickness dependence of structural, electrical and optical properties of sprayed ZnO:Cu films," *Thin Solid Films*, vol. 516, no. 8, pp. 1703–1709, 2008.
- [43] A. A. Ziabari and F. E. Ghodsi, "Optoelectronic studies of sol-gel derived nanostructured CdO-ZnO composite films," *Journal of Alloys and Compounds*, vol. 509, no. 35, pp. 8748–8755, 2011.
- [44] Q. G. Du, G. Alagappan, H. Dai et al., "UV-blocking ZnO nanostructure anti-reflective coatings," *Optics Communications*, vol. 285, no. 13-14, pp. 3238–3241, 2012.
- [45] O. Lupana, T. Pauporte, L. Chowc et al., "Effects of annealing on properties of ZnO thin films prepared by electrochemical deposition in chloride medium," *Applied Surface Science*, vol. 256, pp. 1895–1907, 2010.
- [46] Z. R. Khan, M. S. Khan, M. Zulfequar, and M. S. Khan, "Optical and structural properties of ZnO thin films fabricated by Sol-Gel method," *Materials Sciences and Applications*, vol. 2, no. 5, pp. 340–345, 2011.
- [47] B. Y. Erdoan, "The alloying effects on the structural and optical properties of nanocrystalline copper zinc oxide thin films fabricated by spin coating and annealing method," *Journal of Alloys and Compounds*, vol. 502, no. 2, pp. 445–450, 2010.
- [48] A. S. Kuznetsov, Y.-G. Lu, S. Turner et al., "Preparation, structural and optical characterization of nanocrystalline ZnO doped with luminescent Ag-nanoclusters," *Optical Materials Express*, vol. 2, no. 6, pp. 723–734, 2012.
- [49] M. Gao, J. Yang, L. Yang et al., "Enhancement of optical properties and donor-related emissions in Y-doped ZnO," *Superlattices and Microstructures*, vol. 52, no. 1, pp. 84–91, 2012.